MOX-Report No. 56/2021

A multiscale CFD model of blood flow in the human left heart coupled with a lumped parameter model of the cardiovascular system

Zingaro, A.; Fumagalli, I.; Dede' L.; Fedele M.; Africa P.C.;

Corno A.F.; Quarteroni A.

MOX, Dipartimento di Matematica
Politecnico di Milano, Via Bonardi 9 - 20133 Milano (Italy)

mox-dmat@polimi.it http://mox.polimi.it

A multiscale CFD model of blood flow in the human left heart coupled with a lumped-parameter model of the cardiovascular system

Alberto Zingaro[1,*], Ivan Fumagalli[1], Luca Dede'[1], Marco Fedele[1], Pasquale C. Africa[1], Antonio F. Corno[2], Alfio Quarteroni[1,3]

[1]MOX, Dipartimento di Matematica, Politecnico di Milano, Piazza Leonardo da Vinci 32, 20133, Milan, Italy
[2]Children's Heart Institute, Hermann Children's Hospital, University of Texas Health, McGovern Medical School, Houston, TX, USA
[3]Chair of Modeling and Scientific Computing (CMCS), Institute of Mathematics, École Polytechnique Fédérale de Lausanne, Station 8, Av. Piccard, CH-1015 Lausanne, Switzerland (Professor Emeritus)

[*]Corresponding author: alberto.zingaro@polimi.it

September 30, 2021

Abstract

We present a novel computational model for the numerical simulation of the blood flow in the human heart by focusing on 3D fluid dynamics of the left heart. With this aim, we employ the Navier-Stokes equations in an Arbitrary Lagrangian Eulerian formulation to account for the endocardium motion, and we model both the mitral and the aortic valves by means of the Resistive Immersed Implicit Surface method. To impose a physiological displacement of the domain boundary, we use a 3D cardiac electromechanical model of the left ventricle coupled to a lumped-parameter (0D) closed-loop model of the circulation and the remaining cardiac chambers, including the left atrium. To extend the left ventricle motion to the endocardium of the left atrium and the ascending aorta, we introduce a preprocessing procedure that combines an harmonic extension of the left ventricle displacement with the motion of the left atrium based on the 0D model. We thus obtain a one-way coupled electromechanics-fluid dynamics model in the left ventricle. To better match the 3D CFD with blood circulation, we also couple the 3D Navier-Stokes equations – with domain motion driven by electromechanics – to the 0D circulation model. We obtain a multiscale coupled 3D-0D fluid dynamics model that we solve via a segregated numerical scheme. We carry out numerical simulations for a healthy left heart and we validate our model by showing that significant hemodynamic indicators are correctly reproduced. We finally show that our model is able to simulate the blood flow in the left heart in the scenario of mitral valve regurgitation.

Keywords: Left heart, Circulation, Cardiac valves, Mitral valve regurgitation, Cardiovascular fluid dynamics, Multiscale modeling.

1 Introduction

The study of cardiac blood flow aims at improving the knowledge of the heart physiology, assessing the pathological conditions and potentially helping the design of treatments. In the clinical routine, blood flow analysis is conventionally based on non-invasive imaging techniques. However, the space and time resolution of the available techniques is not accurate enough to capture small-scales features as recirculation regions, possibile regions of transition to turbulence and small coherent structures [1]. Moreover, imaging techniques cannot provide relevant fluid dynamics indicators such as wall shear stress (WSS), turbulent kinetic energy dissipation, or the oscillatory stress index, which are correlated with the function and remodeling of the heart and vessels [1–5]. In this respect, numerical simulations – also known as in silico simulations – of the

heart and circulation represent a valuable tool to quantitatively assess the cardiac function and to enhance the understanding of cardiovascular diseases.

The hemodynamics in the heart is characterized by different complex features that computational modeling needs to take into account [3]. The mathematical problem is defined in complex geometries, and there is a strong interaction between the myocardial structure and the blood flow due to the electromechanical activity of the heart. This yields a complex coupled problem among electrophysiology, mechanics and fluid dynamics. Furthermore, the topology of the domain changes during the heartbeat due to the presence of unidirectional cardiac valves, affecting the dynamics of the intracardiac flow. In addition, the blood flow regime is known to be nor laminar, nor fully turbulent, but rather transitional [6–9]. Eventually, the flow in the heart is strictly coupled with the flow in the pulmonary and systemic circulation.

The aim of this work is to introduce an accurate computational model accounting for all the features of the hemodynamics in the left heart (LH): the motion of the surrounding tissue, the dynamics of aortic valve (AV) and mitral valve (MV), transitional flow effects, and the flows and pressures in the rest of cardiocirculatory system. Moreover, the present study stands as a significant step towards a high fidelity fluid dynamics model of the whole human heart.

A key point in 3D computational fluid dynamics (CFD) models is the treatment of the boundary displacement, driving the blood motion in the heart chambers. Boundary displacement can be modeled mainly according to the following two paradigms: Fluid-Structure-Interaction (FSI) models and CFD simulation under a prescribed motion. In cardiac FSI problems, the fluid model is coupled with the electromechanics (EM) model and the coupling is explicitly solved, entailing a high computational effort [10–15]. In prescribed displacement CFD simulations, on the other hand, the influence of the cardiac walls motion is modeled by analytical laws [8, 16–22] or by patient-specific image-based reconstructions [3, 23–27].

A possible approach to account for the interdependence between the flow field of the region of interest and the one of the remaining circulation is to rely on geometric multiscale modeling [28]. The specific region of interest (a vessel or a heart chamber) is represented by a 3D model while the remaining part of the circulation is addressed by means of models characterized by a lower geometric dimension, as 0D [28–32] or 1D [28, 33–35] models. Specifically, with 0D models we refer to lumped-parameter models where the dependence on the spatial coordinates is completely neglected, and a uniform spatial distribution of pressures and flowrates in a specific compartment is assumed [28, 36].

The blood flow is modeled by the incompressible Navier-Stokes (NS) equations in an Arbitrary Lagrangian Eulerian (ALE) formulation to account for the moving boundary, whereas the AV and MV are immersed in the domain by the Resistive Immersed Implicit Surface (RIIS) method [23, 37]. In order to account for the transitional flow regime, the Variational Multiscale - Large Eddy Simulation (VMS-LES) turbulence model is considered [8, 38, 39], which also acts as a stabilization method for the CFD numerical scheme. The motion of the wall is derived from an EM simulation on the left ventricle (LV) [40, 41] and then extended to the whole boundary of the domain of interest by means of an original preprocessing procedure, suitably considering a volume-based definition of the displacement of the left atrium (LA). By prescribing the EM-based velocity at the endocardial wall, we enforce a one-way (kinematic) coupling condition between EM and CFD in the LV. Furthermore, to address the interdependence between the fluid dynamics of the LH and the remaining cardiovascular system, we couple the 3D CFD model to the lumped-parameter (0D) model proposed in [40, 41] representing the whole cardiovascular system.

We numerically simulate the hemodynamics of the LH in physiological conditions. We analyze the obtained complex blood flow pattern, and we validate our model by comparing hemodynamic indicators with data available in the literature. Then, we apply our computational model to the case of mitral valve regurgitation, allowing to estimate several clinical indicators and to compare the WSS distribution with the healthy case.

This work is organized as follows: in Section 2 we recall the lumped-parameter circulation model of the cardiovascular system developed in [40, 41]; in Section 3 we describe the mathematical model for the moving-domain hemodynamics in the LH with the immersed valves. In particular, in Section 3.4 we introduce the preprocessing procedure to reconstruct the displacement on the whole domain boundary based on an EM simulation of the LV, while in Section 3.5 we present the reduced valve dynamics model employed. The coupling between the 0D circulation model and the 3D CFD model is described in Section 4. Section 5 is devoted to the description of the numerical approximation of each component of the model and the segregated scheme for their coupling. Numerical results are reported in Section 6: specifically, we consider the case of

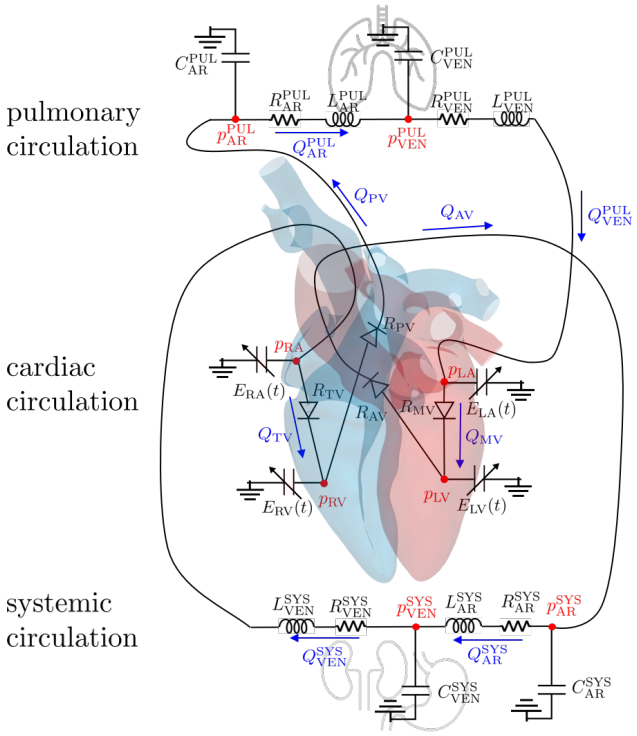

Figure 1: The 0D circulation model of the whole cardiovascular system.

a healthy LH in Section 6.1 and that of mitral valve regurgitation in Section 6.2. Finally, conclusions are drawn in Section 7.

2 A 0D circulation model of the whole cardiovascular system

We employ the closed-loop lumped-parameter (0D) circulation model that was recently proposed in [40] (see also [29, 42]). As represented in Figure 1, the closed-loop model consists of the systemic and pulmonary circulations modelled with resistance-inductance-capacitance (RLC) circuits, one for the arterial part and the other one for the venous part. The electric resistance R models viscosity effects, the inductance L inertial effects and finally the conductance C the compliance of vessels. The four heart chambers (cardiac circulation) are modeled by time-varying elastance elements $E(t)$ and the four valves by non-ideal diodes. Let $V_{\mathrm{LA}}(t)$, $V_{\mathrm{LV}}(t)$, $V_{\mathrm{RA}}(t)$, $V_{\mathrm{RV}}(t)$, $p_{\mathrm{LA}}(t)$, $p_{\mathrm{LV}}(t)$, $p_{\mathrm{RA}}(t)$, $p_{\mathrm{RV}}(t)$ and $E_{\mathrm{LA}}(t)$, $E_{\mathrm{LV}}(t)$, $E_{\mathrm{RA}}(t)$, $E_{\mathrm{RV}}(t)$ be respectively the volumes, pressures and elastances of left atrium (LA), left ventricle (LV), right atrium (RA), right ventricle (RV); $Q_{\mathrm{MV}}(t)$, $Q_{\mathrm{AV}}(t)$, $Q_{\mathrm{TV}}(t)$ and $Q_{\mathrm{PV}}(t)$ the flowrates in mitral valve (MV), aortic valve (AV), tricuspid valve (TV) and pulmonary valve (PV). $Q_{\mathrm{AR}}^{\mathrm{SYS}}(t)$, $Q_{\mathrm{VEN}}^{\mathrm{SYS}}(t)$ and $p_{\mathrm{AR}}^{\mathrm{SYS}}(t)$, $p_{\mathrm{VEN}}^{\mathrm{SYS}}(t)$ are the flowrates and pressures in the systemic circulation respectively in the arterial and venous parts; analogously for $Q_{\mathrm{AR}}^{\mathrm{PUL}}(t)$, $Q_{\mathrm{VEN}}^{\mathrm{PUL}}(t)$ and $p_{\mathrm{AR}}^{\mathrm{PUL}}(t)$, $p_{\mathrm{VEN}}^{\mathrm{PUL}}(t)$ in the pulmonary circulation.

The 0D closed-loop circulation model of the whole cardiovascular system reads [40]: for any $t \in (0, T_f)$:

$$\frac{\mathrm{d}V_{\mathrm{LA}}(t)}{\mathrm{d}t} = Q_{\mathrm{VEN}}^{\mathrm{PUL}}(t) - Q_{\mathrm{MV}}(t), \tag{1a}$$

$$\frac{\mathrm{d}V_{\mathrm{LV}}(t)}{\mathrm{d}t} = Q_{\mathrm{MV}}(t) - Q_{\mathrm{AV}}(t), \tag{1b}$$

$$\frac{\mathrm{d}V_{\mathrm{RA}}(t)}{\mathrm{d}t} = Q_{\mathrm{VEN}}^{\mathrm{SYS}}(t) - Q_{\mathrm{TV}}(t), \tag{1c}$$

$$\frac{\mathrm{d}V_{\mathrm{RV}}(t)}{\mathrm{d}t} = Q_{\mathrm{TV}}(t) - Q_{\mathrm{PV}}(t), \tag{1d}$$

$$C_{\mathrm{AR}}^{\mathrm{SYS}} \frac{\mathrm{d}p_{\mathrm{AR}}^{\mathrm{SYS}}(t)}{\mathrm{d}t} = Q_{\mathrm{AV}}(t) - Q_{\mathrm{AR}}^{\mathrm{SYS}}(t), \tag{1e}$$

$$C_{\mathrm{VEN}}^{\mathrm{SYS}} \frac{\mathrm{d}p_{\mathrm{VEN}}^{\mathrm{SYS}}(t)}{\mathrm{d}t} = Q_{\mathrm{AR}}^{\mathrm{SYS}}(t) - Q_{\mathrm{VEN}}^{\mathrm{SYS}}(t), \tag{1f}$$

$$C_{\mathrm{AR}}^{\mathrm{PUL}} \frac{\mathrm{d}p_{\mathrm{AR}}^{\mathrm{PUL}}(t)}{\mathrm{d}t} = Q_{\mathrm{PV}}(t) - Q_{\mathrm{AR}}^{\mathrm{PUL}}(t), \tag{1g}$$

$$C_{\mathrm{VEN}}^{\mathrm{PUL}} \frac{\mathrm{d}p_{\mathrm{VEN}}^{\mathrm{PUL}}(t)}{\mathrm{d}t} = Q_{\mathrm{AR}}^{\mathrm{PUL}}(t) - Q_{\mathrm{VEN}}^{\mathrm{PUL}}(t), \tag{1h}$$

$$\frac{L_{\mathrm{AR}}^{\mathrm{SYS}}}{R_{\mathrm{AR}}^{\mathrm{SYS}}} \frac{\mathrm{d}Q_{\mathrm{AR}}^{\mathrm{SYS}}(t)}{\mathrm{d}t} = -Q_{\mathrm{AR}}^{\mathrm{SYS}}(t) - \frac{p_{\mathrm{VEN}}^{\mathrm{SYS}}(t) - p_{\mathrm{AR}}^{\mathrm{SYS}}(t)}{R_{\mathrm{AR}}^{\mathrm{SYS}}}, \tag{1i}$$

$$\frac{L_{\mathrm{VEN}}^{\mathrm{SYS}}}{R_{\mathrm{VEN}}^{\mathrm{SYS}}} \frac{\mathrm{d}Q_{\mathrm{VEN}}^{\mathrm{SYS}}(t)}{\mathrm{d}t} = -Q_{\mathrm{VEN}}^{\mathrm{SYS}}(t) - \frac{p_{\mathrm{RA}}(t) - p_{\mathrm{VEN}}^{\mathrm{SYS}}(t)}{R_{\mathrm{VEN}}^{\mathrm{SYS}}}, \tag{1j}$$

$$\frac{L_{\mathrm{AR}}^{\mathrm{PUL}}}{R_{\mathrm{AR}}^{\mathrm{PUL}}} \frac{\mathrm{d}Q_{\mathrm{AR}}^{\mathrm{PUL}}(t)}{\mathrm{d}t} = -Q_{\mathrm{AR}}^{\mathrm{PUL}}(t) - \frac{p_{\mathrm{VEN}}^{\mathrm{PUL}}(t) - p_{\mathrm{AR}}^{\mathrm{PUL}}(t)}{R_{\mathrm{AR}}^{\mathrm{PUL}}}, \tag{1k}$$

$$\frac{L_{\mathrm{VEN}}^{\mathrm{PUL}}}{R_{\mathrm{VEN}}^{\mathrm{PUL}}} \frac{\mathrm{d}Q_{\mathrm{VEN}}^{\mathrm{PUL}}(t)}{\mathrm{d}t} = -Q_{\mathrm{VEN}}^{\mathrm{PUL}}(t) - \frac{p_{\mathrm{LA}}(t) - p_{\mathrm{VEN}}^{\mathrm{PUL}}(t)}{R_{\mathrm{VEN}}^{\mathrm{PUL}}}, \tag{1l}$$

where

$$p_{\mathrm{LA}}(t) = p_{\mathrm{EX}}(t) + E_{\mathrm{LA}}(t)\left(V_{\mathrm{LA}}(t) - V_{0,\mathrm{LA}}\right), \tag{2a}$$

$$p_{\mathrm{LV}}(t) = p_{\mathrm{EX}}(t) + E_{\mathrm{LV}}(t)\left(V_{\mathrm{LV}}(t) - V_{0,\mathrm{LV}}\right), \tag{2b}$$

$$p_{\mathrm{RA}}(t) = p_{\mathrm{EX}}(t) + E_{\mathrm{RA}}(t)\left(V_{\mathrm{RA}}(t) - V_{0,\mathrm{RA}}\right), \tag{3a}$$

$$p_{\mathrm{RV}}(t) = p_{\mathrm{EX}}(t) + E_{\mathrm{RV}}(t)\left(V_{\mathrm{RV}}(t) - V_{0,\mathrm{RV}}\right), \tag{3b}$$

and

$$Q_{\mathrm{MV}}(t) = \frac{p_{\mathrm{LA}}(t) - p_{\mathrm{LV}}(t)}{R_{\mathrm{MV}}(p_{\mathrm{LA}}(t), p_{\mathrm{LV}}(t))}, \tag{4a}$$

$$Q_{\mathrm{AV}}(t) = \frac{p_{\mathrm{LV}}(t) - p_{\mathrm{AR}}^{\mathrm{SYS}}(t)}{R_{\mathrm{AV}}(p_{\mathrm{LV}}(t), p_{\mathrm{AR}}^{\mathrm{SYS}}(t))}, \tag{4b}$$

$$Q_{\mathrm{TV}}(t) = \frac{p_{\mathrm{RA}}(t) - p_{\mathrm{RV}}(t)}{R_{\mathrm{TV}}(p_{\mathrm{RA}}(t), p_{\mathrm{RV}}(t))}, \tag{5a}$$

$$Q_{\mathrm{PV}}(t) = \frac{p_{\mathrm{RV}}(t) - p_{\mathrm{AR}}^{\mathrm{PUL}}(t)}{R_{\mathrm{PV}}(p_{\mathrm{RV}}(t), p_{\mathrm{AR}}^{\mathrm{PUL}}(t))}. \tag{5b}$$

The elastances $E(t)$ of cardiac chambers are analytically prescribed and calibrated on the basis of physiological data; the valves are represented by diodes of resistance $R_k(p_{\mathrm{up}}^{(k)}, p_{\mathrm{down}}^{(k)})$, being $p_{\mathrm{up}}^{(k)}$, $p_{\mathrm{down}}^{(k)}$ the pressure upwind and downwind the valve k, with $k =$ MV, AV, TV, PV. For further details on the 0D closed-loop model adopted, the reader can refer to [40, 41].

3 A 3D fluid dynamics model of the left heart

In this section, we introduce the 3D fluid dynamics model of the LH. Specifically, we present the NS equations in ALE framework with RIIS modelling and the boundary conditions (BCs) we employ for our LH model (Sections 3.1, 3.2, 3.3). We introduce in Section 3.4 the preprocessing procedure to compute the LH displacement and in Section 3.5 the valves dynamics.

3.1 The NS-ALE-RIIS equations

Let $\widehat{\Omega} \subset \mathbb{R}^d$ be the reference configuration and $\partial\widehat{\Omega} \equiv \widehat{\Gamma}$ its sufficiently regular boundary, as displayed in Figure 2. Let $\Omega_t \subset \mathbb{R}^d$ be the fluid domain at a specific time instant $t > 0$ (current configuration), with a sufficiently regular boundary $\partial\Omega_t \equiv \Gamma_t$ oriented by outward pointing normal unit vector $\boldsymbol{n}$. We denote as Γ_t^D and Γ_t^N the portions of the boundary where, respectively, Dirichlet and Neumann type BCs are prescribed,

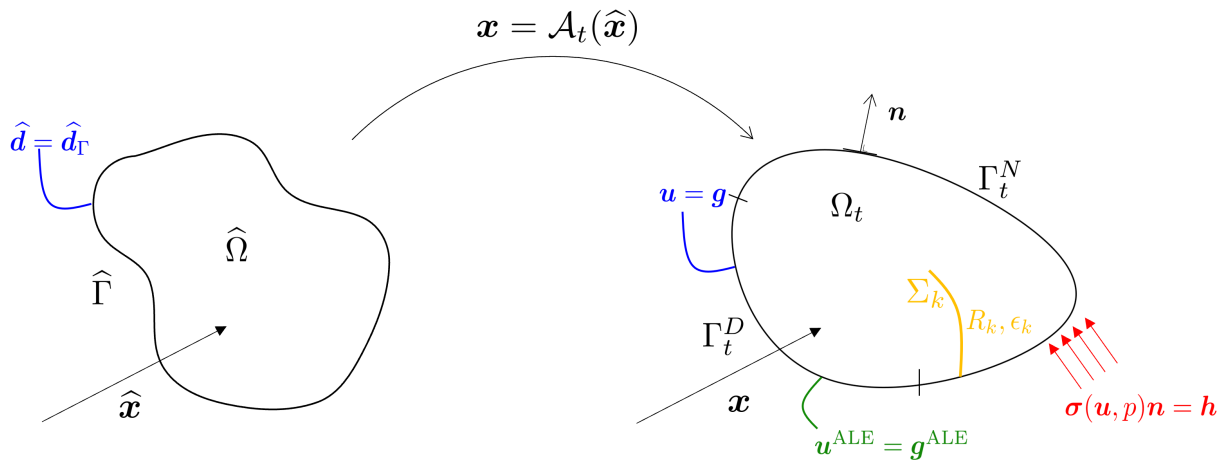

Figure 2: Fluid domain in reference configuration (left), ALE map $\boldsymbol{x} = \mathcal{A}_t(\widehat{\boldsymbol{x}})$ and domain in current configuration (right). In the current configuration, the domain Ω_t is bounded by $\Gamma_t = \Gamma_t^D \cup \Gamma_t^N$; Σ_k is an immersed surface modeled by means of the RIIS method.

with $\Gamma_t = \overline{\Gamma_t^D} \cup \overline{\Gamma_t^N}$ and $\overset{\circ}{\Gamma}{}_t^D \cap \overset{\circ}{\Gamma}{}_t^N = \emptyset$.

We introduce the ALE map $\mathcal{A}_t$ which associates, at each $t \in (0, T_f)$, a point $\widehat{\boldsymbol{x}} \in \widehat{\Omega}$ to a point $\boldsymbol{x} \in \Omega_t$ [43]:

$$\mathcal{A}_t : \widehat{\Omega} \to \Omega_t : \quad \boldsymbol{x} = \mathcal{A}_t(\widehat{\boldsymbol{x}}) = \widehat{\boldsymbol{x}} + \widehat{\boldsymbol{d}}(\widehat{\boldsymbol{x}}, t), \tag{6}$$

being $\widehat{\boldsymbol{d}}$ the domain displacement with respect to the reference configuration $\widehat{\Omega}$. For every function w defined in the current configuration we denote with $\widehat{w} = w \circ \mathcal{A}_t$ the corresponding function in the reference frame. Viceversa, $w = \widehat{w} \circ \mathcal{A}_t^{-1}$.

Assuming $\widehat{\boldsymbol{d}}_\Gamma(\widehat{\boldsymbol{x}}, t)$ to be known on the whole boundary $\widehat{\Gamma}$ at any time $t \in [0, T_f)$, we can extend it to the fluid domain by solving at each time step the following harmonic extension problem:

$$-\Delta \widehat{\boldsymbol{d}} = \boldsymbol{0} \qquad \text{in } \widehat{\Omega}, \tag{7a}$$

$$\widehat{\boldsymbol{d}} = \widehat{\boldsymbol{d}}_\Gamma \qquad \text{on } \widehat{\Gamma}. \tag{7b}$$

Eq. (7) allows to compute at each time step the current domain $\Omega_t = \mathcal{A}_t(\widehat{\Omega})$. The ALE velocity is finally computed as

$$\boldsymbol{u}^{\mathrm{ALE}} = \left(\frac{\partial \widehat{\boldsymbol{d}}}{\partial t} \right) \circ \mathcal{A}_t^{-1}. \tag{8}$$

In heart chambers, blood can be regarded as a Newtonian incompressible fluid and modeled with the incompressible Navier-Stokes (NS) equations [2, 44–46]. Let $\boldsymbol{u}$ be the fluid velocity, p the pressure. The motion of the domain is considered by expressing the NS equations in an ALE framework [43, 47]. The presence of the cardiac valves is accounted by means of the RIIS method [23, 37]. This method, inspired by the Resisitive Immersed Surface (RIS) method introduced in [48] and then applied to cardiac valves in [49, 50], was introduced in [37] and then extended in [23]. It lays in the class of immersed boundary - fictitious domain methods, and it allows to account for a moving immersed surface in an Eulerian framework without requiring the use of a surface-conforming mesh. Specifically, in the RIIS method we introduce into the momentum balance of the NS equations an additional term which penalizes a kinematic condition, i.e. the adherence of the blood to m immersed moving surfaces Σ_k:

$$\Sigma_k = \{\boldsymbol{x} \,:\, \varphi_k(\boldsymbol{x}) = 0\}, \quad \text{with } k = 1, \dots, m. \tag{9}$$

In Eq. (9), $\varphi_k(\boldsymbol{x})$ is a signed-distance function that implicitly describes the k–th immersed surface. In particular, we denote with R_k the resistance coefficient; the resistive term has support in a narrow layer

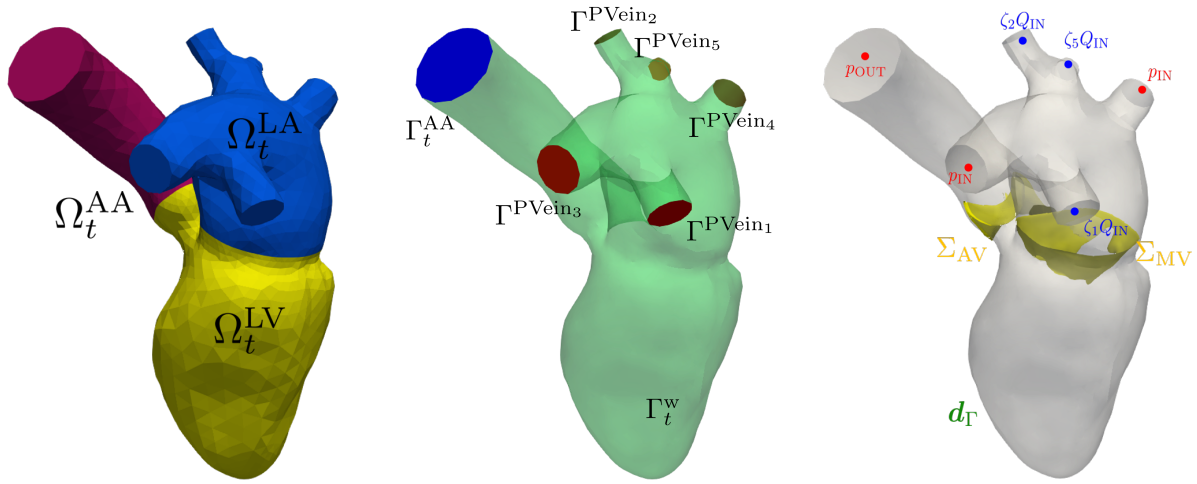

(a) (b) (c)

Figure 3: The LH geometry: (a) the three subdomains $\Omega_t = \Omega_t^{\mathrm{LA}} \cup \Omega_t^{\mathrm{LV}} \cup \Omega_t^{\mathrm{AA}}$; (b) the boundary portions of the LH geometry $\Gamma_t = \left(\bigcup_{i=1}^{5} \Gamma^{\mathrm{PVein}_i}\right) \cup \Gamma_t^{\mathrm{AA}} \cup \Gamma_t^{\mathrm{w}}$; (c) the immersed surfaces Σ_{MV} and Σ_{AV} (respectively in their open and closed configurations), in blue the inlet Dirichlet BCs, in red the Neumann BCs (for both inlet and outlet sections) and in green the Dirichlet condition at wall.

around Σ_k represented by a smoothed Dirac delta type function:

$$\delta_{\Sigma_k,\varepsilon_k}(\varphi_k(\boldsymbol{x})) = \begin{cases} \dfrac{1+\cos(\pi\varphi_k(\boldsymbol{x})/\varepsilon_k)}{2\varepsilon_k} & \text{if } |\varphi_k(\boldsymbol{x})| \le \varepsilon_k, \\ 0 & \text{if } |\varphi_k(\boldsymbol{x})| > \varepsilon_k, \end{cases} \tag{10}$$

and $\varepsilon_k > 0$ is a suitable parameter representing half of thickness of the leaflet. $\boldsymbol{u}_{\Sigma_k}$ is the prescribed immersed surface velocity that, for the sake of simplicity, and similarly to [23] is taken as $\boldsymbol{u}_{\Sigma_k} = \boldsymbol{0}$. We refer to [23, 37] for additional details on the RIIS method.

The incompressible NS equations in ALE framework with RIIS modeling read:

$$\rho\frac{\widehat{\partial}\boldsymbol{u}}{\partial t} + \rho\left(\left(\boldsymbol{u}-\boldsymbol{u}^{\mathrm{ALE}}\right)\cdot\nabla\right)\boldsymbol{u} - \nabla\cdot\boldsymbol{\sigma}(\boldsymbol{u},p) + \sum_{k=1}^{m}\frac{R_k}{\varepsilon_k}\delta_{\Sigma_k,\varepsilon_k}(\varphi_k)\left(\boldsymbol{u}-\boldsymbol{u}_{\Sigma_k}\right) = \boldsymbol{0} \qquad \text{in } \Omega_t\times(0,T_f), \quad (11a)$$

$$\nabla\cdot\boldsymbol{u} = 0 \qquad \text{in } \Omega_t\times(0,T_f), \quad (11b)$$

$$\boldsymbol{u} = \boldsymbol{g} \qquad \text{on } \Gamma_t^D\times(0,T_f), \quad (11c)$$

$$\boldsymbol{\sigma}(\boldsymbol{u},p)\boldsymbol{n} = \boldsymbol{h} \qquad \text{on } \Gamma_t^N\times(0,T_f), \quad (11d)$$

$$\boldsymbol{u} = \boldsymbol{u}_0 \qquad \text{in } \Omega_0\times\{0\}. \quad (11e)$$

We will refer to this formulation as NS-ALE-RIIS formulation; in particular, $\frac{\widehat{\partial}\boldsymbol{u}}{\partial t} = \frac{\partial\boldsymbol{u}}{\partial t} + (\boldsymbol{u}^{\mathrm{ALE}}\cdot\nabla)\boldsymbol{u}$ is the ALE derivative, ρ the fluid density and $\boldsymbol{\sigma}(\boldsymbol{u},p)$ the total stress tensor defined for Newtonian, incompressible and viscous fluids as $\boldsymbol{\sigma}(\boldsymbol{u},p) = -p\boldsymbol{I} + 2\mu\boldsymbol{\epsilon}(\boldsymbol{u})$. μ is the dynamic viscosity and $\boldsymbol{\epsilon}(\boldsymbol{u})$ the strain-rate tensor $\boldsymbol{\epsilon}(\boldsymbol{u}) = \frac{1}{2}\left(\nabla\boldsymbol{u} + (\nabla\boldsymbol{u})^T\right)$. The functions $\boldsymbol{g}$ and $\boldsymbol{h}$ are Dirichlet and Neumann data, $\boldsymbol{u}_0$ the initial datum.

3.2 The LH geometry model

We consider a realistic LH geometry provided by Zygote [51], an accurate 3D model of the heart obtained with CT scan data. The LH is constituted by the LA, LV and a portion of the ascending aorta (AA). The two cardiac chambers (LA, LV) are separated by the MV whereas the AV separates the LV from the AA. The oxygenated blood is collected from the pulmonary veins, the inlets of our domain. The four pulmonary

veins are connected to the upper part of the LA. In the geometry considered there are four pulmonary veins, but one of them is splitted into two inlets, thus, our LH geometry is characterized by five inlet sections as displayed in Figure 3. The blood is then pushed into the systemic circulation through the outlet section of the AA.

As shown in Figure 3a, we decompose the geometry into three subdomains: $\Omega_t = \Omega_t^{\mathrm{LA}} \cup \Omega_t^{\mathrm{LV}} \cup \Omega_t^{\mathrm{AA}}$, namely the LA Ω_t^{LA}, the LV Ω_t^{LV} and the AA Ω_t^{AA}. The boundary is split into $\Gamma_t = \left(\bigcup_{i=1}^{5} \Gamma^{\mathrm{PVein}_i}\right) \cup \Gamma_t^{\mathrm{AA}} \cup \Gamma_t^{\mathrm{w}}$, where we denote with $\Gamma^{\mathrm{PVein}_i}$, $i = 1, \ldots, 5$ the five inlet sections of the four pulmonary veins; with Γ_t^{AA} the outlet section of the ascending aorta and with Γ_t^{w} the endocardium (see Figure 3b). The boundary portions $\Gamma^{\mathrm{PVein}_i}$, $i = 1, \ldots, 5$ are fixed. As displayed in Figure 3c, we immerse in the LH domain two surfaces Σ_{MV} and Σ_{AV}, namely the MV and the AV. Specifics on valves dynamics are given in Section 3.5.

3.3 Boundary conditions

To set pressures and flowrates in the LH, we prescribe Dirichlet BCs on three out of five inlet sections, and Neumann BCs on the remaining two. For the Dirichlet inlet sections, we have at our disposal the inlet flowrate $Q_{\mathrm{IN}}(t)$ only [1]. Thus, the inlet BC is in principle a defective BC because the datum is provided only as averaged scalar quantity [52]. Since a laminar flow regime is reasonably expected in the pulmonary veins throughout the heart-cycle [53, 54], we choose a priori a parabolic velocity profile in space, in the direction of the outward unit normal $\boldsymbol{n}_i$ to the i–th inlet section. Specifically, on the three Dirichlet sections, we set:

$$\boldsymbol{u} = 2Q_{\mathrm{IN}} \frac{\zeta_i}{|\Gamma^{\mathrm{PVein}_i}|} \left(1 - \frac{r^2}{R_i^2}\right) \boldsymbol{n}_i, \qquad \text{on } \Gamma^{\mathrm{PVein}_i} \times (0, T_f), \quad i = 1, 2, 5, \tag{12}$$

being $r(\boldsymbol{x}) = |\boldsymbol{x}|$ the radial coordinate, R_i the radius of the i–th inlet section, $|\Gamma^{\mathrm{PVein}_i}|$ its measure and ζ_i the flow-repartition factor which expresses the amount of flowrate for each inlet section and computed as $\zeta_i = \frac{|\Gamma^{\mathrm{PVein}_i}|}{\sum_{i=1}^{5} |\Gamma^{\mathrm{PVein}_i}|}$. On the two remaining inlet sections, we prescribe the pressure in the pulmonary veins $p_{\mathrm{IN}}(t)$ with a Neumann BC as:

$$\boldsymbol{\sigma}(\boldsymbol{u}, p)\boldsymbol{n} = -p_{\mathrm{IN}} \boldsymbol{n}_i, \qquad \text{on } \Gamma^{\mathrm{PVein}_i} \times (0, T_f), \quad i = 3, 4. \tag{13}$$

On the outlet section Γ_t^{AA} we prescribe a Neumann BC by setting the outlet pressure $p_{\mathrm{OUT}}(t)$:

$$\boldsymbol{\sigma}\left(\boldsymbol{u}, p\right) \boldsymbol{n} = -p_{\mathrm{OUT}} \boldsymbol{n}, \qquad \text{on } \Gamma_t^{\mathrm{AA}} \times (0, T_f). \tag{14}$$

Details on the way we compute inlet flowrate $Q_{\mathrm{IN}}(t)$, inlet and outlet pressures $p_{\mathrm{IN}}(t)$, $p_{\mathrm{OUT}}(t)$ are given in Section 4. Finally, on the endocardium (wall) we prescribe the boundary ALE velocity, by time differentiating the wall displacement $\boldsymbol{d}_\Gamma$ (that will be introduced in Section 3.4) in the current configuration:

$$\boldsymbol{u} = \boldsymbol{u}_\Gamma = \frac{\partial \boldsymbol{d}_\Gamma}{\partial t}, \qquad \text{on } \Gamma_t^{\mathrm{w}} \times (0, T_f). \tag{15}$$

A graphical sketch of the whole set of BCs is given in Figure 3c.

3.4 Displacement modeling

The mathematical problem describing the hemodynamics of the LH is solved by prescribing a given displacement field denoted as $\widehat{\boldsymbol{d}}_\Gamma$ on the endocardium. In particular, the latter is used as Dirichlet BC on Γ_t^{w} for the NS-ALE-RIIS problem in Eq. (15) and for the geometric problem in Eq. (7b) on the whole boundary $\widehat{\Gamma}$. In the following, we present a procedure aimed at computing a physiological LH displacement $\widehat{\boldsymbol{d}}_\Gamma$ on $\widehat{\Gamma}$ starting from an EM simulation of the LV.

We split the wall into $\widehat{\Gamma}^{\mathrm{w}} = \widehat{\Gamma}^{\mathrm{w,\ LA}} \cup \widehat{\Gamma}^{\mathrm{w,\ LV}} \cup \widehat{\Gamma}^{\mathrm{w,\ AA}}$, being respectively the walls of LA, LV and AA as displayed in Figure 4. Let $\widehat{\psi_1}$ and $\widehat{\psi_2}$ be two characteristic functions, $\widehat{\boldsymbol{d}}_{\mathrm{LV}}$ and $\widehat{\boldsymbol{d}}_{\mathrm{LA}}$ two displacement fields

[1] We use the convection of the sign of the flowrate defined according to the outward unit normal $\boldsymbol{n}$. Thus, an inlet flowrate (entering velocity) will be, by definition, negative.

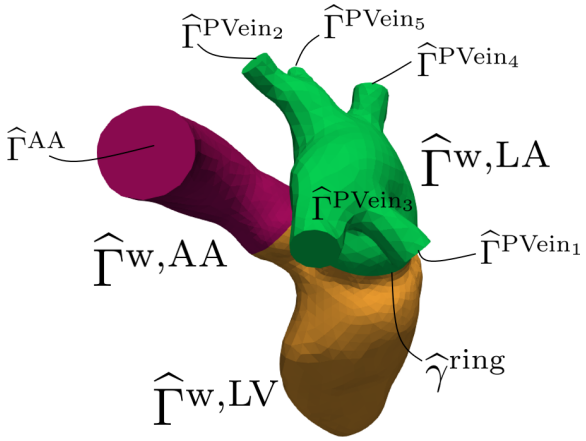

Figure 4: Boundary portions of the LH geometry in reference configuration to model displacement: $\widehat{\Gamma} = \widehat{\Gamma}^{\text{w}} \cup \left(\bigcup_{i=1}^{5} \widehat{\Gamma}^{\text{PVein}_i}\right) \cup \widehat{\Gamma}^{\text{AA}}$, with $\widehat{\Gamma}^{\text{w}} = \widehat{\Gamma}^{\text{w, LA}} \cup \widehat{\Gamma}^{\text{w, LV}} \cup \widehat{\Gamma}^{\text{w, AA}}$ and $\widehat{\gamma}^{\text{ring}} = \overline{\widehat{\Gamma}^{\text{w, LV}}} \cap \left(\widehat{\Gamma} \setminus \widehat{\Gamma}^{\text{w, LV}}\right)$

acting on the whole LH which account respectively for the motion of the LV and the LA. We define the displacement on the whole LH as

$$\widehat{\boldsymbol{d}}_{\Gamma}(\widehat{\boldsymbol{x}}, t) = \underbrace{\widehat{\psi}_1(\widehat{\boldsymbol{x}})\widehat{\boldsymbol{d}}_{\text{LV}}(\widehat{\boldsymbol{x}}, t)}_{\text{(I)}} + \underbrace{\widehat{\psi_2}(\widehat{\boldsymbol{x}})\widehat{\boldsymbol{d}}_{\text{LA}}(\widehat{\boldsymbol{x}}, t)}_{\text{(II)}}, \quad \text{on } \widehat{\Gamma} \times (0, T_f). \tag{16}$$

Thus, we model the LH displacement as the sum of two contributions: (I) a displacement coming from an EM simulation of the LV that we extend to the whole LH domain; (II) an ad-hoc designed displacement for the LA. In the following, we describe how we compute all the quantities involved in Eq. (16), namely the characteristic functions $\widehat{\psi}_1$, $\widehat{\psi}_2$ and the displacement fields $\widehat{\boldsymbol{d}}_{\text{LV}}$, $\widehat{\boldsymbol{d}}_{\text{LA}}$. In Algorithm 1 we summarize the main steps required in the preprocessing procedure; in Figure 5, we represent these steps with boxes numbered as the lines in Algorithm 1. We wish to point out that, since the displacement at the LV is computed through an EM simulation, and we prescribe this datum at walls of the fluid domain, we are enforcing in the LV a kinematic one-way coupling condition between EM and CFD.

3.4.1 EM of a LV and harmonic extension on the whole LH geometry

We describe how we compute the LV displacement through an EM simulation and then its extension on the whole LH geometry. The steps here introduced correspond to boxes 1-5 in Figure 5 and, analogously, to lines 1-5 of Algorithm 1.

We adopt the 3D EM model of the LV developed in [40, 41]. Electrophysiology is modelled through the Monodomain equation [55] coupled with the ten Tusscher-Panfilov ionic model [56]. Subcellular generation of active force is modelled by means of artificial neural networks through the RDQ20-MF model [57]. The passive behaviour of the tissue is modelled through the Guccione strain energy density function [58]. At the epicardium we set generalized Robin-type BCs; on the rings of the AV and MV we impose energy-consistent BCs [59]. Fibers distribution is considered through rule based Bayer-Blake-Plank-Trayanova algorithm [60, 61]. The 3D EM model of the LV is coupled to the 0D closed-loop circulation model of the whole cardiovascular system introduced in Section 2. For the numerical approximation of the problem, we use linear finite elements (FE) for the space discretization. Specifically, in the EM model an intergrid transfer operator [62] is adopted to employ a coarser grid for the elastodynamic and a finer one for the electrophysiology, due to the higher resolution required by the latter. The coupled EM problem is solved by means of the staggered numerical scheme presented in [41]. For additional details on this model and for the numerical methods adopted to solve it, we refer respectively to [40] and [41].

Algorithm 1 Preprocessing procedure to compute LH displacement

Input $\widehat{\Omega}$, $\widehat{\Gamma}$
Output $\widehat{\boldsymbol{d}}_{\Gamma}$

1: LV-EM simulation $\rightarrow \widehat{\boldsymbol{d}}^{\mathrm{EM}}_{\mathrm{LV}}$ on $\widehat{\Omega}^{\mathrm{LV,\,s}} \times (0, T_f)$
2: Extract solution on LV endocardium $\rightarrow \widehat{\boldsymbol{d}}^{\mathrm{EM}}_{\mathrm{LV,\,endo}}$ on $\widehat{\Gamma}^{\mathrm{w,\,LV}} \times (0, T_f)$
3: $\widehat{\boldsymbol{d}}^{\mathrm{EM}}_{\mathrm{LV,\,endo}} \rightarrow$ Laplace - Beltrami (Eq. (17) $\rightarrow \widehat{\boldsymbol{d}}_*$ on $\widehat{\Gamma} \setminus \widehat{\Gamma}^{\mathrm{w,\,LV}} \times (0, T_f)$
4: Compute $\widehat{\boldsymbol{d}}_{\mathrm{LV}}$ on $\widehat{\Gamma} \times (0, T_f)$ (Eq. (18))
5: Compute characteristic functions $\widehat{\psi}_1$, $\widehat{\psi}_2$ on $\widehat{\Gamma}$
6: Solve the geometric problem (7) with Dirichlet datum: $\widehat{\boldsymbol{d}}^{\mathrm{PRE}}_{\Gamma} = \widehat{\psi_1}\widehat{\boldsymbol{d}}_{\mathrm{LV}}$ on $\widehat{\Gamma} \times (0, T_f)$
7: Compute $V_{\mathrm{LV}}(t)$, $V_{\mathrm{AA}}(t)$, $\forall t \in (0, T_f)$
8: Compute $\mathcal{A}(t)$, $\forall t \in (0, T_f)$ (Eq. (22))
9: Solve the 0D circulation model $\rightarrow V_{\mathrm{LA}}(t) = V^{\mathrm{0D}}_{\mathrm{LA}}(t)$
10: Compute $\Phi(t)$, $\forall t \in (0, T_f)$
11: Compute $\widehat{\boldsymbol{e}}^{\mathrm{LA}}_{\mathrm{G}}$ on $\widehat{\Gamma}$
12: Compute $\mathcal{B}(t)$, $\forall t \in (0, T_f)$
13: Solve the ODE in Eq. (24) $\forall t \in (0, T_f) \rightarrow g_{\mathrm{LA}}(t)$
14: $\widehat{\boldsymbol{d}}_{\mathrm{LA}} = \widehat{\boldsymbol{e}}^{\mathrm{LA}}_{\mathrm{G}} g_{\mathrm{LA}}$ on $\widehat{\Gamma} \times (0, T_f)$
15: $\widehat{\boldsymbol{d}}_{\Gamma} = \widehat{\psi}_1 \widehat{\boldsymbol{d}}_{\mathrm{LV}} + \widehat{\psi}_2 \widehat{\boldsymbol{d}}_{\mathrm{LA}}$, on $\widehat{\Gamma} \times (0, T_f)$

Since the one-way coupling ignores the dynamic balance among CFD and EM, the pressure in the LV during the isovolumetric phases (i.e. when both valves are closed) would not be uniquely defined [50, 63] and, as a consequence, we neglect the isovolumetric phases removing them in post-processing.

Let $\widehat{\boldsymbol{d}}^{\mathrm{EM}}_{\mathrm{LV}}(\widehat{\boldsymbol{x}}, t)$ in $\widehat{\Omega}^{\mathrm{LV,\,s}} \times (0, T_f)$ be the displacement of the LV, solution of the EM model and defined in the LV structure ("s", i.e. LV myocardium). In Figure 6a we show the LV in its reference configuration ($\widehat{\Omega}^{\mathrm{LV,\,s}}$); in Figures 6b and 6c we display snapshots of the numerical solution during systole and diastole respectively. Moreover, we also report the solution in Figure 5, box 1.

Let then $\widehat{\boldsymbol{d}}^{\mathrm{EM}}_{\mathrm{LV,\,endo}}(\widehat{\boldsymbol{x}}, t)$ on $\widehat{\Gamma}^{\mathrm{w,\,LV}} \times (0, T_f)$ be the displacement field restricted to the LV endocardium – wall of the LV fluid domain – and shown in Figure 5, box 2.

We compute a displacement $\widehat{\boldsymbol{d}}_*$ acting on LA and AA only. We compute it as the solution of a vectorial Laplace-Beltrami problem. Specifically, we extend on LA and AA the LV displacement $\widehat{\boldsymbol{d}}^{\mathrm{EM}}_{\mathrm{LV,\,endo}}(\widehat{\boldsymbol{x}}, t)$ by keeping the pulmonary veins fixed as (see Figure 5, box 3):

$$-\Delta_{\widehat{\Gamma}} \widehat{\boldsymbol{d}}_* = \boldsymbol{0} \qquad \text{on } \widehat{\Gamma} \setminus \left(\widehat{\Gamma}^{\mathrm{w,\,LV}} \cup \left(\bigcup_{i=1}^{5} \widehat{\Gamma}^{\mathrm{PVein}_i} \right) \right) \times (0, T_f), \tag{17a}$$

$$\widehat{\boldsymbol{d}}_* = \widehat{\boldsymbol{d}}^{\mathrm{EM}}_{\mathrm{LV,\,endo}} \qquad \text{on } \widehat{\gamma}^{\mathrm{ring}} \times (0, T_f), \tag{17b}$$

$$\widehat{\boldsymbol{d}}_* = \boldsymbol{0} \qquad \text{on } \partial\widehat{\Gamma}^{\mathrm{PVein}_i} \times (0, T_f), \quad i = 1, \ldots, 5, \tag{17c}$$

being $\widehat{\gamma}^{\mathrm{ring}} = \overline{\widehat{\Gamma}^{\mathrm{w,\,LV}}} \cap \left(\widehat{\Gamma} \setminus \widehat{\Gamma}^{\mathrm{w,\,LV}} \right)$. We define the displacement $\widehat{\boldsymbol{d}}_{\mathrm{LV}}(\widehat{\boldsymbol{x}}, t)$ on $\widehat{\Gamma} \times (0, T_f)$ as:

$$\widehat{\boldsymbol{d}}_{\mathrm{LV}}(\widehat{\boldsymbol{x}}, t) = \begin{cases} \widehat{\boldsymbol{d}}^{\mathrm{EM}}_{\mathrm{LV,\,endo}}(\widehat{\boldsymbol{x}}, t) & \text{on } \widehat{\Gamma}^{\mathrm{w,\,LV}} \times (0, T_f), \\ \widehat{\boldsymbol{d}}_*(\widehat{\boldsymbol{x}}, t) & \text{on } \widehat{\Gamma} \setminus \widehat{\Gamma}^{\mathrm{w,\,LV}} \times (0, T_f). \end{cases} \tag{18}$$

By combining $\widehat{\boldsymbol{d}}_*$ and $\widehat{\boldsymbol{d}}^{\mathrm{EM}}_{\mathrm{LV,\,endo}}$ as in Eq. (18), the resulting $\widehat{\boldsymbol{d}}_{\mathrm{LV}}$ is hence defined on the whole LH boundary $\widehat{\Gamma}$, as shown in Figure 5, box 4. Thus, $\widehat{\boldsymbol{d}}_{\mathrm{LV}}$ is obtained by extending the EM-based LV displacement on the LH. As a consequence, at this stage, we are still not accounting for any contribution coming from the LA motion. As a matter of fact, a simple extension of the LV displacement would bring to a non physiological LA volume behavior, having then a direct impact on the fluid dynamics simulation, for instance in terms of non-physiological flowrates and pressures. In Section 3.4.2, we propose a simplified model to account for a physiological LA motion.

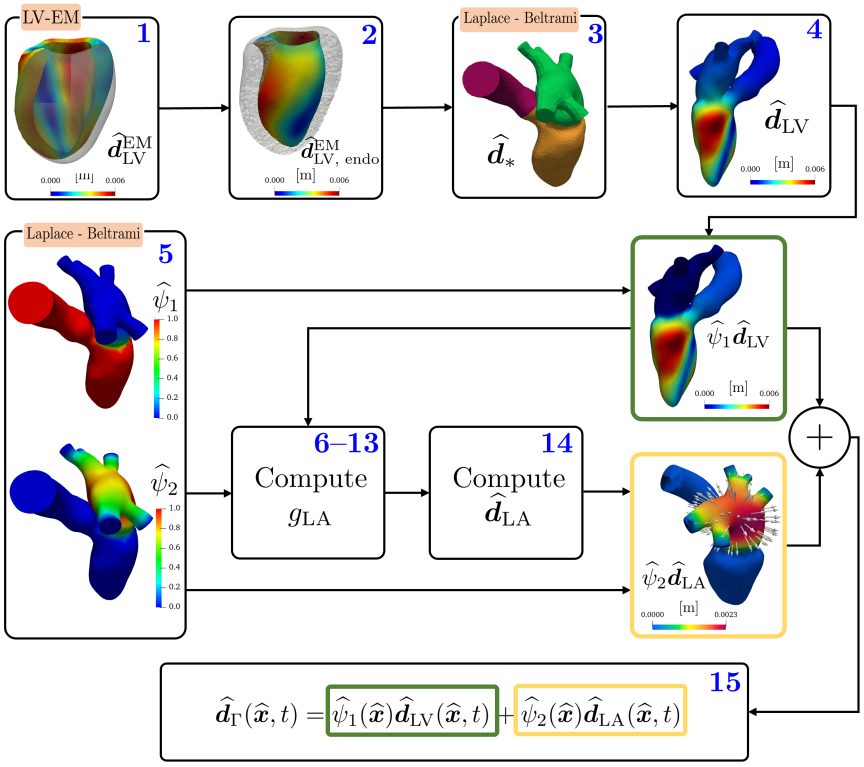

Figure 5: Displacement procedure. Boxes numbers are referred to lines in Algorithm 1.

We compute two scalar characteristic functions $\widehat{\psi}_1(\widehat{\boldsymbol{x}})$ and $\widehat{\psi}_2(\widehat{\boldsymbol{x}})$ on $\widehat{\Gamma}$ (reported in Figure 5, box 5) by solving additional scalar Laplace-Beltrami problems. We introduce them to isolate the effects of LA and LV displacements, while still guaranteeing an overall smooth solution over the whole LH. In particular,

1. $\widehat{\psi}_1(\widehat{\boldsymbol{x}})$ is equal to 1 on $\widehat{\Gamma}^{\mathrm{w,\ LV}} \cup \widehat{\Gamma}^{\mathrm{w,\ AA}} \cup \widehat{\Gamma}^{\mathrm{AA}}$ and smoothly vanishes in a subregion of $\widehat{\Gamma}^{\mathrm{w,\ LA}}$ and it is zero on $\bigcup_{i=1}^{5} \widehat{\Gamma}^{\mathrm{PVein}_i}$;

2. $\widehat{\psi}_2(\widehat{\boldsymbol{x}})$ is equal to 0 on $\widehat{\Gamma}^{\mathrm{w,\ LV}} \cup \widehat{\Gamma}^{\mathrm{w,\ AA}} \cup \widehat{\Gamma}^{\mathrm{AA}}$, positive on $\widehat{\Gamma}^{\mathrm{w,\ LA}}$, and vanishes on $\bigcup_{i=1}^{5} \widehat{\Gamma}^{\mathrm{PVein}_i}$.

In the green box of Figure 5, we report the displacement field $\widehat{\psi}_1\widehat{\boldsymbol{d}}_{\mathrm{LV}}$ arising from the aforementioned steps: on the LV it is equal to to the displacement computed in the EM simulation; it is harmonically extended on the AA and it smoothly vanishes on the LA.

3.4.2 Modeling the LA motion

In absence of an EM model of the whole LH (or of the isolated LA), we propose a simplified model to compute the displacement of the whole LH, also considering the LA physiological motion.

Let $\widehat{\boldsymbol{d}}_{\mathrm{LA}}(\widehat{\boldsymbol{x}},t)$ be the (unknown) displacement of the LA introduced in Eq. (16); we assume that the LA displacement can be modelled by separation of variables [8]. Moreover, we assume that the LA displacement is directed towards its center of volume $\widehat{\boldsymbol{x}}_{\mathrm{G}}^{\mathrm{LA}}$. We introduce $\widehat{\boldsymbol{e}}_{\mathrm{G}}^{\mathrm{LA}}$ as the unit vector directed towards $\widehat{\boldsymbol{x}}_{\mathrm{G}}^{\mathrm{LA}}$ as $\widehat{\boldsymbol{e}}_{\mathrm{G}}^{\mathrm{LA}}(\widehat{\boldsymbol{x}}) = \frac{\widehat{\boldsymbol{x}}-\widehat{\boldsymbol{x}}_{\mathrm{G}}^{\mathrm{LA}}}{|\widehat{\boldsymbol{x}}-\widehat{\boldsymbol{x}}_{\mathrm{G}}^{\mathrm{LA}}|}$, where $|\cdot|$ is the Euclidean norm. Thus, we define $\widehat{\boldsymbol{d}}_{\mathrm{LA}}$ as

$$\widehat{\boldsymbol{d}}_{\mathrm{LA}}(\widehat{\boldsymbol{x}},t) = \widehat{\boldsymbol{e}}_{\mathrm{G}}^{\mathrm{LA}}(\widehat{\boldsymbol{x}}) g_{\mathrm{LA}}(t), \text{ on } \widehat{\Gamma} \times (0, T_f), \tag{19}$$

being $g_{\mathrm{LA}}(t)$ a time-dependent function.

Equation (19) introduces some simplifications since – differently from the LV – we are not considering the LA fibers' direction nor the solution of a suitable EM model. We make these assumptions in order to

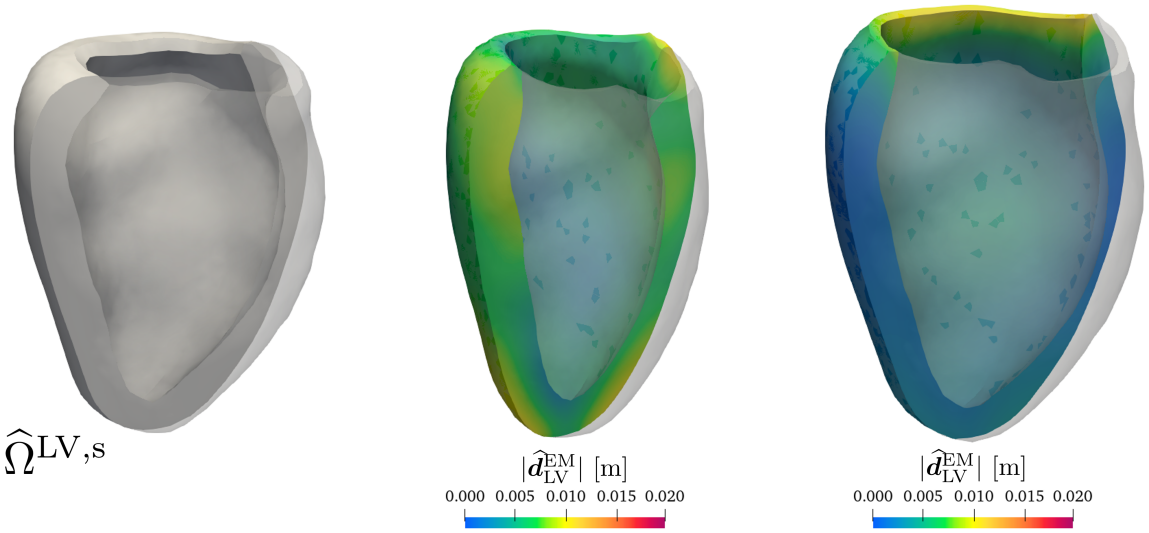

(a) Reference configuration (b) Systole (c) Diastole

Figure 6: EM simulation of the LV: (a) LV in its reference configuration; (b), (c) LV during systole and diastole colored with displacement magnitude.

model the LA displacement in all those cases in which this might not be available as input data: cases in which an EM model is available for the LV only (as in this case) or imaging data given for the LV solely. As a matter of fact, imaging data routinely acquired in diagnostic exams are commonly focused on the LV, thus CFD simulations are carried out on this chamber only, discarding the effects of the overhead atrial flow. This extension procedure can hence be used to fill the missing data and to perform numerical simulations on the whole left part of the heart.

To compute $g_{\mathrm{LA}}(t)$, we consider the LH volume time-derivative and we express it through the Reynolds transport theorem (RTT) [64] as

$$\frac{\mathrm{d}V_{\mathrm{LH}}(t)}{\mathrm{d}t} = \frac{\mathrm{d}}{\mathrm{d}t}\int_{\Omega_t} \mathrm{d}\boldsymbol{x} \overset{\mathrm{RTT}}{=} \oint_{\Gamma_t} \boldsymbol{u}_\Gamma \cdot \boldsymbol{n}\mathrm{d}\boldsymbol{x} = \oint_{\Gamma_t} \frac{\partial}{\partial t}\boldsymbol{d}_\Gamma \cdot \boldsymbol{n}\mathrm{d}\boldsymbol{x}, \tag{20}$$

being V_{LH} the LH volume. By defining $\boldsymbol{u}_\Gamma(\boldsymbol{x},t) = \frac{\partial}{\partial t}\widehat{\boldsymbol{d}}_\Gamma(\mathcal{A}_t^{-1}(x),t)$ and by recalling that for a generic function w holds that $w = \widehat{w}\circ\mathcal{A}_t^{-1}$, we use Eq. (16) and (19) mapped to the current configuration Γ_t in Eq. (20) to get:

$$\frac{\mathrm{d}V_{\mathrm{LH}}(t)}{\mathrm{d}t} = \oint_{\Gamma_t} \frac{\partial}{\partial t}\left(\psi_1(\boldsymbol{x})\boldsymbol{d}_{\mathrm{LV}}(\boldsymbol{x},t)\right)\cdot\boldsymbol{n}\mathrm{d}\boldsymbol{x} + \frac{\mathrm{d}g_{\mathrm{LA}}(t)}{\mathrm{d}t}\oint_{\Gamma_t}\psi_2(\boldsymbol{x})\boldsymbol{e}_{\mathrm{G}}^{\mathrm{LA}}(\boldsymbol{x})\cdot\boldsymbol{n}\mathrm{d}\boldsymbol{x}, \tag{21}$$

Let V_{LA}, V_{LV} and V_{AA} be the volumes of LA, LV and AA, with $V_{\mathrm{LH}}(t) = V_{\mathrm{LA}}(t) + V_{\mathrm{LV}}(t) + V_{\mathrm{AA}}(t)$; we define the fluxes in (21) as

$$\mathcal{A}(t) = \oint_{\Gamma_t} \frac{\partial}{\partial t}\left(\psi_1(\boldsymbol{x})\boldsymbol{d}_{\mathrm{LV}}(\boldsymbol{x},t)\right)\cdot\boldsymbol{n}\mathrm{d}\boldsymbol{x}, \quad \mathcal{B}(t) = \oint_{\Gamma_t}\psi_2(\boldsymbol{x})\boldsymbol{e}_{\mathrm{G}}^{\mathrm{LA}}(\boldsymbol{x})\cdot\boldsymbol{n}\mathrm{d}\boldsymbol{x}, \tag{22}$$

$$\Phi(t) = \frac{\mathrm{d}V_{\mathrm{LH}}(t)}{\mathrm{d}t} - \mathcal{A}(t) = \frac{\mathrm{d}V_{\mathrm{LA}}(t)}{\mathrm{d}t} + \frac{\mathrm{d}V_{\mathrm{LV}}(t)}{\mathrm{d}t} + \frac{\mathrm{d}V_{\mathrm{AA}}(t)}{\mathrm{d}t} - \mathcal{A}(t). \tag{23}$$

Solving Eq. (21) for $\frac{\mathrm{d}g_{\mathrm{LA}}(t)}{\mathrm{d}t}$, yields the following Cauchy problem:

$$\begin{cases} \dfrac{\mathrm{d}g_{\mathrm{LA}}(t)}{\mathrm{d}t} & = \mathcal{B}^{-1}(t)\,\Phi(t), \quad t\in(0,T_f), \\ g_{\mathrm{LA}}(0) & = g_{\mathrm{LA}_0}. \end{cases} \tag{24}$$

Algorithm 2 Numerically compute g_{LA}

Input $\widehat{\Gamma}$, $\widehat{\psi}_2$, $\widehat{\boldsymbol{d}}^{\mathrm{PRE}}_{\Gamma_n,n}$, $n = 0, \dots N_t$
Output g_{LA_n}, $n = 0, \dots N_t$.

1: Initialize $g_{\mathrm{LA}_0} = 0$, $n = 0$, $\Gamma_0 = \widehat{\Gamma}$
2: **while** $n < N_t$ **do**
3: Set $\widehat{\boldsymbol{d}}_{\Gamma_n}(\boldsymbol{x}) = \widehat{\boldsymbol{d}}^{\mathrm{PRE}}_{\Gamma_n}(\widehat{\boldsymbol{x}}) + \widehat{\psi}_2(\widehat{\boldsymbol{x}}) g_{\mathrm{LA}_n} \widehat{\boldsymbol{e}}^{\mathrm{LA}}_{\mathrm{G}}$ on $\widehat{\Gamma}$
4: Move the domain $\rightarrow \Gamma_n$
5: Compute $\boldsymbol{e}^{\mathrm{LA}}_{\mathrm{G}}$ and $\boldsymbol{n}$ on Γ_n
6: $\mathcal{B}_n = \oint_{\Gamma_n} \psi_2(\boldsymbol{x}) \boldsymbol{e}^{\mathrm{LA}}_{\mathrm{G}} \cdot \boldsymbol{n} \mathrm{d}\boldsymbol{x}$
7: $g_{\mathrm{LA},n+1} = g_{\mathrm{LA},n} + \Delta t\, \mathcal{B}_n^{-1}\, \Phi_{n+1}$
8: $n \leftarrow n + 1$
9: **end while**

Since the Zygote's geometry is scanned at 70 % of diastole [51], we consider such instant as initial time $t = 0$ such that $\widehat{\Omega} = \Omega_0$, thus $g_{\mathrm{LA}_0} = 0$. To compute $V_{\mathrm{LA}}(t)$ in Eq. (23), we solve the 0D closed-loop circulation model - tuned on the basis of the EM simulation[2]- and we denote the LA volume computed as $V^{\mathrm{0D}}_{\mathrm{LA}}(t)$. Thus, we set:

$$V_{\mathrm{LA}}(t) = V^{\mathrm{0D}}_{\mathrm{LA}}(t).$$

To compute the remaining terms in $\Phi(t)$, we define a preliminary displacement field which accounts for the LV motion only (i.e. the one appearing in the definition of $\mathcal{A}(t)$ in Eq. (22)):

$$\widehat{\boldsymbol{d}}^{\mathrm{PRE}}_{\Gamma}(\widehat{\boldsymbol{x}}, t) = \widehat{\psi}_1(\widehat{\boldsymbol{x}}) \widehat{\boldsymbol{d}}_{\mathrm{LV}}(\widehat{\boldsymbol{x}}, t), \quad \text{on } \widehat{\Gamma} \times (0, T_f). \tag{25}$$

As reported in Algorithm 1, in order to compute $g_{\mathrm{LA}}(t)$, we first solve a preliminary geometric problem, as the one in Eq. (7) but using $\widehat{\boldsymbol{d}}^{\mathrm{PRE}}_{\Gamma}$ as Dirichlet BC on $\widehat{\Gamma} \times (0, T_f)$. By introducing $\widehat{\boldsymbol{d}}^{\mathrm{PRE}}_{\Gamma}$, we can compute once and for all the volumes $V_{\mathrm{LV}}(t)$, $V_{\mathrm{AA}}(t)$ and the flux $\mathcal{A}(t)$. We solve the 0D circulation model to get $V_{\mathrm{LA}}(t)$ and we compute the flux $\Phi(t)$. Once we compute $\widehat{\boldsymbol{e}}^{\mathrm{LA}}_{\mathrm{G}}$, we calculate the flux $\mathcal{B}(t)$ to finally get $g_{\mathrm{LA}}(t)$ as solution of the Cauchy problem (24). The steps here mentioned are aimed at computing $g_{\mathrm{LA}}(t)$: they are shown in lines 6-13 of Algorithm 1 and gathered in a single box in Figure 5.

Once we get $g_{\mathrm{LA}}(t)$, we can compute $\widehat{\boldsymbol{d}}_{\mathrm{LA}}$ as in Eq. (19) and displayed in box 14 in Figure 5. The magnitude of the displacement $\widehat{\psi}_2 \widehat{\boldsymbol{d}}_{\mathrm{LA}}$ is shown in the yellow box in Figure 5: it is non-null on the LA only, smoothly vanishing towards the pulmonary veins and on the LV and the AA. We also report glyphs of $\widehat{\psi}_2 \widehat{\boldsymbol{d}}_{\mathrm{LA}}$: the LA displacement direction coincides with $\widehat{\boldsymbol{e}}^{\mathrm{LA}}_{\mathrm{G}}$.

The displacement $\boldsymbol{d}_{\Gamma}$ can be eventually computed as in Eq. (16) and as reported in Figure 5, box 15.

3.4.3 Algorithms, numerical methods for the displacement model and displacement results

We implemented the whole procedure in PvPython [65]. To compute $\widehat{\boldsymbol{d}}^{\mathrm{EM}}_{\mathrm{LV}}$ and $\widehat{\boldsymbol{d}}^{\mathrm{PRE}}_{\Gamma}$, solving respectively the EM model of the LV [40, 41] and the geometric problem (7), we carry out numerical simulations using the in-house finite element library life$^{\mathrm{x}}$ [66] (more details will be provided in Section 6). We solved the Laplace-Beltrami problems to get $\widehat{\boldsymbol{d}}_*$, $\widehat{\psi}_1$ and $\widehat{\psi}_2$ using vmtk [67, 68] and the pre-processing tools for cardiac numerical simulations [69].

Specifically, referring to Algorithm 1, the computation of g_{LA} in step 13 would involve a non-linear problem. As a matter of fact, the definition of the flux $\mathcal{B}(t)$ (specified in step 12 and required in step 13) entails an integral acting on LA and computed on Γ_t, which is still unknown. Hence, differently from $\mathcal{A}(t)$ – where we already know the geometry since $\psi_1 = 0$ on the LA – we cannot evaluate this flux once and for all. We address the non linearity by considering the flux $\mathcal{B}$ at the previous time step, as reported in Algorithm 2. We denote with n the quantities evaluated at time step t_n, with $n = 0, \dots, N_t$ and let Δt be the time step

[2]In principle, one could directly adopt the LA volume obtained with the 3D-0D EM model [40, 41]. However, as previously explained, since we remove in post-processing the isovolumetric phases, we calibrate the 0D model to be consistent with the LV volume achieved.

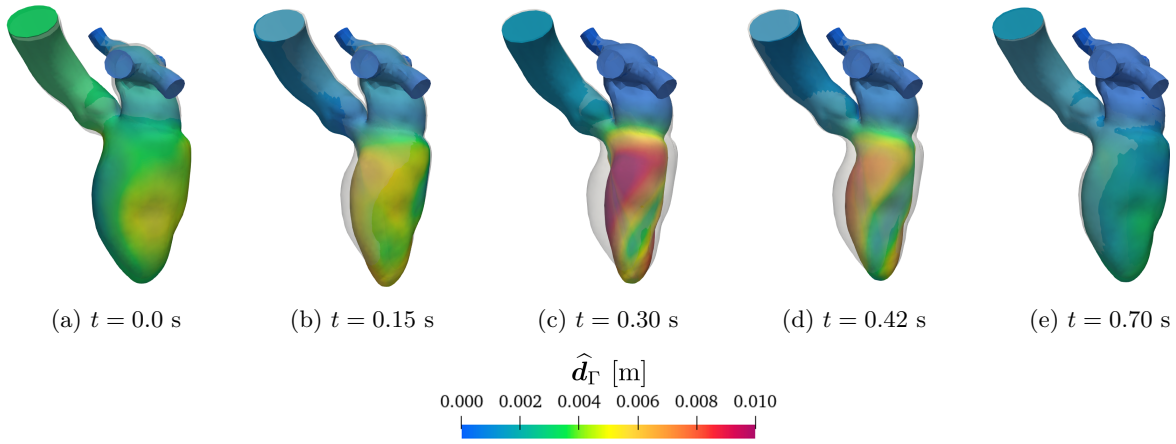

(a) $t = 0.0$ s (b) $t = 0.15$ s (c) $t = 0.30$ s (d) $t = 0.42$ s (e) $t = 0.70$ s

Figure 7: LH geometry warped by $\widehat{\boldsymbol{d}}_\Gamma$ at different time step.

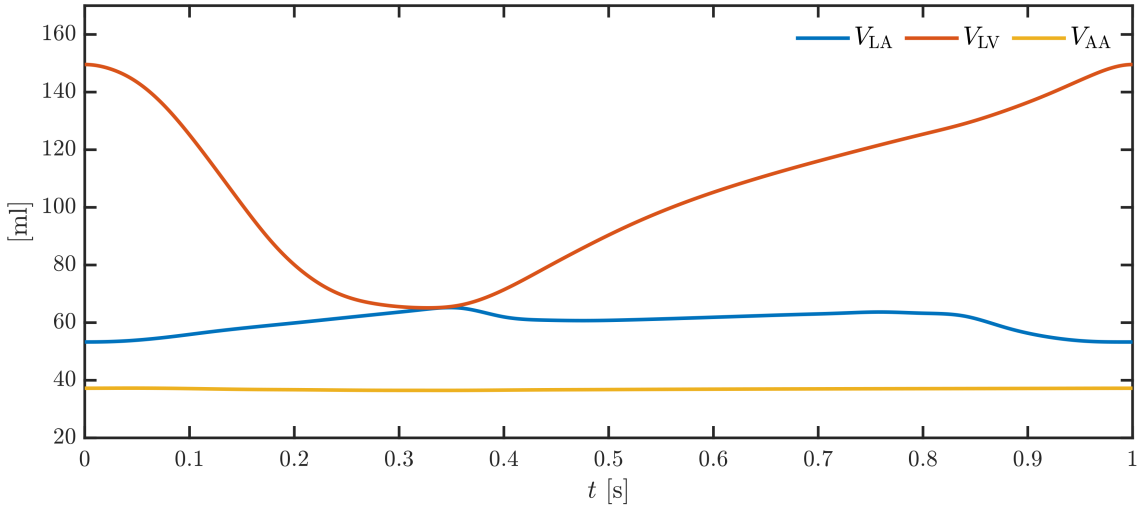

Figure 8: Volumes of LA, LV and AA achieved applying to $\widehat{\Gamma}$ the displacement $\widehat{\boldsymbol{d}}_\Gamma$ defined in Eq. (16).

size. At each time step, we compute the displacement $\widehat{\boldsymbol{d}}_{\Gamma_n}(\widehat{\boldsymbol{x}}) = \widehat{\boldsymbol{d}}_\Gamma(\widehat{\boldsymbol{x}}, t_n)$, we move the domain boundary to recover the geometry Γ_n (computing also $\boldsymbol{e}_{\text{G}}^{\text{LA}}$ and $\boldsymbol{n}$ on Γ_n), we evaluate the flux $\mathcal{B}_n$. The ODE (24) is then numerically integrated with the backward Euler method: given g_{LA_n}, for $n = 0, \dots, N_t - 1$, find $g_{\text{LA}_{n+1}}$ such that

$$g_{\text{LA}_{n+1}} = g_{\text{LA}_n} + \Delta t\, \mathcal{B}_n^{-1}\, \Phi_{n+1}. \tag{26}$$

In Figure 7, we finally report the LH geometry warped by $\widehat{\boldsymbol{d}}_\Gamma$ at different time steps during the heart cycle starting from the time of end diastole. Moreover, in Figure 8 we show the volumes of LA, LV and AA obtained with our preprocessing procedure.

3.5 Valves dynamics

As denoted in Section 3.1, the effect of MV and AV on the fluid is modelled by means of the RIIS method [23, 37]. In addition, we developed preprocessing pipelines to define a displacement to move the leaflets of the cardiac valves and hence to bring the immersed surfaces from the open to the closed configuration and vice versa. The MV and AV are given by Zygote [51] respectively in their closed and open configuration. In

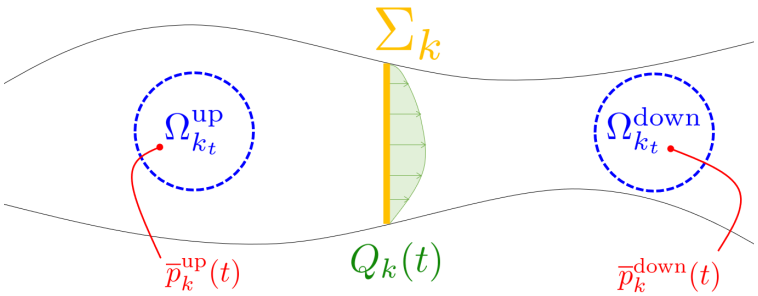

Figure 9: Immersed valve Σ_k with upwind and downwind control volumes where average pressures are computed. Q_k is the flowrate across Σ_k.

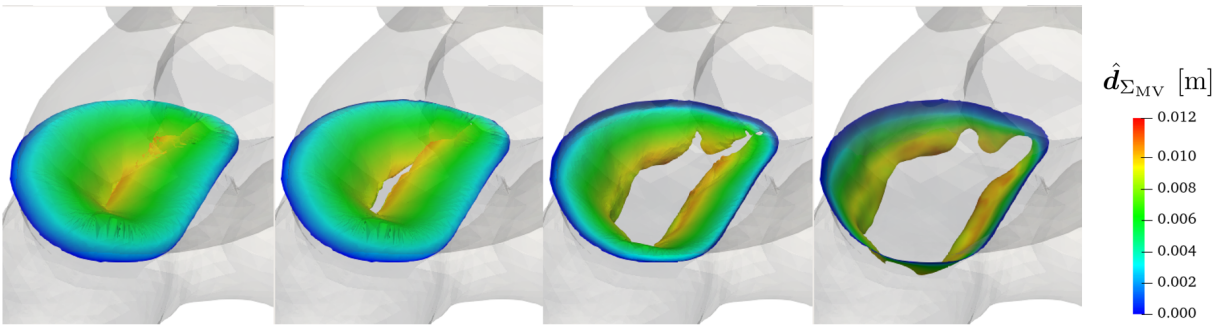

(a) MV

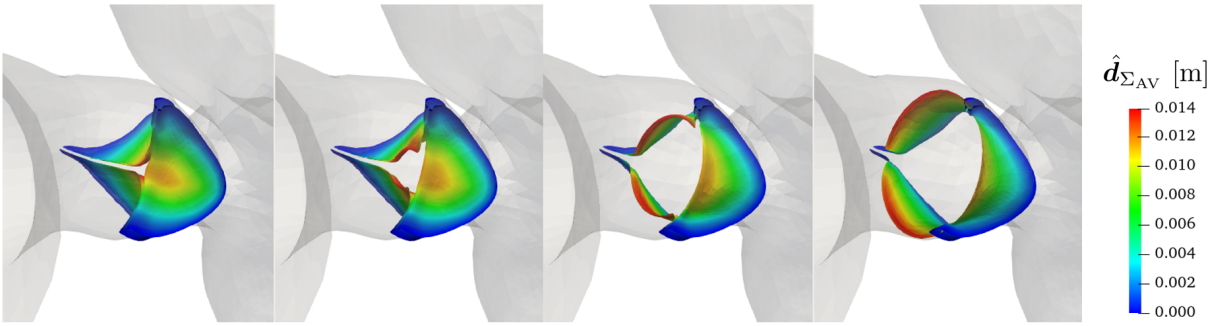

(b) AV

Figure 10: Cardiac valves from their fully closed to their fully open configuration. Leaflets are deformed with the displacement $\widehat{\boldsymbol{d}}_{\Sigma_{\text{MV}}}$ and $\widehat{\boldsymbol{d}}_{\Sigma_{\text{AV}}}$.

Figure 10, we show the cardiac valves from their fully closed to fully open configurations and we denote the valves leaflets' displacements as $\widehat{\boldsymbol{d}}_{\Sigma_{\text{MV}}}(\widehat{\boldsymbol{x}})$ and $\widehat{\boldsymbol{d}}_{\Sigma_{\text{AV}}}(\widehat{\boldsymbol{x}})$.

We do not prescribe a priori the time at which valves open and close as this is the result of our numerical simulations. If a valve is closed, its leaflets start to open when the pressure jump across it becomes positive; viceversa, the valve closes when a condition of reversed flow across the orifice area is detected [50]. The condition on the pressure jump across the valve k, with $k = \text{MV}, \text{AV}$ is checked by considering two control volumes inside the upwind and downwind chambers, namely $\Omega_{k_t}^{\text{up}}$ and $\Omega_{k_t}^{\text{down}}$, as shown in Figure 9. Let

$\overline{p}_k^{\rm up}(t)$ and $\overline{p}_k^{\rm down}(t)$ be the average pressure inside each control volume:

$$\overline{p}_k^{\rm up}(t) = \frac{1}{|\Omega_{k_t}^{\rm up}|}\int_{\Omega_{k_t}^{\rm up}} p(\boldsymbol{x},t)d\boldsymbol{x}, \quad \overline{p}_k^{\rm down}(t) = \frac{1}{|\Omega_{k_t}^{\rm down}|}\int_{\Omega_{k_t}^{\rm down}} p(\boldsymbol{x},t)d\boldsymbol{x}, \tag{27}$$

respectively. Then, the pressure jump across the valve k is computed as

$$\delta\overline{p}_k(t) = \overline{p}_k^{\rm up}(t) - \overline{p}_k^{\rm down}(t). \tag{28}$$

The valve k will thus open when $\delta\overline{p}_k(t) > 0$.

The closure condition at time t of reversed flow is checked when $Q_k(t) < 0$, Q_k being the flowrate through the valve k. Hinging upon a mass balance, the sign of $Q_k(t)$ is directly related to that of $\dot{V}_{\rm LV}(t)$. Therefore, the MV will close when $\dot{V}_{\rm LV}(t) < 0$, while the AV when $\dot{V}_{\rm LV}(t) > 0$

Hence, during a heart cycle, to each cardiac valve two times will be associated: a closing (superscript '$\emptyset$') and an opening (superscript '0') times that we assemble in

$$\boldsymbol{\tau} = \left(\tau_{\rm MV}^{\emptyset},\, \tau_{\rm MV}^{0},\, \tau_{\rm AV}^{\emptyset},\, \tau_{\rm AV}^{0}\right)^T. \tag{29}$$

Opening and closure stages of valves are not instantaneous: we prescribe a given ramp time to fully open/close the valve. For instance, the MV starts opening at $t = \tau_{\rm MV}^0$ and its opening stage ends at $t = \tau_{\rm MV}^0 + \Delta\tau_{\rm MV}^0$, with $\Delta\tau_{\rm MV}^0$ given. More details on the role played by the displacement fields $\widehat{\boldsymbol{d}}_{\Sigma_{\rm MV}}$ and $\widehat{\boldsymbol{d}}_{\Sigma_{\rm AV}}$ and the opening and closing times $\boldsymbol{\tau}$ will be given in Section 5.4.

4 Coupling the 3D CFD model with the 0D circulation model

In order to couple the 3D CFD model of the LH with the 0D circulation model of the whole cardiovascular system, we first remove from the 0D model Eq. (1a), (1b), (2a), (2b), (4a), (4b) and we replace them with the 3D model of the LH. The coupling between che 3D and 0D models consists of the enforcement of the continuity of flowrates and pressures on the "artificially chopped" boundaries, i.e. inlet and outlet sections of the 3D domain: $\Gamma^{{\rm PVein}_i}$, $i = 1, \ldots, 5$ and $\Gamma_t^{\rm AA}$.

Referring to Figure 11, the arterial systemic pressure $p_{\rm AR}^{\rm SYS}(t)$, appearing in Eq. (1e) and (1i) acts as the outlet pressure used in the Neumann BC on the AA outlet section $\Gamma_t^{\rm AA}$ in Eq. (14), formerly denoted as $p_{\rm OUT}(t)$. The outlet BC hence becomes:

$$\boldsymbol{\sigma}(\boldsymbol{u},p)\boldsymbol{n} = -p_{\rm AR}^{\rm SYS}\boldsymbol{n}, \qquad \text{on } \Gamma_t^{\rm AA} \times (0,T_f). \tag{30}$$

Conversely, the LA pressure $p_{\rm LA}(t)$ appearing in Eq. (1l) represents the pressure downwind the "PUL VEN" RLC system, i.e. the one to be prescribed on the inlet sections of our 3D domain. We rename the latter as $p_{\rm LA}^{\rm in}(t)$ and it replaces $p_{\rm IN}(t)$ in the inlet BC (13):

$$\boldsymbol{\sigma}(\boldsymbol{u},p)\boldsymbol{n} = -p_{\rm LA}^{\rm in}\boldsymbol{n}_i, \qquad \text{on } \Gamma^{{\rm PVein}_i} \times (0,T_f), \quad i = 3,4. \tag{31}$$

The flowrate $Q_{\rm VEN}^{\rm PUL}(t)$, appearing in Eq. (1h) and (1l), is the inlet flowrate $Q_{\rm IN}(t)$ used as inlet BC for the 3D problem (see Eq. (12)). Since in all the parts of the heartbeat mass conservation must be ensured, the inlet flowrate should match the volume time derivative of LA and LV in diastole (when the MV is open) and of the sole LA in systole (MV closed):

$$Q_{\rm IN}(t) = \begin{cases} -\dfrac{{\rm d}\left(V_{\rm LV}(t) + V_{\rm LA}(t)\right)}{{\rm d}t} & \text{if MV is open,} \\ -\dfrac{{\rm d}V_{\rm LA}(t)}{{\rm d}t} & \text{if MV is closed.} \end{cases} \tag{32}$$

Since $Q_{\rm IN}(t)$ is computed in the 3D simulation and represents the flowrate in the pulmonary veins, we replace it with $Q_{\rm VEN}^{\rm PUL,\ 3D}(t)$ and the inlet BC becomes:

$$\boldsymbol{u} = 2Q_{\rm VEN}^{\rm PUL,\ 3D}\frac{\zeta_i}{|\Gamma^{{\rm PVein}_i}|}\left(1 - \frac{r^2}{R_i^2}\right)\boldsymbol{n}_i, \qquad \text{on } \Gamma^{{\rm PVein}_i} \times (0,T_f), \quad i = 1,2,5. \tag{33}$$

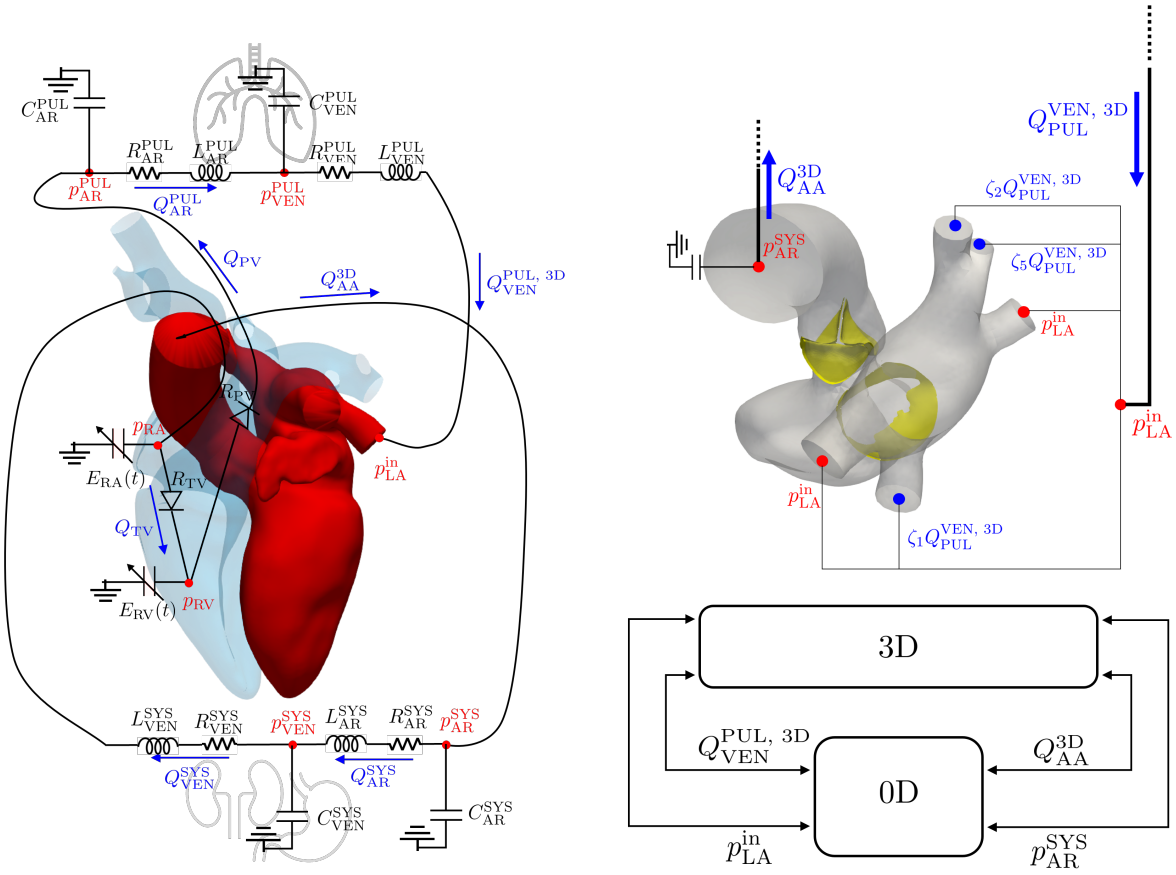

(a) 3D-0D coupling

(b) zoom on LH and continuity of flowrates and pressures among 3D and 0D models.

Figure 11: 3D-0D coupling among the 3D fluid-dynamics model of the LH and the 0D circulation model of the whole cardiovascular system with a zoom on the LH and a scheme explaining the adopted coupled strategy.

In an analogous fashion, the flowrate $Q_{AV}(t)$ in the 0D model represents in our 3D model the outlet flowrate at the AA section Γ_t^{AA}. Hence, we replaced it as $Q_{AA}^{3D}(t)$ and we compute it – exploiting mass balance – as

$$Q_{AA}^{3D}(t) = \begin{cases} -\dfrac{dV_{AA}(t)}{dt} & \text{if AV is closed,} \\ -\dfrac{d\left(V_{LV}(t) + V_{AA}(t)\right)}{dt} & \text{if AV is open.} \end{cases} \tag{34}$$

Eq. (32) and (34) are valid for healthy valves motion. In Section 6.2, we cope the case of a regurgitant MV and the flowrates definitions will properly consider the amount of regurgitant flow. In particular, by considering the valves characteristic times introduced in Section 3.5, Eq. (32) and (34) are conveniently rewritten as:

$$Q_{VEN}^{PUL, 3D}(t) = \begin{cases} -\dfrac{d\left(V_{LV}(t) + V_{LA}(t)\right)}{dt} & \text{if } t < \tau_{MV}^{\emptyset} \text{ or } t \geq \tau_{MV}^{0}, \\ -\dfrac{dV_{LA}(t)}{dt} & \text{if } \tau_{MV}^{\emptyset} \leq t < \tau_{MV}^{0}, \end{cases} \tag{35}$$

$$Q_{\mathrm{AA}}^{\mathrm{3D}}(t) = \begin{cases} -\dfrac{\mathrm{d}V_{\mathrm{AA}}(t)}{\mathrm{d}t} & \text{if } t \le \tau_{\mathrm{AV}}^{0} \text{ or } t > \tau_{\mathrm{AV}}^{\emptyset}, \\ -\dfrac{\mathrm{d}\left(V_{\mathrm{LV}}(t) + V_{\mathrm{AA}}(t)\right)}{\mathrm{d}t} & \text{if } \tau_{\mathrm{AV}}^{0} < t \le \tau_{\mathrm{AV}}^{\emptyset}. \end{cases} \tag{36}$$

Finally, note that, in Eq. (1l), the variable $Q_{\mathrm{VEN}}^{\mathrm{PUL}}(t)$ can be computed from the 3D model using Eq. (32), while $p_{\mathrm{LA}}(t)$ is replaced by $p_{\mathrm{LA}}^{\mathrm{in}}(t)$ and it is an unknown. Hence, we can solve (1l) in terms of the pressure to be prescribed at the inlet sections $p_{\mathrm{LA}}^{\mathrm{in}}(t)$ (see Eq. (38a)). The reduced 0D model arising from these observations is the following: for any $t \in (0, T_f)$:

$$\frac{\mathrm{d}V_{\mathrm{RA}}(t)}{\mathrm{d}t} = Q_{\mathrm{VEN}}^{\mathrm{SYS}}(t) - Q_{\mathrm{TV}}(t), \tag{37a}$$

$$\frac{\mathrm{d}V_{\mathrm{RV}}(t)}{\mathrm{d}t} = Q_{\mathrm{TV}}(t) - Q_{\mathrm{PV}}(t), \tag{37b}$$

$$\frac{\mathrm{d}p_{\mathrm{AR}}^{\mathrm{SYS}}(t)}{\mathrm{d}t} = \frac{1}{C_{\mathrm{AR}}^{\mathrm{SYS}}}\left(Q_{\mathrm{AA}}^{\mathrm{3D}}(t) - Q_{\mathrm{AR}}^{\mathrm{SYS}}(t)\right), \tag{37c}$$

$$\frac{\mathrm{d}p_{\mathrm{VEN}}^{\mathrm{SYS}}(t)}{\mathrm{d}t} = \frac{1}{C_{\mathrm{VEN}}^{\mathrm{SYS}}}\left(Q_{\mathrm{AR}}^{\mathrm{SYS}}(t) - Q_{\mathrm{VEN}}^{\mathrm{SYS}}(t)\right), \tag{37d}$$

$$\frac{\mathrm{d}p_{\mathrm{AR}}^{\mathrm{PUL}}(t)}{\mathrm{d}t} = \frac{1}{C_{\mathrm{AR}}^{\mathrm{PUL}}}\left(Q_{\mathrm{PV}}(t) - Q_{\mathrm{AR}}^{\mathrm{PUL}}(t)\right), \tag{37e}$$

$$\frac{\mathrm{d}p_{\mathrm{VEN}}^{\mathrm{PUL}}(t)}{\mathrm{d}t} = \frac{1}{C_{\mathrm{VEN}}^{\mathrm{PUL}}}\left(Q_{\mathrm{AR}}^{\mathrm{PUL}}(t) - Q_{\mathrm{PUL}}^{\mathrm{VEN,\ 3D}}(t)\right), \tag{37f}$$

$$\frac{\mathrm{d}Q_{\mathrm{AR}}^{\mathrm{SYS}}(t)}{\mathrm{d}t} = \frac{R_{\mathrm{AR}}^{\mathrm{SYS}}}{L_{\mathrm{AR}}^{\mathrm{SYS}}}\left(-Q_{\mathrm{AR}}^{\mathrm{SYS}}(t) - \frac{p_{\mathrm{VEN}}^{\mathrm{SYS}}(t) - p_{\mathrm{AR}}^{\mathrm{SYS}}(t)}{R_{\mathrm{AR}}^{\mathrm{SYS}}}\right), \tag{37g}$$

$$\frac{\mathrm{d}Q_{\mathrm{VEN}}^{\mathrm{SYS}}(t)}{\mathrm{d}t} = \frac{R_{\mathrm{VEN}}^{\mathrm{SYS}}}{L_{\mathrm{VEN}}^{\mathrm{SYS}}}\left(-Q_{\mathrm{VEN}}^{\mathrm{SYS}}(t) - \frac{p_{\mathrm{RA}}(t) - p_{\mathrm{VEN}}^{\mathrm{SYS}}(t)}{R_{\mathrm{VEN}}^{\mathrm{SYS}}}\right), \tag{37h}$$

$$\frac{\mathrm{d}Q_{\mathrm{AR}}^{\mathrm{PUL}}(t)}{\mathrm{d}t} = \frac{R_{\mathrm{AR}}^{\mathrm{PUL}}}{L_{\mathrm{AR}}^{\mathrm{PUL}}}\left(-Q_{\mathrm{AR}}^{\mathrm{PUL}}(t) - \frac{p_{\mathrm{VEN}}^{\mathrm{PUL}}(t) - p_{\mathrm{AR}}^{\mathrm{PUL}}(t)}{R_{\mathrm{AR}}^{\mathrm{PUL}}}\right), \tag{37i}$$

being

$$p_{\mathrm{LA}}^{\mathrm{in}}(t) = p_{\mathrm{VEN}}^{\mathrm{PUL}}(t) - R_{\mathrm{VEN}}^{\mathrm{PUL}} Q_{\mathrm{VEN}}^{\mathrm{PUL,\ 3D}}(t) - L_{\mathrm{VEN}}^{\mathrm{PUL}} \frac{\mathrm{d}Q_{\mathrm{VEN}}^{\mathrm{PUL,\ 3D}}(t)}{\mathrm{d}t}, \tag{38a}$$

$$p_{\mathrm{RA}}(t) = p_{\mathrm{EX}}(t) + E_{\mathrm{RA}}(t)\left(V_{\mathrm{RA}}(t) - V_{0,\mathrm{RA}}\right), \tag{38b}$$

$$p_{\mathrm{RV}}(t) = p_{\mathrm{EX}}(t) + E_{\mathrm{RV}}(t)\left(V_{\mathrm{RV}}(t) - V_{0,\mathrm{RV}}\right), \tag{38c}$$

$$Q_{\mathrm{TV}}(t) = \frac{p_{\mathrm{RA}}(t) - p_{\mathrm{RV}}(t)}{R_{\mathrm{TV}}(p_{\mathrm{RA}}(t), p_{\mathrm{RV}}(t))}, \tag{38d}$$

$$Q_{\mathrm{PV}}(t) = \frac{p_{\mathrm{RV}}(t) - p_{\mathrm{AR}}^{\mathrm{PUL}}(t)}{R_{\mathrm{PV}}(p_{\mathrm{RV}}(t), p_{\mathrm{AR}}^{\mathrm{PUL}}(t))}. \tag{38e}$$

We gather the unknown variables of Equations (37) in a vector $\boldsymbol{c}(t) = (V_{\mathrm{RA}}(t),\ V_{\mathrm{RV}}(t),\ p_{\mathrm{AR}}^{\mathrm{SYS}}(t),\ p_{\mathrm{VEN}}^{\mathrm{SYS}}(t),\ p_{\mathrm{AR}}^{\mathrm{PUL}}(t),\ p_{\mathrm{VEN}}^{\mathrm{PUL}}(t),\ Q_{\mathrm{AR}}^{\mathrm{SYS}}(t),\ Q_{\mathrm{VEN}}^{\mathrm{SYS}}(t),\ Q_{\mathrm{AR}}^{\mathrm{PUL}}(t))^T$ and the left-hand side of Eq. (38) in a vector $\tilde{\boldsymbol{c}}(t) = (p_{\mathrm{LA}}^{\mathrm{in}}(t),\ p_{\mathrm{RA}}(t),\ p_{\mathrm{RV}}(t),\ Q_{\mathrm{TV}}(t),\ Q_{\mathrm{PV}}(t))^T$. We then collect the right-hand sides of Eq. (37) and (38) respectively in the vectors $\boldsymbol{r}(t, \boldsymbol{c}(t), \tilde{\boldsymbol{c}}(t))$ and $\tilde{\boldsymbol{r}}(t, \boldsymbol{c}(t))$. Hence, the reduced 0D model, enriched with suitable initial conditions, is expressed in a compact form as

$$\frac{\mathrm{d}\boldsymbol{c}(t)}{\mathrm{d}t} = \boldsymbol{r}(t, \boldsymbol{c}(t), \tilde{\boldsymbol{c}}(t)) \qquad t \in (0, T_f), \tag{39a}$$

$$\tilde{\boldsymbol{c}}(t) = \tilde{\boldsymbol{r}}(t, \boldsymbol{c}(t)) \qquad t \in (0, T_f), \tag{39b}$$

$$\boldsymbol{c}(0) = \boldsymbol{c}_0. \tag{39c}$$

Finally, a graphical representation of the 3D-0D coupling scheme is given in Figure 11 and the overall set of 3D-0D coupled equations is expressed as

$$
\begin{aligned}
&\rho\frac{\widehat{\partial}\boldsymbol{u}}{\partial t}+\rho\left(\left(\boldsymbol{u}-\boldsymbol{u}^{\mathrm{ALE}}\right)\cdot\nabla\right)\boldsymbol{u}-\nabla\cdot\boldsymbol{\sigma}(\boldsymbol{u},p)+\\
&+\frac{R_{\mathrm{AV}}}{\varepsilon_{\mathrm{AV}}}\delta_{\Sigma_{\mathrm{AV}},\varepsilon_{\mathrm{AV}}}\boldsymbol{u}+\frac{R_{\mathrm{MV}}}{\varepsilon_{\mathrm{MV}}}\delta_{\Sigma_{\mathrm{MV}},\varepsilon_{\mathrm{MV}}}\boldsymbol{u}=\boldsymbol{0} && \text{in } \Omega_t\times(0,T_f), && \text{(40a)}\\
&\nabla\cdot\boldsymbol{u}=0 && \text{in } \Omega_t\times(0,T_f), && \text{(40b)}\\
&\boldsymbol{u}=2Q_{\mathrm{VEN}}^{\mathrm{PUL,\ 3D}}\frac{\zeta_i}{|\Gamma^{\mathrm{PVein}_i}|}\left(1-\frac{r^2}{R_i^2}\right)\boldsymbol{n}_i && \text{on } \Gamma^{\mathrm{PVein}_i}\times(0,T_f),\quad i=1,2,5, && \text{(40c)}\\
&\boldsymbol{\sigma}(\boldsymbol{u},p)\boldsymbol{n}=-p_{\mathrm{LA}}^{\mathrm{in}}\boldsymbol{n}_i && \text{on } \Gamma^{\mathrm{PVein}_i}\times(0,T_f),\quad i=3,4, && \text{(40d)}\\
&\boldsymbol{\sigma}(\boldsymbol{u},p)\boldsymbol{n}=-p_{\mathrm{AR}}^{\mathrm{SYS}}\boldsymbol{n} && \text{on } \Gamma_t^{\mathrm{AA}}\times(0,T_f), && \text{(40e)}\\
&\boldsymbol{u}=\boldsymbol{u}_\Gamma=\partial_t\boldsymbol{d}_\Gamma && \text{on } \Gamma_t^{\mathrm{w}}\times(0,T_f), && \text{(40f)}\\
&\boldsymbol{u}=\boldsymbol{0} && \text{in } \Omega_0\times\{0\}, && \text{(40g)}\\
&\boldsymbol{x}=\widehat{\boldsymbol{x}}+\widehat{\boldsymbol{d}}=\mathcal{A}_t(\widehat{\boldsymbol{x}}) && && \text{(40h)}\\
&-\nabla\cdot\left(\boldsymbol{K}\nabla\widehat{\boldsymbol{d}}\right)=\boldsymbol{0} && \text{in } \widehat{\Omega}, && \text{(40i)}\\
&\widehat{\boldsymbol{d}}=\widehat{\boldsymbol{d}}_\Gamma && \text{on } \widehat{\Gamma}, && \text{(40j)}\\
&\boldsymbol{u}^{\mathrm{ALE}}=\left(\frac{\partial\widehat{\boldsymbol{d}}}{\partial t}\right)\circ\widehat{\boldsymbol{d}}^{-1}, && && \text{(40k)}\\
&\frac{\mathrm{d}\boldsymbol{c}(t)}{\mathrm{d}t}=\boldsymbol{r}(t,\boldsymbol{c}(t),\tilde{\boldsymbol{c}}(t)) && \text{for } t\in(0,T_f), && \text{(40l)}\\
&\tilde{\boldsymbol{c}}(t)=\tilde{\boldsymbol{r}}(t,\boldsymbol{c}(t)) && \text{for } t\in(0,T_f), && \text{(40m)}\\
&\boldsymbol{c}=\boldsymbol{c}_0 && \text{for } t=0. && \text{(40n)}
\end{aligned}
$$

5 Numerical methods

In this section we present the numerical methods to solve the multiscale problem (40). Specifically, we present the numerical schemes for the solutions of the NS-ALE-RIIS equations, the geometric problem and the 0D circulation model respectively; we show the algorithms to determine opening and closing times of valves and to update their leaflet positions. Finally, we introduce the segregated scheme for the coupled problem.

5.1 Space and time discretization of the NS-ALE-RIIS equations and VMS-LES method

For the space discretization of Eq. (11), we introduce the following infinite dimensional function spaces:

$$
\boldsymbol{\mathcal{V}}_{\boldsymbol{g}}:=\left\{\boldsymbol{v}\in[H^1(\Omega_t)]^d:\boldsymbol{v}=\boldsymbol{g}\text{ on }\Gamma_t^D\right\},\quad \mathcal{Q}:=L^2(\Omega_t). \tag{41}
$$

We employ the FE method for the spatial discretization and we denote with the superscript h quantities associated to the FE discretization. We adopt the VMS-LES method [8, 17, 38, 39] to get a stable formulation of the NS equations discretized with FE in the sense of the *inf-sup* condition, to control instabilities arising from advection dominated problems, and to take into account the transitional and nearly turbulent regime that typically occurs in cardiac blood flow [8, 38].

For the time discretization, we partition the time domain in N_t time steps of equal size $\Delta t=\frac{T_f}{N_t}$ and we denote with the subscript n quantities evaluated at time step n: t_n, with $n=0,\dots,N_t$. We use the Backward Differentiation Formula (BDF) scheme of order $\sigma_t=1,2,3$ to discretize the problem in time [39]

Algorithm 3 Geometric problem

Input $\widehat{\boldsymbol{d}}_{\Gamma_n}, \widehat{\Omega}, \widehat{\mathcal{T}}^h$
Output $\boldsymbol{u}_n^{\mathrm{ALE},h}$, Ω_n, $\mathcal{T}_n^h$

Solve lifting problem in Eq. (49) $\rightarrow \widehat{\boldsymbol{d}}_n^h$
Compute ALE velocity through Eq. (50) $\rightarrow \widehat{\boldsymbol{u}}_n^{\mathrm{ALE},h} \rightarrow \boldsymbol{u}_n^{\mathrm{ALE},h}$
Move the domain and the mesh through Eq. (51) $\rightarrow \Omega_n$, $\mathcal{T}_n^h$

and we adopt a semi-implicit treatment of the non linearities by extrapolating the velocity field by means of the Newton-Gregory backward polynomials of order σ_t bringing to the extrapolated velocity $\boldsymbol{u}_{n+1,\mathrm{EXT}}^h$.

The fully discretized linearized semi-implicit VMS-LES formulation of the NS-ALE-RIIS equations with BDF as time integration method reads: given $\boldsymbol{u}_n^h, \ldots, \boldsymbol{u}_{n+1-\sigma_t}^h$, for any $n = 0, \ldots, N_t - 1$, find $(\boldsymbol{u}_{n+1}^h, p_{n+1}^h) \in \mathcal{V}_{\boldsymbol{g}}^h \times \mathcal{Q}^h$ such that:

$$
\begin{aligned}
&\left(\boldsymbol{v}^h, \rho \frac{\alpha_{\mathrm{BDF}} \boldsymbol{u}_{n+1}^h}{\Delta t}\right)_{\Omega_{n+1}} + \left(\boldsymbol{v}^h, \rho \left(\left(\boldsymbol{u}_{n+1,\mathrm{EXT}}^h - \boldsymbol{u}_{n+1}^{\mathrm{ALE},h}\right) \cdot \nabla\right) \boldsymbol{u}_{n+1}^h\right)_{\Omega_{n+1}} + \left(\nabla \boldsymbol{v}^h, \mu \nabla \boldsymbol{u}_{n+1}^h\right)_{\Omega_{n+1}} \\
&- \left(\nabla \cdot \boldsymbol{v}^h, p_{n+1}^h\right)_{\Omega_{n+1}} + \left(q^h, \nabla \cdot \boldsymbol{u}_{n+1}^h\right)_{\Omega_{n+1}} + \left(\boldsymbol{v}^h, \sum_{k=1}^{m} \frac{R_k}{\varepsilon_k} \delta_{\Sigma_k, n+1, \varepsilon_k} \left(\boldsymbol{u}_{n+1}^h - \boldsymbol{u}_{\Sigma_k, n+1}\right)\right)_{\Omega_{n+1}} \\
&+ \mathcal{S}(\boldsymbol{v}^h, q^h, \boldsymbol{u}_{n+1}^h, \boldsymbol{u}_{n+1}^{\mathrm{ALE},h}, \boldsymbol{u}_{n+1,\mathrm{EXT}}^h, p_{n+1}^h, p_{n+1,\mathrm{EXT}}^h) = \left(\boldsymbol{v}^h, \boldsymbol{h}_{n+1}\right)_{\Gamma_{n+1}^N} + \left(\boldsymbol{v}^h, \rho \frac{\boldsymbol{u}_{n,\mathrm{BDF}}^h}{\Delta t}\right)_{\Omega_n} \\
&\quad \text{for all } (\boldsymbol{v}^h, q^h) \in \boldsymbol{\mathcal{V}}_{\boldsymbol{0}}^h \times \mathcal{Q}^h, \quad \text{for all } n \geq \sigma_t - 1.
\end{aligned}
\tag{42}
$$

In Eq. (42), the form $\mathcal{S}$ includes the stabilization and turbulence terms provided by the VMS-LES method. By defining the relative velocity $\boldsymbol{u}_*^h = \boldsymbol{u}_{n+1,\mathrm{EXT}}^h - \boldsymbol{u}_{n+1}^{\mathrm{ALE},h}$, the form $\mathcal{S}$ is expressed as:

$$
\begin{aligned}
&\mathcal{S}(\boldsymbol{v}^h, q^h, \boldsymbol{u}_{n+1}^h, \boldsymbol{u}_{n+1}^{\mathrm{ALE},h}, \boldsymbol{u}_{n+1,\mathrm{EXT}}^h, p_{n+1}^h, p_{n+1,\mathrm{EXT}}^h) = \\
&\left(\rho \boldsymbol{u}_*^h \cdot \nabla \boldsymbol{v}^h + \nabla q^h,\, \tau_{\mathrm{M}}(\boldsymbol{u}_*^h) \boldsymbol{r}_{\mathrm{M}}(\boldsymbol{u}_{n+1}^h, p_{n+1}^h)\right)_{\Omega_{n+1}} + \left(\nabla \cdot \boldsymbol{v}^h, \tau_{\mathrm{C}}(\boldsymbol{u}_*^h) r_{\mathrm{C}}(\boldsymbol{u}_{n+1}^h)\right)_{\Omega_{n+1}} \\
&+ \left(\rho \boldsymbol{u}_*^h \cdot (\nabla \boldsymbol{v}^h)^T, \tau_{\mathrm{M}}(\boldsymbol{u}_*^h) \boldsymbol{r}_{\mathrm{M}}(\boldsymbol{u}_{n+1}^h, p_{n+1}^h)\right)_{\Omega_{n+1}} \\
&- \left(\rho \nabla \boldsymbol{v}^h, \tau_{\mathrm{M}}(\boldsymbol{u}_*^h) \boldsymbol{r}_{\mathrm{M}}(\boldsymbol{u}_*^h, p_{n+1,\mathrm{EXT}}^h) \otimes \tau_{\mathrm{M}}(\boldsymbol{u}_*^h) \boldsymbol{r}_{\mathrm{M}}(\boldsymbol{u}_{n+1}^h, p_{n+1}^h)\right)_{\Omega_{n+1}},
\end{aligned}
\tag{43}
$$

being $\boldsymbol{r}_{\mathrm{M}}(\boldsymbol{u}^h, p^h)$ and $r_{\mathrm{C}}(\boldsymbol{u}^h)$ the strong residuals of (11a) and (11b), defined respectively as:

$$
\boldsymbol{r}_{\mathrm{M}}(\boldsymbol{u}^h, p^h) = \rho \frac{\widehat{\partial} \boldsymbol{u}^h}{\partial t} + \rho \left(\left(\boldsymbol{u}^h - \boldsymbol{u}^{\mathrm{ALE}}\right) \cdot \nabla\right) \boldsymbol{u}^h + \nabla p^h - \mu \Delta \boldsymbol{u}^h + \sum_{k=1}^{m} \frac{R_k}{\varepsilon_k} \delta_{\Sigma_k, \varepsilon_k}(\varphi_k) \left(\boldsymbol{u}^h - \boldsymbol{u}_{\Sigma_k}\right), \tag{44}
$$

$$
r_{\mathrm{C}}(\boldsymbol{u}^h) = \nabla \cdot \boldsymbol{u}^h, \tag{45}
$$

where the temporal derivative in Eq. (44) is approximated with BDF method of the same order σ_t adopted for the temporal discretization in Eq. (42). The stabilization parameters are chosen as in [23, 37–39]:

$$
\tau_{\mathrm{M}}(\boldsymbol{u}^h) = \left(\frac{\sigma_t^2 \rho^2}{\Delta t^2} + \rho^2 \left(\boldsymbol{u}^h - \boldsymbol{u}^{\mathrm{ALE}}\right) \cdot \widetilde{\boldsymbol{G}} \left(\boldsymbol{u}^h - \boldsymbol{u}^{\mathrm{ALE}}\right) + C_r \mu^2 \widetilde{\boldsymbol{G}} : \widetilde{\boldsymbol{G}} + \sum_{k=1}^{m} \frac{R_k^2}{\varepsilon_k^2} \delta_{\Sigma_k, \varepsilon_k}^2(\varphi_k)\right)^{-\frac{1}{2}}, \tag{46}
$$

$$
\tau_{\mathrm{C}}(\boldsymbol{u}^h) = \left(\tau_M(\boldsymbol{u}^h) \widetilde{\boldsymbol{g}} \cdot \widetilde{\boldsymbol{g}}\right)^{-1}, \tag{47}
$$

being $C_r = 15 \cdot 2^r$ a constant obtained by an inverse inequality depending on the local velocity polynomial degree r [38, 39] and $\widetilde{\boldsymbol{G}}$ and $\widetilde{\boldsymbol{g}}$ are respectively the metric tensor and metric vector (see [8, 38]).

Algorithm 4 Valves opening-closing times

Input $\delta\overline{p}_n^{\mathrm{MV},h}$, $\delta\overline{p}_n^{\mathrm{AV},h}$, $\dot{V}_{\mathrm{LV},n}$
Output $\boldsymbol{\tau} = \left(\tau^0_{\mathrm{MV}},\, \tau^{\emptyset}_{\mathrm{MV}},\, \tau^0_{\mathrm{AV}},\, \tau^{\emptyset}_{\mathrm{AV}}\right)^T$

if $t_n = jT_{\mathrm{HB}}$, $j = 0, 1, 2, \dots$ **then**
  $\boldsymbol{\tau} = \mathbf{0}$
end if
if $\delta\overline{p}_{n-1}^{\mathrm{MV},h} \leq 0$ and $\delta\overline{p}_n^{\mathrm{MV},h} > 0$ **then**
  $\tau^0_{\mathrm{MV}} = t_n$
else if $\dot{V}_{\mathrm{LV},n-1} \geq 0$ and $\dot{V}_{\mathrm{LV},n} < 0$ **then**
  $\tau^{\emptyset}_{\mathrm{MV}} = t_n$
end if
if $\delta\overline{p}_{n-1}^{\mathrm{AV},h} \leq 0$ and $\delta\overline{p}_n^{\mathrm{AV},h} > 0$ **then**
  $\tau^0_{\mathrm{AV}} = t_n$
else if $\dot{V}_{\mathrm{LV},n-1} \leq 0$ and $\dot{V}_{\mathrm{LV},n} > 0$ **then**
  $\tau^{\emptyset}_{\mathrm{AV}} = t_n$
end if

Algorithm 5 Valves' leaflets position

Input $\widehat{\boldsymbol{x}}, \widehat{\Sigma}_{\mathrm{MV}}, \widehat{\Sigma}_{\mathrm{AV}}, \widehat{\boldsymbol{d}}_{\Sigma_{\mathrm{MV}}}, \widehat{\boldsymbol{d}}_{\Sigma_{\mathrm{AV}}}, \boldsymbol{\tau}, \Delta\tau^0_{\mathrm{MV}}, \Delta\tau^{\emptyset}_{\mathrm{MV}}, \Delta\tau^0_{\mathrm{AV}}, \Delta\tau^{\emptyset}_{\mathrm{AV}}$
Output $\Sigma_{\mathrm{MV},n}, \Sigma_{\mathrm{AV},n}$
$\eta_{\mathrm{MV},n}, \eta_{\mathrm{AV},n} \in \mathbb{R}$

if $t_n < \tau^0_{\mathrm{MV}}$ **then**
  $\eta_{\mathrm{MV},n} = 0$
else if $\tau^0_{\mathrm{MV}} \leq t_n < \tau^0_{\mathrm{MV}} + \Delta\tau^0_{\mathrm{MV}}$ **then**
  $\eta_{\mathrm{MV},n} = \dfrac{t_n - \tau^0_{\mathrm{MV}}}{\Delta\tau^0_{\mathrm{MV}}}$
else if $\tau^0_{\mathrm{MV}} + \Delta\tau^0_{\mathrm{MV}} \leq t_n < \tau^{\emptyset}_{\mathrm{MV}}$ **then**
  $\eta_{\mathrm{MV},n} = 1$
else if $\tau^{\emptyset}_{\mathrm{MV}} \leq t_n < \tau^{\emptyset}_{\mathrm{MV}} + \Delta\tau^{\emptyset}_{\mathrm{MV}}$ **then**
  $\eta_{\mathrm{MV},n} = -\dfrac{t_n - \tau^{\emptyset}_{\mathrm{MV}}}{\Delta\tau^{\emptyset}_{\mathrm{MV}}}$
else
  $\eta_{\mathrm{MV},n} = 0$
end if

if $t_n < \tau^{\emptyset}_{\mathrm{AV}}$ **then**
  $\eta_{\mathrm{AV},n} = 0$
else if $\tau^{\emptyset}_{\mathrm{AV}} \leq t_n < \tau^{\emptyset}_{\mathrm{AV}} + \Delta\tau^{\emptyset}_{\mathrm{AV}}$ **then**
  $\eta_{\mathrm{AV},n} = \dfrac{t_n - \tau^{\emptyset}_{\mathrm{AV}}}{\Delta\tau^{\emptyset}_{\mathrm{AV}}}$
else if $\tau^{\emptyset}_{\mathrm{AV}} + \Delta\tau^{\emptyset}_{\mathrm{AV}} \leq t_n < \tau^0_{\mathrm{AV}}$ **then**
  $\eta_{\mathrm{AV},n} = 1$
else if $\tau^0_{\mathrm{AV}} \leq t_n < \tau^0_{\mathrm{AV}} + \Delta\tau^0_{\mathrm{AV}}$ **then**
  $\eta_{\mathrm{AV},n} = -\dfrac{t_n - \tau^0_{\mathrm{AV}}}{\Delta\tau^0_{\mathrm{AV}}}$
else
  $\eta_{\mathrm{AV},n} = 0$
end if

$\Sigma_{\mathrm{MV},n} = \left\{ \widehat{\boldsymbol{x}} + \eta_{\mathrm{MV},n}\widehat{\boldsymbol{d}}_{\Sigma_{\mathrm{MV}}} \,:\, \varphi_{\mathrm{MV}}(\widehat{\boldsymbol{x}} + \eta_{\mathrm{MV},n}\widehat{\boldsymbol{d}}_{\Sigma_{\mathrm{MV}}}) = 0 \right\}$
$\Sigma_{\mathrm{AV},n} = \left\{ \widehat{\boldsymbol{x}} + \eta_{\mathrm{AV},n}\widehat{\boldsymbol{d}}_{\Sigma_{\mathrm{AV}}} \,:\, \varphi_{\mathrm{AV}}(\widehat{\boldsymbol{x}} + \eta_{\mathrm{AV},n}\widehat{\boldsymbol{d}}_{\Sigma_{\mathrm{AV}}}) = 0 \right\}$

5.2 Space discretization of the geometric problem

For the ALE lifting problem in Eq. (7), we introduce the infinite dimensional function space $\boldsymbol{\mathcal{V}}_{\widehat{\boldsymbol{d}}_\Gamma} := \left\{ \widehat{\boldsymbol{v}} \in \left[H^1(\widehat{\Omega})\right]^d : \widehat{\boldsymbol{v}} = \widehat{\boldsymbol{d}}_\Gamma \text{ on } \widehat{\Gamma} \right\}$ to get the following weak formulation:

$$\text{find } \widehat{\boldsymbol{d}} \in \boldsymbol{\mathcal{V}}_{\widehat{\boldsymbol{d}}_\Gamma} \text{ such that } \left(\nabla\widehat{\boldsymbol{d}},\, \nabla\widehat{\boldsymbol{w}}\right) = 0 \quad \text{for all } \widehat{\boldsymbol{w}} \in \boldsymbol{\mathcal{V}}_{\mathbf{0}}. \tag{48}$$

The Galerkin formulation of Eq. (48) is expressed as

$$\text{for any } n = 0, \dots, N_t, \text{ find } \widehat{\boldsymbol{d}}_n^h \in \boldsymbol{\mathcal{V}}^h_{\widehat{\boldsymbol{d}}_\Gamma} \text{ such that } \left(\nabla\widehat{\boldsymbol{d}}_n^h,\, \nabla\widehat{\boldsymbol{w}}^h\right) = 0 \quad \text{for all } \widehat{\boldsymbol{w}}^h \in \boldsymbol{\mathcal{V}}^h_{\mathbf{0}}. \tag{49}$$

Algorithm 6 Compute volumes and flowrates

Input $\Omega_n, \mathcal{T}_n^h, \boldsymbol{\tau}$
Output $Q_{\mathrm{VEN},n}^{\mathrm{PUL,\ 3D}}, Q_{\mathrm{AA},n}^{\mathrm{3D}}, \dot{V}_{\mathrm{LV},n}$

Compute volumes: $V_{\mathrm{LV},n} = \int_{\Omega_n^{\mathrm{LV}}} d\boldsymbol{x}, \quad V_{\mathrm{LA},n} = \int_{\Omega_n^{\mathrm{LA}}} d\boldsymbol{x}, \quad V_{\mathrm{AA},n} = \int_{\Omega_n^{\mathrm{AA}}} d\boldsymbol{x}$
Compute flowrates:

$$Q_{\mathrm{VEN},n}^{\mathrm{PUL,\ 3D}} = \begin{cases} -\dfrac{(V_{\mathrm{LV},n} + V_{\mathrm{LA},n}) - (V_{\mathrm{LV},n-1} + V_{\mathrm{LA},n-1})}{\Delta t} & \text{if } t^n < \tau_{\mathrm{MV}}^{\emptyset} \text{ or } t^n \geq \tau_{\mathrm{MV}}^{0} \\ -\dfrac{V_{\mathrm{LA},n} - V_{\mathrm{LA},n-1}}{\Delta t} & \text{if } \tau_{\mathrm{MV}}^{\emptyset} \leq t^n < \tau_{\mathrm{MV}}^{0}. \end{cases}$$

$$Q_{\mathrm{AA},n}^{\mathrm{3D}} = \begin{cases} -\dfrac{V_{\mathrm{AA},n} - V_{\mathrm{AA},n-1}}{\Delta t} & \text{if } t^n < \tau_{\mathrm{AV}}^{0} \text{ or } t^n \geq \tau_{\mathrm{AV}}^{\emptyset} \\ -\dfrac{(V_{\mathrm{LV},n} + V_{\mathrm{AA},n}) - (V_{\mathrm{LV},n-1} - V_{\mathrm{AA},n-1})}{\Delta t} & \text{if } \tau_{\mathrm{AV}}^{0} \leq t^n < \tau_{\mathrm{AV}}^{\emptyset}. \end{cases}$$

Compute LV volume derivative: $\dot{V}_{\mathrm{LV},n} = \frac{V_{\mathrm{LV},n} - V_{\mathrm{LV},n-1}}{\Delta t}$

The ALE velocity in the reference configuration is recovered discretizing Eq. (8) with the Backward Euler Method, as

$$\widehat{\boldsymbol{u}}_n^{\mathrm{ALE},h} = \frac{\widehat{\boldsymbol{d}}_n^h - \widehat{\boldsymbol{d}}_{n-1}^h}{\Delta t}. \tag{50}$$

Finally, we move the domain Ω_n and the mesh $\mathcal{T}_n^h$ according to the ALE map $\mathcal{A}_n(\boldsymbol{x}) = \widehat{\boldsymbol{x}} + \widehat{\boldsymbol{d}}_n^h$ defined in Eq. (6), which gives:

$$\Omega_n = \mathcal{A}_n(\widehat{\Omega}), \quad \mathcal{T}_n^h = \mathcal{A}_n(\widehat{\mathcal{T}^h}). \tag{51}$$

In Algorithm 3 we report the numerical scheme required to solve the geometric problem at time step n. We denote it in short as

$$\left(\boldsymbol{u}_n^{\mathrm{ALE},h},\ \Omega_n,\ \mathcal{T}_n^h\right)^T = \textsc{Geometric}\left(\widehat{\boldsymbol{d}}_{\Gamma_n}, \widehat{\Omega}, \widehat{\mathcal{T}}^h\right). \tag{52}$$

The geometric problem – taking as input the prescribed displacement, the domain and the mesh in its reference configuration – computes the ALE fluid velocity, the domain and the mesh at the current time step.

5.3 Time discretization of the 0D circulation model

As done in [41], we solve the system of ODEs in Eq. (39) with a 4^{th} order explicit Runge-Kutta method. The choice of a high-order time discretization scheme is motivated by the stiffness of the circulation model [41, 70]. The time-step size Δt adopted for its numerical discretization is the same used for the BDF advancing scheme in the 3D problem.

5.4 Valves: algorithms to update opening-closing times and leaflets position

In the following, we show the algorithms adopted to find the valves opening-closing times and to determine the valves' leaflets position based on the displacements $\widehat{\boldsymbol{d}}_{\Sigma_{\mathrm{MV}}}$ and $\widehat{\boldsymbol{d}}_{\Sigma_{\mathrm{AV}}}$ introduced in Section 3.5 and the opening-closing times.

In Algorithm 4 the valves opening-closing times are obtained by checking whether the pressure jump across an immersed surface changes signs (valve opens) and if a condition of reverse flow across the valve is detected (valve closes). At the beginning of each heart cycle of period T_{HB}, the opening-closing times are set to zero. The algorithm is invoked at every time step of the numerical simulation as

$$\boldsymbol{\tau} = \textsc{ValvesOpeningClosingTimes}(\delta\overline{p}_n^{\mathrm{MV},h},\ \delta\overline{p}_n^{\mathrm{AV},h}, \dot{V}_{\mathrm{LV},n}). \tag{53}$$

Algorithm 7 Fluid dynamics problem

Input $\boldsymbol{u}_n^{\mathrm{ALE},h}, p_{\mathrm{LA},n}^{\mathrm{in}}, Q_{\mathrm{VEN},n}^{\mathrm{PUL,\ 3D}}, p_{\mathrm{AR},n}^{\mathrm{SYS}}, \boldsymbol{d}_{\Gamma_n}; R_{\mathrm{MV}},\ R_{\mathrm{AV}},\ \varepsilon_{\mathrm{MV}},\ \varepsilon_{\mathrm{AV}}, \Sigma_{\mathrm{MV},n}, \Sigma_{\mathrm{AV},n};\ \Omega_n,\ \mathcal{T}_n^h$
Output $\boldsymbol{u}_n^h,\ p_n^h,\ \delta\overline{p}_n^{\mathrm{MV},h},\ \delta\overline{p}_n^{\mathrm{AV},h}$

Solve NS-ALE-RIIS equations with VMS-LES modeling in Eq. (42):

$$\begin{aligned}\mathcal{P}_{\text{NS-ALE-RIIS-VMS-LES}}(&\boldsymbol{u}_n^h, p_n^h; \boldsymbol{u}_n^{\mathrm{ALE},h}; p_{\mathrm{LA},n}^{\mathrm{in}}, Q_{\mathrm{VEN},n}^{\mathrm{PUL,\ 3D}}, p_{\mathrm{AR},n}^{\mathrm{SYS}}, \boldsymbol{d}_{\Gamma_n};\\ &\Sigma_{\mathrm{MV},n}, \Sigma_{\mathrm{AV},n},\ R_{\mathrm{MV}},\ R_{\mathrm{AV}},\ \varepsilon_{\mathrm{MV}},\ \varepsilon_{\mathrm{AV}};\\ &\Omega_n,\ \mathcal{T}_n^h) = 0\end{aligned}$$

Compute pressure jumps as in Eq. (28) $\rightarrow \delta\overline{p}_n^{\mathrm{MV},h},\ \delta\overline{p}_n^{\mathrm{AV},h}$

Algorithm 8 Segregated scheme for the 3D-0D coupled problem

Initialize $\boldsymbol{u}_0^h,\ \boldsymbol{c}_0, \delta\overline{p}_0^{\mathrm{MV},h},\ \delta\overline{p}_0^{\mathrm{AV},h},\ \dot{V}_0^{\mathrm{LV}}, n = 1$
Set $R_{\mathrm{MV}},\ R_{\mathrm{AV}},\ \varepsilon_{\mathrm{MV}},\ \varepsilon_{\mathrm{AV}},\ \Delta\tau_{\mathrm{MV}}^0,\ \Delta\tau_{\mathrm{MV}}^{\emptyset},\ \Delta\tau_{\mathrm{AV}}^0,\ \Delta\tau_{\mathrm{AV}}^{\emptyset}$
Compute $\widehat{\boldsymbol{d}}_{\Gamma_n}$ for $n = 0, \dots, N_t$
Compute $\widehat{\boldsymbol{d}}_{\Sigma_{\mathrm{MV}}}, \widehat{\boldsymbol{d}}_{\Sigma_{\mathrm{AV}}}$
while $n \leq N_t$ **do**

$\left(\boldsymbol{u}_n^{\mathrm{ALE},h},\ \Omega_n,\ \mathcal{T}_n^h\right)^T = \textsc{Geometric}\left(\widehat{\boldsymbol{d}}_{\Gamma_n}, \widehat{\Omega}, \widehat{\mathcal{T}}^h,\right)$

$\boldsymbol{\tau} = \textsc{ValvesOpeningClosingTimes}(\delta\overline{p}_n^{\mathrm{MV},h},\ \delta\overline{p}_n^{\mathrm{AV},h}, \dot{V}_{\mathrm{LV},n})$

$\left(Q_{\mathrm{VEN},n}^{\mathrm{PUL,\ 3D}}, Q_{\mathrm{AA},n}^{\mathrm{3D}}, \dot{V}_{\mathrm{LV},n}\right)^T = \textsc{Flowrates}\left(\Omega_n,\ \mathcal{T}_n^h, \boldsymbol{\tau}\right)$

$(\Sigma_{\mathrm{MV},n}, \Sigma_{\mathrm{AV},n})^T = \textsc{ValvesLeafletPosition}(\widehat{\boldsymbol{x}}, \widehat{\Sigma}_{\mathrm{MV}}, \widehat{\Sigma}_{\mathrm{AV}}, \widehat{\boldsymbol{d}}_{\Sigma_{\mathrm{MV}}}, \widehat{\boldsymbol{d}}_{\Sigma_{\mathrm{AV}}}, \boldsymbol{\tau}, \Delta\tau_{\mathrm{MV}}^0, \Delta\tau_{\mathrm{MV}}^{\emptyset}, \Delta\tau_{\mathrm{AV}}^0, \Delta\tau_{\mathrm{AV}}^{\emptyset})$.

$(\boldsymbol{c}_n, \tilde{\boldsymbol{c}}_n)^T = \textsc{Circulation}(Q_{\mathrm{VEN},n}^{\mathrm{PUL,\ 3D}}, Q_{\mathrm{AA},n}^{\mathrm{3D}})$

$\left(\boldsymbol{u}_n^h,\ p_n^h,\ \delta\overline{p}_n^{\mathrm{MV},h},\ \delta\overline{p}_n^{\mathrm{AV},h}\right)^T = \textsc{FluidDynamics}(\boldsymbol{u}_n^{\mathrm{ALE},h}; p_{\mathrm{LA},n}^{\mathrm{in}}, Q_{\mathrm{VEN},n}^{\mathrm{PUL,\ 3D}}, p_{\mathrm{AR},n}^{\mathrm{SYS}}, \boldsymbol{d}_{\Gamma_n};$
$R_{\mathrm{MV}},\ R_{\mathrm{AV}},\ \varepsilon_{\mathrm{MV}},\ \varepsilon_{\mathrm{AV}}, \Sigma_{\mathrm{MV},n}, \Sigma_{\mathrm{AV},n}; \Omega_n,\ \mathcal{T}_n^h)$

$n \leftarrow n + 1$

end while

In Algorithm 5, we report the procedure to determine the position of the valves' leaflets $\Sigma_{\mathrm{MV},n}, \Sigma_{\mathrm{AV},n}$ on the basis of the heartbeat phases (vector $\boldsymbol{\tau}$ determined in Algorithm 4), the space-dependent displacement fields $\widehat{\boldsymbol{d}}_{\Sigma_{\mathrm{MV}}}, \widehat{\boldsymbol{d}}_{\Sigma_{\mathrm{AV}}}$ introduced in Section 3.5. In the algorithm we introduce the scalars $\eta_{\mathrm{MV},n}, \eta_{\mathrm{AV},n} \in \mathbb{R}$ to define fully and partially applied displacement fields. Since our simulation starts at the end-diastole time, the valves reference configuration $\widehat{\Sigma}_{\mathrm{MV}}, \widehat{\Sigma}_{\mathrm{AV}}$ corresponds to the fully opened configuration for MV and the fully closed one for the AV. During the opening and closing stages, the displacement increases (decreases) linearly. We will refer to this algorithm as

$$(\Sigma_{\mathrm{MV},n}, \Sigma_{\mathrm{AV},n})^T = \textsc{ValvesLeafletsPosition}(\widehat{\boldsymbol{x}}, \widehat{\Sigma}_{\mathrm{MV}}, \widehat{\Sigma}_{\mathrm{AV}}, \widehat{\boldsymbol{d}}_{\Sigma_{\mathrm{MV}}}, \widehat{\boldsymbol{d}}_{\Sigma_{\mathrm{AV}}}, \boldsymbol{\tau}, \Delta\tau_{\mathrm{MV}}^0, \Delta\tau_{\mathrm{MV}}^{\emptyset}, \Delta\tau_{\mathrm{AV}}^0, \Delta\tau_{\mathrm{AV}}^{\emptyset}). \tag{54}$$

5.5 A segregated scheme for the 3D-0D coupling

In Algorithm 6, we show how we numerically compute $Q_{\mathrm{VEN},n}^{\mathrm{PUL,\ 3D}}, Q_{\mathrm{AA},n}^{\mathrm{3D}}$ and $\dot{V}_{\mathrm{LV},n}$ given Ω_n, $\mathcal{T}_n^h$ and the valves status described by $\boldsymbol{\tau}$. We denote it in short as:

$$\left(Q_{\mathrm{VEN},n}^{\mathrm{PUL,\ 3D}}, Q_{\mathrm{AA},n}^{\mathrm{3D}}, \dot{V}_{\mathrm{LV},n}\right)^T = \textsc{Flowrates}\left(\Omega_n,\ \mathcal{T}_n^h, \boldsymbol{\tau}\right). \tag{55}$$

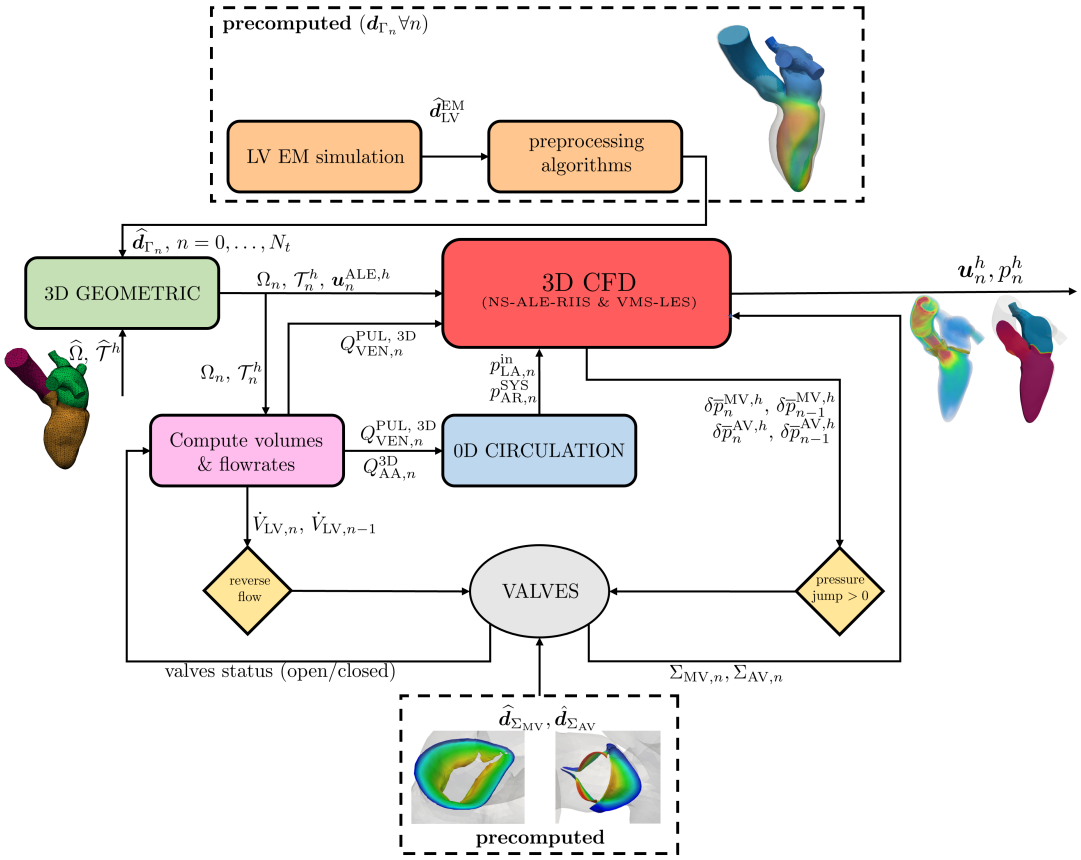

Figure 12: Coupling scheme among 3D geometric, 0D circulation and 3D CFD problems for the LH model at time step n (segregated scheme).

Flowrates are computed hinging upon mass balance and volumes time derivatives are discretized with backward finite differences.

We gather the problems in Eq. (40l)-(40n), discretized as in Section 5.3, as

$$(\boldsymbol{c}_n, \tilde{\boldsymbol{c}}_n)^T = \textsc{Circulation}(Q_{\mathrm{VEN},n}^{\mathrm{PUL,\ 3D}}, Q_{\mathrm{AA},n}^{\mathrm{3D}}), \tag{56}$$

where we highlight the dependency of the circulation problem on the fluxes $Q_{\mathrm{VEN},n}^{\mathrm{PUL,\ 3D}}, Q_{\mathrm{AA},n}^{\mathrm{3D}}$ computed in Algorithm 6. To solve the system of ODEs in Eq. (40l)-(40n), at every time step, the right-hand sides $\boldsymbol{r}(t_n, \boldsymbol{c}_n, \tilde{\boldsymbol{c}}_n)$ and $\tilde{\boldsymbol{r}}(t_n, \boldsymbol{c}_n)$ is fed with $Q_{\mathrm{VEN},n}^{\mathrm{PUL,\ 3D}}$ and $Q_{\mathrm{AA},n}^{\mathrm{3D}}$ as computed in Algorithm 6; in turn, the pressures $p_{\mathrm{AR},n}^{\mathrm{SYS}}$ and $p_{\mathrm{LA},n}^{\mathrm{in}}(t)$, computed in the 0D model, are used to prescribe BCs to the 3D CFD problem. We denote by $\mathcal{P}_{\text{NS-ALE-RIIS-VMS-LES}}$ the fluid-dynamics problem in Eq. (42):

$$\begin{aligned}\mathcal{P}_{\text{NS-ALE-RIIS-VMS-LES}}(\boldsymbol{u}_n^h,\, p_n^h;\, \boldsymbol{u}_n^{\mathrm{ALE},h};\, p_{\mathrm{LA},n}^{\mathrm{in}},\, Q_{\mathrm{VEN},n}^{\mathrm{PUL,\ 3D}},\, p_{\mathrm{AR},n}^{\mathrm{SYS}},\, \boldsymbol{d}_{\Gamma_n};\\ \Sigma_{\mathrm{MV},n},\, \Sigma_{\mathrm{AV},n},\, R_{\mathrm{MV}},\, R_{\mathrm{AV}},\, \varepsilon_{\mathrm{MV}},\, \varepsilon_{\mathrm{AV}};\, \Omega_n,\, \mathcal{T}_n^h) = 0,\end{aligned} \tag{57}$$

where we highlight the dependency of the problem on the ALE velocity $\boldsymbol{u}_n^{\mathrm{ALE},h}$, on quantities required to set BCs $(p_{\mathrm{LA},n}^{\mathrm{in}}, Q_{\mathrm{VEN},n}^{\mathrm{PUL,\ 3D}}, p_{\mathrm{AR},n}^{\mathrm{SYS}}, \boldsymbol{d}_{\Gamma_n})$ as in Eq. (40d), (40c), (40e) and (40f), on quantities required by the valves' RIIS modeling $(\Sigma_{\mathrm{MV},n}, \Sigma_{\mathrm{AV},n}, R_{\mathrm{MV}}, R_{\mathrm{AV}}, \varepsilon_{\mathrm{MV}}, \varepsilon_{\mathrm{AV}})$ as in Eq. (40a) and on the domain and mesh at current time step $(\Omega_n, \mathcal{T}_n^h)$. $\mathcal{P}_{\text{NS-ALE-RIIS-VMS-LES}}$ denotes the numerical solution at time step n of the fluid dynamics problem made of the NS-ALE-RIIS equations with VMS-LES modeling. The whole procedure to

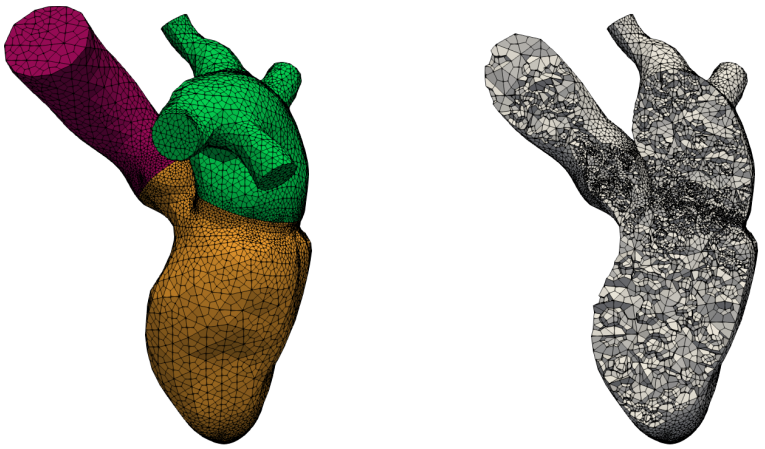

(a) (b)

Figure 13: The LH hexahedral mesh: (a) the mesh made of three conforming submeshes for LA, LV and AA; (b) a clip of the mesh showing the local mesh refinement near the MV and AV.

ρ	μ	R_k		ε_k		h			cells	DOFs ($\mathsf{Q}_1 - \mathsf{Q}_1$)		
[kg/m^3]	[kg/(m · s)]	[kg/(m^2·s)]		[10^{-3} m]		[10^{-3} m]			[10^3]	[10^3]		
		MV	AV	MV	AV	min	avg	max		$\boldsymbol{u}$	p	total
$1.06 \cdot 10^3$	$3.5 \cdot 10^{-3}$	10^4	10^4	1	1	0.79	2.3	5.2	157	534	178	712

Table 1: Parameters for the setup of the numerical simulations.

solve the fluid-dynamics problem is reported in Algorithm 7 and consists of solving Eq. (57) and computing the pressure jumps across valves. The algorithm is in short called as

$$\begin{aligned}\left(\boldsymbol{u}_n^h,\, p_n^h,\, \delta\overline{p}_n^{\mathrm{MV},h},\, \delta\overline{p}_n^{\mathrm{AV},h}\right)^T = \textsc{FluidDynamics}(&\boldsymbol{u}_n^{\mathrm{ALE},h}; p_{\mathrm{LA},n}^{\mathrm{in}}, Q_{\mathrm{VEN},n}^{\mathrm{PUL,\,3D}}, p_{\mathrm{AR},n}^{\mathrm{SYS}}, \boldsymbol{d}_{\Gamma_n};\\ &R_{\mathrm{MV}},\, R_{\mathrm{AV}},\, \varepsilon_{\mathrm{MV}},\, \varepsilon_{\mathrm{AV}}, \Sigma_{\mathrm{MV},n}, \Sigma_{\mathrm{AV},n};\\ &\Omega_n,\, \mathcal{T}_n^h).\end{aligned} \tag{58}$$

We solve the 3D-0D model in Eq. (40) by means of a segregated numerical scheme that we show in Algorithm 8. After initialization, at each time step we solve the geometric problem (Algorithm 3), we check the valves status through Algorithm 4, which – after checking positive pressure jumps and reversed flow conditions – returns the valves' opening-closing times $\boldsymbol{\tau}$. The latter is used to compute the flowrates (Algorithm 6). The flowrates $Q_{\mathrm{VEN},n}^{\mathrm{PUL,\,3D}}, Q_{\mathrm{AA},n}^{\mathrm{3D}}$, computed in the latter, are then used to assemble the right-hand side of Eq. (40l), (40m) (circulation problem). Finally, the pressures $p_{\mathrm{LA},n}^{\mathrm{in}}$, $p_{\mathrm{AR},n}^{\mathrm{SYS}}$ computed by the circulation problem and the flowrate $Q_{\mathrm{VEN},n}^{\mathrm{PUL,\,3D}}$ provided by the flowrates computation are used to set BCs of the fluid dynamics problem as described in Section 4.

In Figure 12 we report a conceptual scheme of the whole problem: from the precomputed quantities to the coupling among circulation and fluid dynamics problems. We highlight the central role played by the valves status determination and all the quantities shared among different the problems.

6 Numerical simulations

We perform numerical simulations on a LH mesh built from the Zygote Solid 3D heart model [51]. To preprocess the geometry and generate the mesh, we use vmtk [67] and the pre-processing tools recently developed in [69]. We mesh each portion of the domain (LA, LV and AA) separately with a non-uniform

mesh size, refining the mesh near the MV, AV and the LV apex, exploiting algorithms based on the closest-point distances [69]. The three submeshes are then connected in a conforming fashion to get the hexahedral mesh in Figure 13. Specifically, with `vmtk` we first generate a tetrahedral mesh, then we use `mesh tethex` [69, 71] to obtain an hexaedral mesh in which each tetrahedron is split into four hexaedra preserving the aspect ratio of the original element.

For the RIIS method, following arguments of [23, 37], we set $R_{\text{MV}} = R_{\text{AV}} = 10^4$ kg/(m^2·s) and $\varepsilon_{\text{MV}} = \varepsilon_{\text{AV}} = 10^{-3}$ m. This choice of ε_{MV} and ε_{AV} allows to have a physiologic representation of the valves' leaflets in a healthy subject and, with our choice of R_{MV} and R_{AV} to avoid flow penetration across the immersed surfaces [37]. As shown in Figure 13b, we have refined the mesh in the valves region in order to accurately represent the leaflets as described by the RIIS method with our choices of ε_{MV} and ε_{AV}. Since we neglect the isovolumetric phases, we cannot employ physiological opening and closing times of the valves, thus we open and close them instantaneously (i.e. in one time step). Thus, we set $\Delta\tau^0_{\text{MV}} = \Delta\tau^{\emptyset}_{\text{MV}} = \Delta\tau^0_{\text{AV}} = \Delta\tau^{\emptyset}_{\text{AV}} = \Delta t$.

The physical parameters for blood are density $\rho = 1.06 \cdot 10^3$ kg/m^3 and dynamic viscosity $\mu = 3.5 \cdot 10^{-3}$ kg/(m·s); we start our simulation from a zero velocity initial condition $\boldsymbol{u}_0 = \boldsymbol{0}$. We adopt linear FE spaces for velocity and pressures ($\mathbb{Q}_1 - \mathbb{Q}_1$), and In Table 1 we summarize the parameters adopted for the setup of our numerical simulations.

Mathematical models and numerical methods described in Sections 2, 3, 4 and 5 have been implemented in life$^{\text{x}}$ [66], a high-performance `C++` library developed within the iHEART project [3] mainly focused on cardiac simulations and based on the `deal.II` finite element core [72]. Numerical simulations are run in a parallel framework [4]. The linear system arising from Eq. (42) is solved at each time step with the GMRES method. The linear system is preconditioned with the aSIMPLE preconditioner [73] and its blocks are preconditioned with an algebraic multigrid preconditioner based on Trilinos [74].

In the following, we first present our numerical results for the case of a healthy LH, then we apply our computational model to the pathological case of MV regurgitation.

6.1 A physiological left heart

We simulate 4 heartbeats ($T_f = 4$ s) of period $T_{\text{HB}} = 1$ s and we discard the first 3 cycles in order to remove the influence of a null initial condition. We show numerical results on the last heartbeat and we shift the temporal domain in $[0, T_{\text{HB}}]$. We start our simulation from the time of end diastole, with the MV open and the AV closed. In Figure 14 we report flowrates and pressure at the inlet and outlet sections of the 3D domain, which are the interfaces of the 3D-0D coupling. In Figure 15 we show the average pressure in LA, LV and AA computed by averaging the pressure field in control volumes in each chamber, as explained in Section 3.5. On the bottom box, we report the LV volume time-derivative, which is the indicator adopted to check for reversed flow across a valve and hence to determine the valves' closing times. The MV closes at the beginning of the heartbeat when the flow becomes reverse on its section ($t = \tau^{\emptyset}_{\text{MV}}$, when $\dot{V}_{\text{LV}}$ becomes negative). The pressure in the LV starts rising and the AV opens when the pressure in the LV becomes larger than the one in the AA ($t = \tau^0_{\text{AV}}$, when $\overline{p}_{\text{LV}}$ becomes larger than $\overline{p}_{\text{AA}}$). This very time marks the beginning of the ejection phase in systole. In Figure 17a we report the volume rendering of the velocity magnitude and in 17b the pressure on a clip in the LV apico-basal direction. During the LV contraction, as shown in Figure 17a, box 2, the blood flows from the LV to the AA, reaching large values of velocity at the systolic peak $t = 0.134$ s. In particular, we measured a maximum flowrate in the AV section equal to 489.5 ml/s and a maximum systemic arterial pressure equal to 121.07 mmHg. The numerical results achieved are consistent with standard physiological data [75–77]: a peak systolic pressure in the range 119 ± 13 mmHg [77]; a maximum flowrate of about 489 ml/s [75].

Specifically on the ejection phase, as shown in Figure 18, during the acceleration phase (Figure 18, boxes 1 and 2), the spatial profile of the velocity field is almost flat, suggesting the development of a turbulent flow inside the AA. However, as the systolic peak is reached, the blood continues to flow from the LV to the AA (Figure 17a, box 3) but it decelerates; differently from the acceleration stage, the velocity profile is

[3] *iHEART - An Integrated Heart model for the simulation of the cardiac function*, European Research Council (ERC) grant agreement No 740132, P.I. Prof A. Quarteroni, 2017-2022.

[4] Numerical simulations were run either on the cluster iHEART (Lenovo SR950 8 x 24-Core Intel Xeon Platinum 8160, 2100 MHz and 1.7TB RAM) available at MOX, Dipartimento di Matematica, Politecnico di Milano and on the cluster GALILEO supercomputer (IBM NeXtScale cluster, 1022 nodes (Intel Broadwell), 2 x 18-Cores Intel Xeon E5-2697 v4 at 2.30 GHz, 36 cores/node, 26.572 cores in total with 128 GB/node) by CINECA.

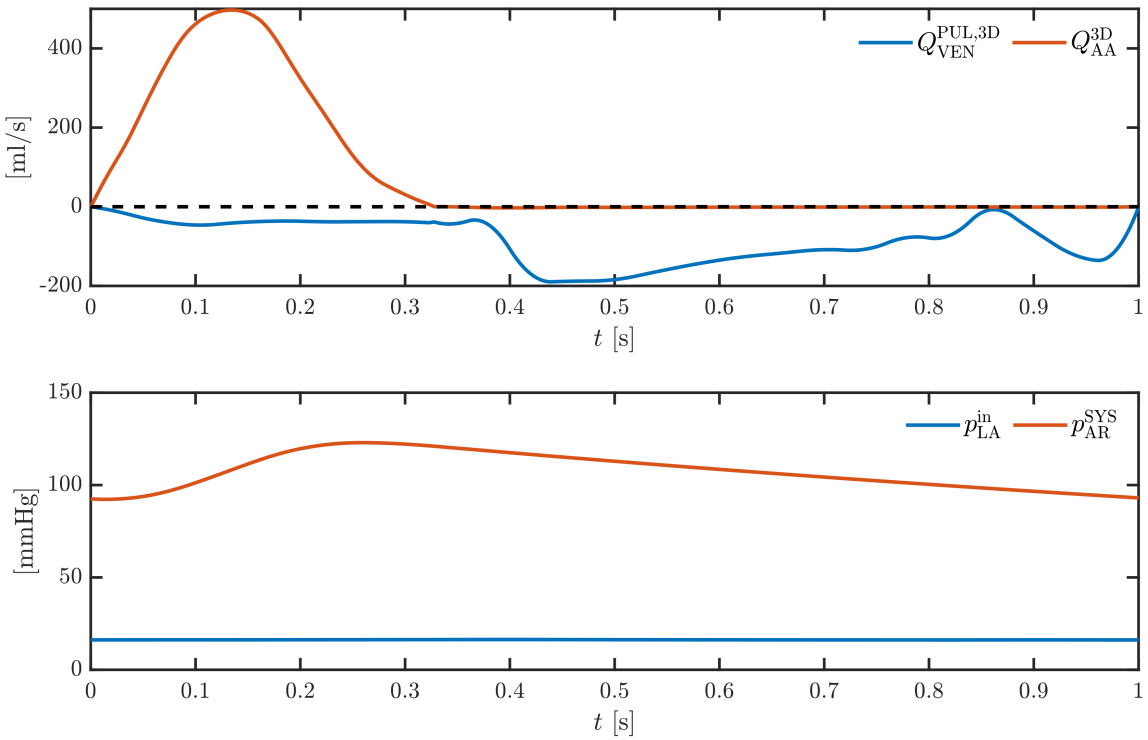

Figure 14: Flowrates (top) and pressures (bottom) at the interfaces of the 3D-0D model.

no longer flat but the flow is partially oriented towards the LV (Figure 18, boxes 3-6). The AV closes when the flow becomes completely reverse on its section ($t = \tau^{\emptyset}_{\mathrm{AV}}$, when $\dot{V}_{\mathrm{LV}}$ becomes positive). Once the AV is closed, the pressure in the LV suddenly decreases, until it becomes smaller than the one in the LA: this marks the beginning of diastole with the opening of the MV ($t = \tau^{0}_{\mathrm{MV}}$, when $\overline{p}_{\mathrm{LA}}$ becomes larger than $\overline{p}_{\mathrm{LV}}$). The diastole is characterized by two filling stages: the E-wave and the A-wave (Figure 17a, boxes 4, 5). As the E-wave starts ($t \approx 0.43$ s), a high-speed flux coming from the LA is observed at the MV section: the LV volume increases and the LA volume decreases. During the A-wave (atrial kick, $t \in [0.87, 1]$ s), we observe a rapid contraction of the LA, as also observed in Figures 8 (V_{LA}) and 14 ($Q^{\mathrm{PUL,\ 3D}}_{\mathrm{VEN}}$), producing a second high speed flux through the MV section, but milder than the one characterizing the E-wave. Once the atrial kick is over and a reverse flow condition is detected on the MV section, the MV closes at the beginning of a new heartbeat.

Figure 16 shows the computed LV pressure-volume (pV) loop. We correctly capture the standard shape of the LV pV loop in physiological conditions, obtaining and end diastolic volume EDV = 149.57 ml, end systolic volume ESV = 65.13 ml, stroke volume SV = EDV - ESV = 84.44 ml and the ejection fraction EF = 100 SV/EDV = 56.45%. The results obtained are consistent with values routinely acquired in healthy subjects [11, 78].

Figure 19 shows the velocity magnitude computed in our numerical simulations in a control volume immediately below the MV section. We compare our result with the velocity profile acquired through transmitral valve spectral Doppler in a normal subject from [79] (normally acquired in a sample volume between the mitral leaflet tips [80]). Specifically, we refer to Figure 4 of the paper [79]. We perform this comparison in diastole only (yellow boxes in Figure 19, bottom box), the peak obtained in systole is due to the blood flowing from the LV to the AA. We observe that our model is able to correctly reproduce the two characteristic waves in diastole, namely E-wave and A-wave: as for our reference data, the first wave shows a stronger peak than the second one. In the Doppler data, the E-wave and A-wave are characterized by amplitudes approximately equal to 1 m/s and 0.8 m/s; from the numerical results we get 0.97 m/s and 0.85 m/s respectively. We

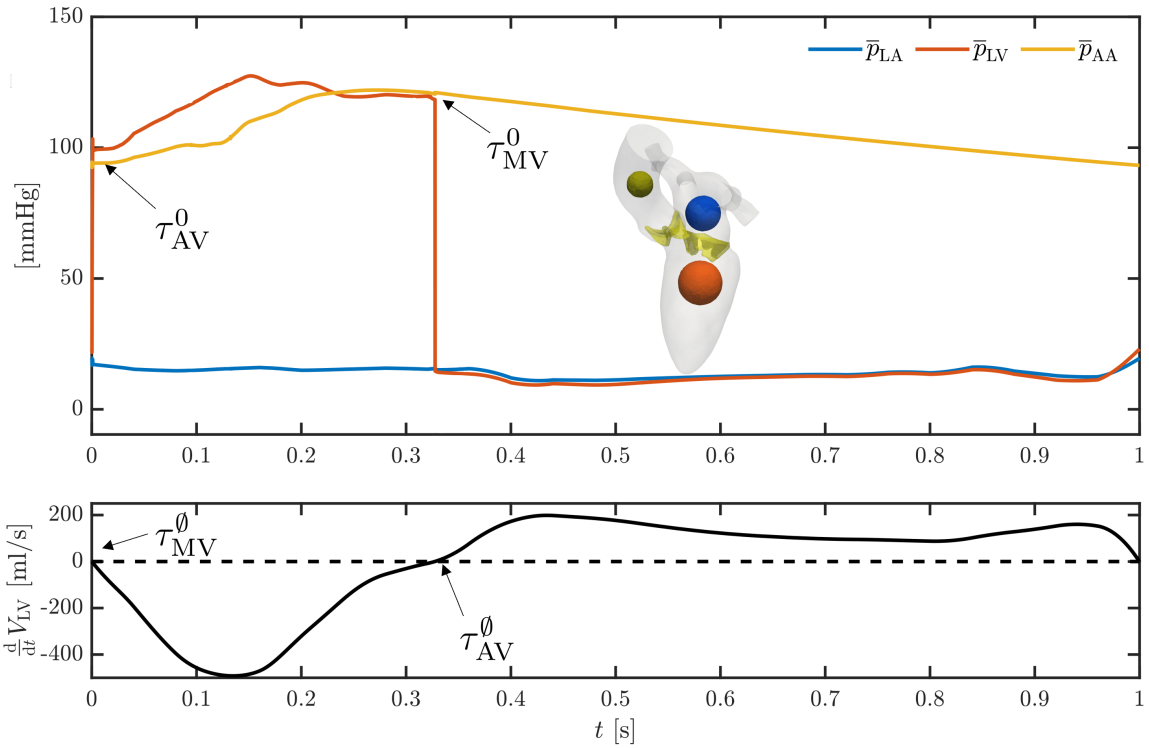

Figure 15: Flow properties to determine opening and closure of valves. Top: average pressure in LA, LV and AA; bottom: time derivative of LV volume. The pressure jumps among chambers determine the opening times of valves (τ^0_{MV}, τ^0_{AV}); the sign of LV volume time derivative determines a condition of reversed flow across the MV and the AV sections which defines valves closing times ($\tau^{\emptyset}_{\mathrm{MV}}$, $\tau^{\emptyset}_{\mathrm{AV}}$). Average pressures in the chambers are computed as in Eq. (27) in the control volumes shown in the LH on the top box.

compute an EA ratio equal to 1.14 (ratio among E-wave and A-wave peak velocities), which lays within the physiological range of EA $\in [0.75, 1.5]$ and is typical of young healthy subjects (EA > 1) [80, 81].

In Figure 20, we show the flowrate in the AA by reporting the computed flowrate in two different sections downind the AV. We compare our result with the flowrate in a normal AA acquired through cardiac magnetic resonance through-plane phase-contrast velocity mapping. Specifically, we compare our numerical results with Figure 3 of the paper [75]. By computing the flowrate at a section Γ^*_t downwind the AV and at the outlet section Γ^{AA}_t, we match accurately the systolic peak, with amplitudes 460.18 ml/s and 489.54 ml/s respectively on Γ^*_t and Γ^{AA}_t, against a peak approximately equal to 490 ml/s in the reference data. As diastole begins, the flow becomes reverse on the section considered, with a maximum amplitude equal to -12.04 ml/s and -2.79 ml/s on Γ^*_t and Γ^{AA}_t respectively. This pattern is also observed in the MR data even though with a larger amplitude.

We wish to point out that our numerical simulations are run on a template – even though realistic – geometry [51] and fed with data coming from EM simulations and 0D circulation model tuned for a generic healthy subject. Thus, from our analysis we can conclude that a qualitative good and satisfactory agreement can be found with the in-vivo results available in literature, making hence the whole computational model significant and reliable from an hemodynamic view point.

In order to identify coherent structures, we introduce the scalar function $\mathbb{Q}(\boldsymbol{u})$ defined as [82]

$$\mathbb{Q}(\boldsymbol{u}) = \frac{1}{2}\left(|\boldsymbol{\epsilon}(\boldsymbol{u})|^2_F - |\boldsymbol{\omega}(\boldsymbol{u})|^2_F\right),$$

where $\boldsymbol{\epsilon}(\boldsymbol{u})$ is the strain rate tensor introduced in Section 3.1, $\boldsymbol{\omega}(\boldsymbol{u}) = \frac{1}{2}\left(\nabla\boldsymbol{u} - \nabla^T\boldsymbol{u}\right)$ the rotation tensor

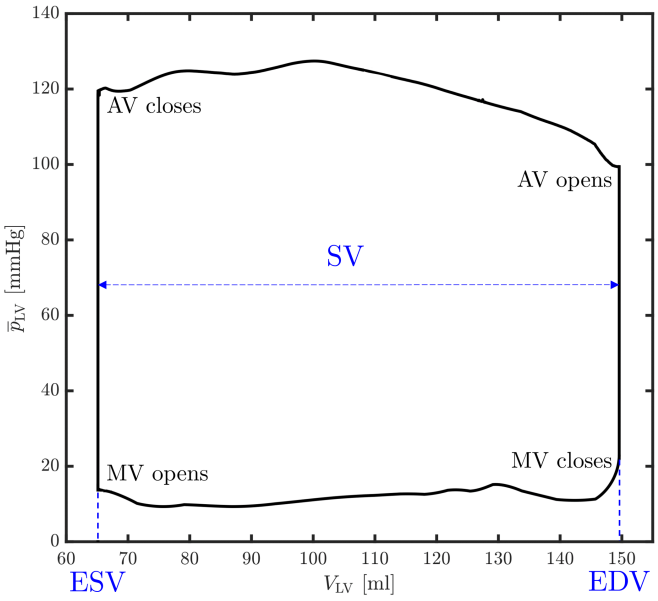

Figure 16: Computed LV pressure-volume loop.

and $|\cdot|_F$ the Frobenius norm of a tensor. The Q-criterion consists of analysing the iso-contours of the positive part of $\mathbb{Q}(\boldsymbol{u})$: when $\mathbb{Q}(\boldsymbol{u}) > 0$, the rotation of a fluid is predominant with respect to its stretching. In Figure 21 we show the iso-contours of Q-criterion with $\mathbb{Q}(\boldsymbol{u}) = 200\,\mathrm{s}^{-2}$ at different instants during the whole heartbeat. At the beginning of the heartbeat (box 1), we observe the residual vortical structures in the LH from late diastole. As the AV opens and the ejection phase starts, coherent structures are flushed out in the AA and the LV remains almost free. During systole, the LA is filled and coherent structures coming from the pulmonary veins impact in the middle of the LA, with still some visible structures at the end of systole (boxes 2-3). As the MV opens, in the LA we observe the formation of four vortex rings coming from the pulmonary veins. As in the systolic filling, they impact in the LA producing smaller and smaller coherent structures, during the E-wave and A-wave, as described in [8]. At the same time, during E-wave, a big vortex ring rolls through the MV leaflets. The observed organized vortical pattern observed rapidly evolves into a chaotic complex flow that fills the whole LV reaching its apex (box 5). During the A-wave, a new vortex under the MV section is formed, but weaker than the one seen during the E-wave (boxes 5-6). A new cycle begins, the MV closes, the vortex under its section is suddenly broken and, with the opening of the AV, all the coherent structures are flushed out again.

In each subfigure of Figure 22, we show on the left the projection of the vorticity on the normal direction of a slice in the LV apico-basal direction; on the right the iso-contours of Q-criterion with $\mathbb{Q}(\boldsymbol{u}) = 1500\,\mathrm{s}^{-2}$. Each subfigure represents a snapshot during early diastole. We observe the formation of shear layers on the leaflets of the MV producing different velocities on the two sides of the leaflets. Shear layers roll on MV leaflets and enter in the main cavity producing low-pressure circulation regions. The flow rotates in clockwise direction under the anterior leaflet, counterclockwise under the posterior, as shown in the projection of the vorticity in the slice's normal direction. This process characterizes the formation of the vortex ring that rolls through the MV leaflets (also shown in Figure 21, box 4), with a higher velocity in the inner part with respect to the exterior part of the ring. Once the vortex is formed, it evolves towards the LV apex and it breaks into smaller coherent structures. Figure 23 shows the streamlines colored according to the velocity magnitude and we compare our numerical results with 4D flow MRI visualizations. Specifically, we refer to the 4D flow MRI data available in Figure 3C of the paper [83] and Figure 4 of the paper [84] respectively. The numerical simulation well predicts the high speed jet across the MV and the formation of vortical flow under its section described by the 4D flow MRI data during the E-wave peak. Thus, our model captures the formation and the dynamic of the vortex ring (also referred to as "O vortex" [3, 17]) during diastole,

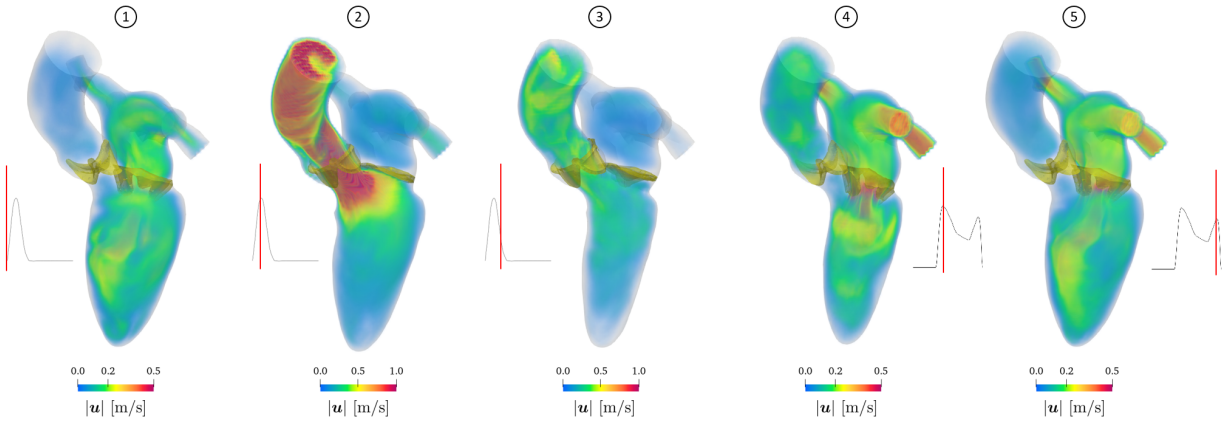

(a) velocity

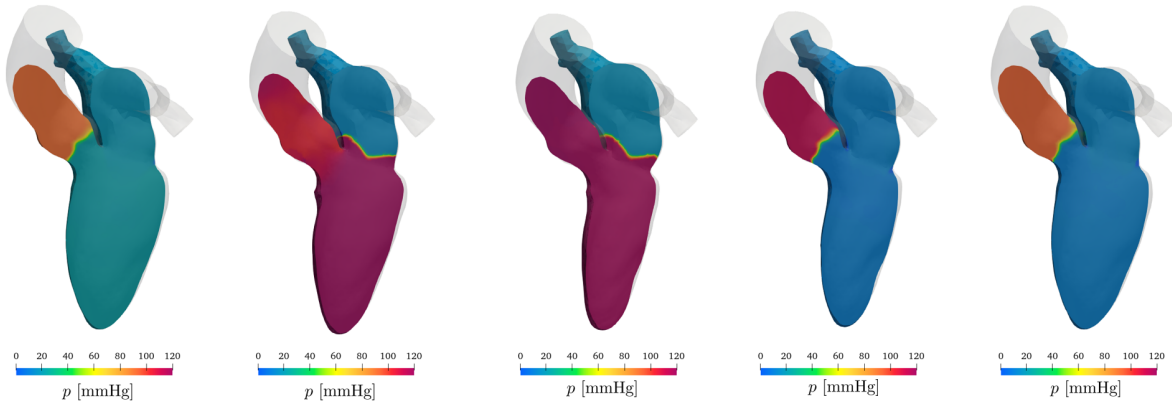

(b) pressure

Figure 17: Velocity and pressure fields during a whole heartbeat: (a) volume rendering of velocity magnitude; (b) pressure on a clip in the LV apico-basal direction. In boxes 1, 2, 3 the 1D plot shows Q_{AV}, in boxes 4 and 5 the MV flowrate Q_{MV}.

a well studied cardiac hemodynamic feature whose characteristics and interactions with LV wall provide information about the diastolic function [3, 85–87].

6.2 The case of MV regurgitation

We now employ our model to investigate primary mitral valve regurgitation. In particular, we mimic the presence of MV regurgitation by redefining $\widehat{\boldsymbol{d}}_{\Sigma_{\mathrm{MV}}}(\boldsymbol{x})$ to get the displacement field displayed in Figure 24. Due to the mitral regurgitant flow, an amount of blood flows from the LV to the LA during systole. Therefore, the flowrate at the aortic outlet can no longer be computed exploiting mass balance as in Eq. (34). Thus, for the coupling with the 0D circulation model we compute the outlet flowrate as

$$Q_{\mathrm{AA}}^{\mathrm{3D}}(t) = \int_{\Gamma_t^{\mathrm{AA}}} \boldsymbol{u} \cdot \boldsymbol{n} \mathrm{d}\boldsymbol{x}. \tag{59}$$

We introduce the mitral regurgitant flow $Q_{\mathrm{MV}}^{\mathrm{reg}}(t)$ as the amount of blood that flows from the LV into the LA during systole:

$$Q_{\mathrm{MV}}^{\mathrm{reg}}(t) = \begin{cases} 0 & \text{if MV in open configuration,} \\ -\dfrac{\mathrm{d}}{\mathrm{d}t}\left(V_{\mathrm{LV}}(t) + V_{\mathrm{AA}}(t)\right) - Q_{\mathrm{AA}}^{\mathrm{3D}}(t) & \text{if MV in closed (regurgitant) configuration.} \end{cases} \tag{60}$$

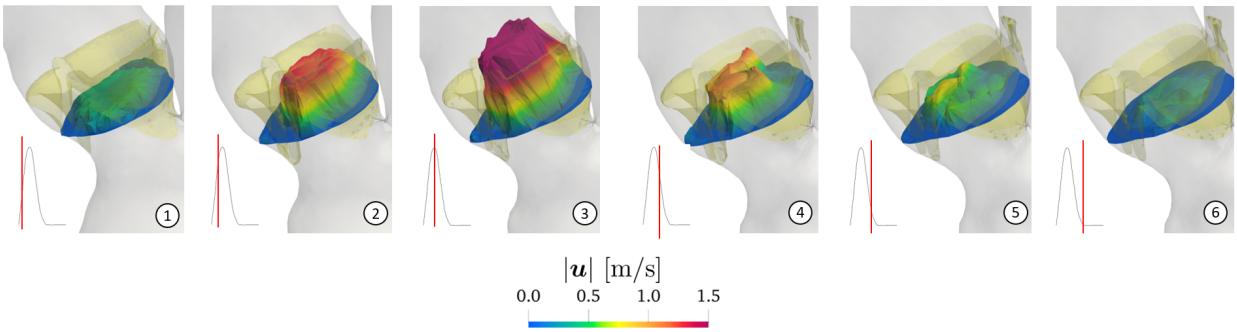

Figure 18: Snapshots of velocity profile at the AV section during systole. The 1D plot shows Q_{AV}.

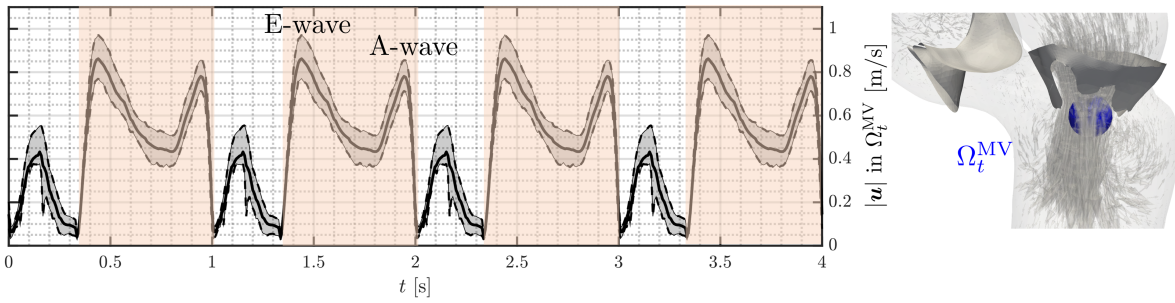

Figure 19: Average, first and third quartile of velocity magnitude in a control volume under the MV section.

The inlet flowrate accounts for MV regurgitation by modifing its definition with respect to the physiological case as

$$Q_{\mathrm{VEN}}^{\mathrm{PUL,\ 3D}}(t) = \begin{cases} -\dfrac{\mathrm{d}\left(V_{\mathrm{LV}}(t) + V_{\mathrm{LA}}(t)\right)}{\mathrm{d}t} & \text{if MV in open configuration,} \\ -\dfrac{\mathrm{d}V_{\mathrm{LA}}(t)}{\mathrm{d}t} - Q_{\mathrm{MV}}^{\mathrm{reg}}(t) & \text{if MV in closed (regurgitant) configuration.} \end{cases} \tag{61}$$

The new definitions (59) and (61) replace the corresponding quantities in the coupling conditions and in the setting of BCs in Eq. (32) and Eq. (34). Moreover, the AV flow no longer matches the LV volume time derivative when the AV is open. Thus, a condition of reversed flow across the AV section – which marks the closure of the AV – is now detected by checking the sign of the following quantity:

$$-\frac{\mathrm{d}V_{\mathrm{LV}}(t)}{\mathrm{d}t} - Q_{\mathrm{MV}}^{\mathrm{reg}}(t). \tag{62}$$

Figure 25a shows the volume rendering of velocity magnitude during systole: a high-speed jet flows from the LV to the LA (reversed flow) and a weaker jet is observed in the AA with respect to the healthy case. To better focus on the strong systolic jets, in Figure 25b we report a contour surface of the velocity magnitude ($|\boldsymbol{u}| = 0.5$ m/s) colored according to pressure. As systole starts at $t = 0.036$ s, the blood flows from the LV to the LA, accelerates towards the LA endocardium and it impinges on the latter thus yielding higher pressure.

Figure 26 reports the flowrates at inlet and outlet sections for the healthy and the pathological cases along with the mitral regurgitant flow. Particularly, we measure a maximum $Q_{\mathrm{MV}}^{\mathrm{reg}}$ equal to 177.50 ml/s and a peak $Q_{\mathrm{AA}}^{\mathrm{3D}}$ of 328.94 ml/s, against the aortic flow of 489.54 ml/s measured in the healthy case. Furthermore, we observe that, due to the presence of the mitral regurgitant flow, the inlet flowrate $Q_{\mathrm{VEN}}^{\mathrm{PUL,\ 3D}}$ becomes negative during systole, thus inducing a reversal pulmonary venous flow. This phenomenon is also observed by clinicians in the case of MV regurgitation and it is a routinely employed indicator to grade its severity [88].

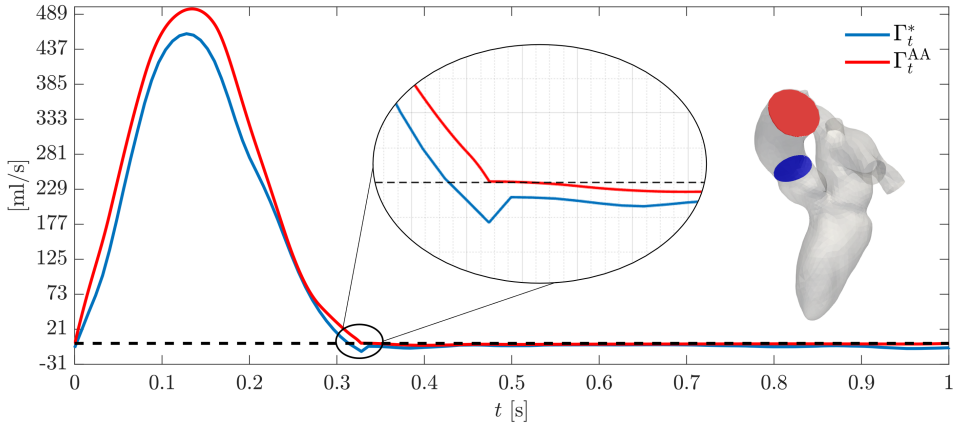

Figure 20: Flowrate computed on a section downwind the AV ($\int_{\Gamma_t^*} \boldsymbol{u}\cdot\boldsymbol{n}$) and on the outlet section ($Q_{\mathrm{AA}}^{\mathrm{3D}}(t) = \int_{\Gamma_t^{\mathrm{AA}}} \boldsymbol{u}\cdot\boldsymbol{n}$)

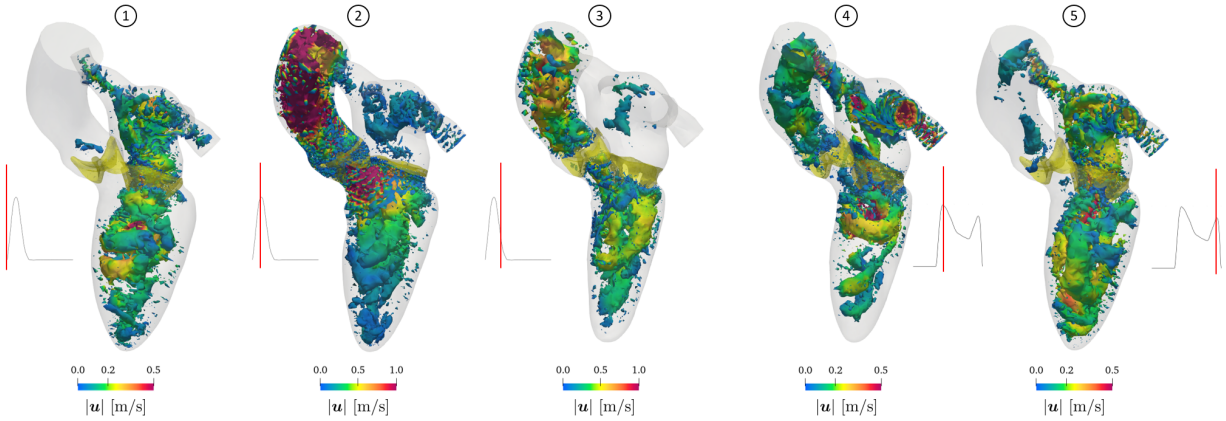

Figure 21: Iso-contours of Q-criterion ($\mathbb{Q}(\boldsymbol{u}) = 200\,\mathrm{s}^{-2}$) colored with velocity magnitude during a whole heartbeat. In boxes 1, 2, 3 the 1D plot shows Q_{AV}, in boxes 4 and 5 Q_{MV}.

Our numerical results allow to estimate additional hemodynamic indicators as the WSS. In particular, we compute the time averaged wall shear stress (TAWSS) in a heartbeat as [89]:

$$\mathrm{TAWSS}(\boldsymbol{u}) = \frac{1}{T_{\mathrm{HB}}}\int_0^{T_{\mathrm{HB}}} |\mathbf{WSS}(\boldsymbol{u})|\mathrm{d}t \quad \text{on } \partial\widehat{\Omega},$$

being

$$\mathbf{WSS}(\boldsymbol{u}) = \boldsymbol{T}(\boldsymbol{u})\widehat{\boldsymbol{n}} - (\boldsymbol{T}(\boldsymbol{u})\widehat{\boldsymbol{n}}\cdot\widehat{\boldsymbol{n}})\,\widehat{\boldsymbol{n}} \quad \text{on } \partial\widehat{\Omega}, \tag{63}$$

and $\boldsymbol{T}(\boldsymbol{u}) = 2\mu\boldsymbol{\epsilon}(\boldsymbol{u})$. In Figure 27a we report the TAWSS on the LH geometry and we compare the healthy (left) and the mitral valve regurgitation (right) scenarios. In the case of valvular insufficiency we observe large values of TAWSS (up to 2.54 Pa) on the top of the LA due to the high speed retrograde flow that impinges the LA endocardium. At the same time, as shown in Figure 27b, due to a lower amount of blood flowing from the LV to the systemic arterial system, a milder interaction between the jet and the wall of the AA is reported as shown by lower values of TAWSS in the AA.

Eventually, we compute two mitral valve regurgitation indicators: the regurgitant volume (RVol) and the regurgitant fraction (RF). These indicators are routinely computed in the clinical practice via the Proximal Isovelocity Surface Area (PISA) method, an ecocardiographic technique based on conservation of mass which however relies on several limiting assumptions [90]. On the contrary, numerical simulations allow to

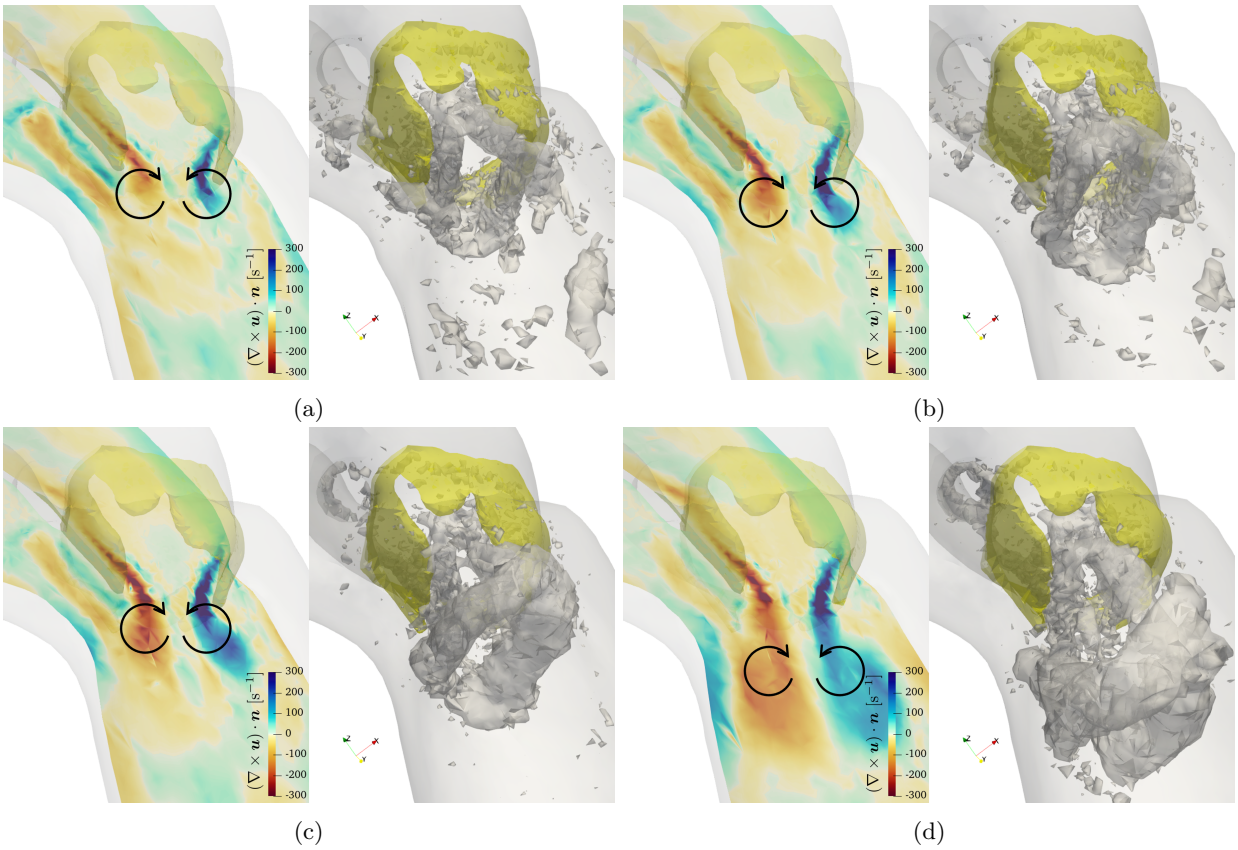

Figure 22: Formation of ring shaped vortex during early diastole. In each subfigure: on the left, projection of the vorticity on the normal direction (pointing towards the reader) of a slice in the LV apico-basal direction; on the right: the Q-criterion with $\mathbb{Q}(\boldsymbol{u}) = 1500\,\mathrm{s}^{-2}$ to identify the vortex.

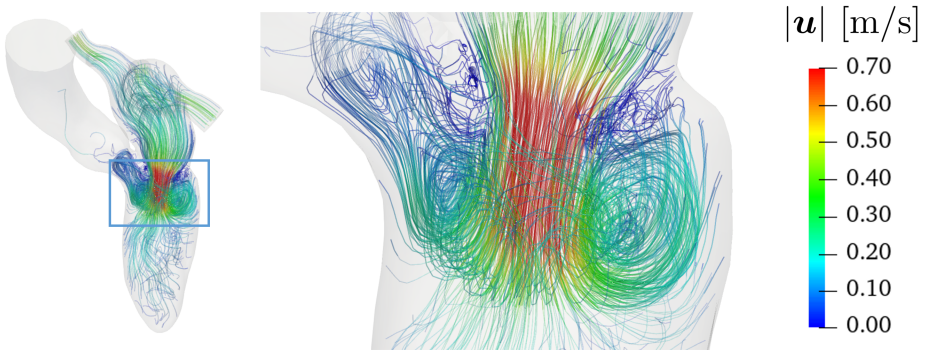

Figure 23: Streamlines colored according to velocity magnitude at early diastolic peak (E-wave).

accurately estimate these indicators without the need of hypotheses considered in the PISA method. We compute RVol as the amount of blood flowing from the LV to the LA in a heartbeat by integrating in time the regurgitant flowrate, as

$$\mathrm{RVol} = \int_0^{T_{\mathrm{HB}}} Q_{\mathrm{MV}}^{\mathrm{reg}}(t)\mathrm{d}t. \tag{64}$$

The RF is defined as the ratio among the RVol and the stroke volume SV [90]. For this proof of concept

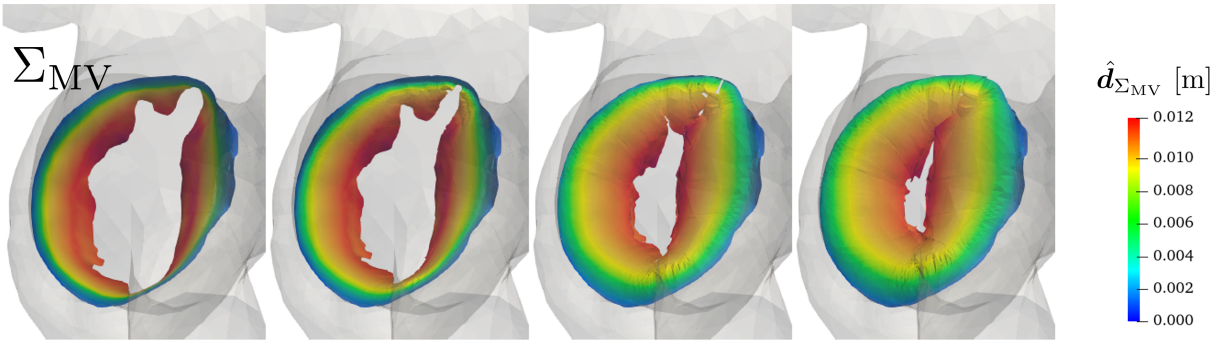

Figure 24: MV: from fully open to closed (regurgitant) configuration. Leaflets are deformed with the displacement $\widehat{\boldsymbol{d}}_{\Sigma_{\mathrm{MV}}}$.

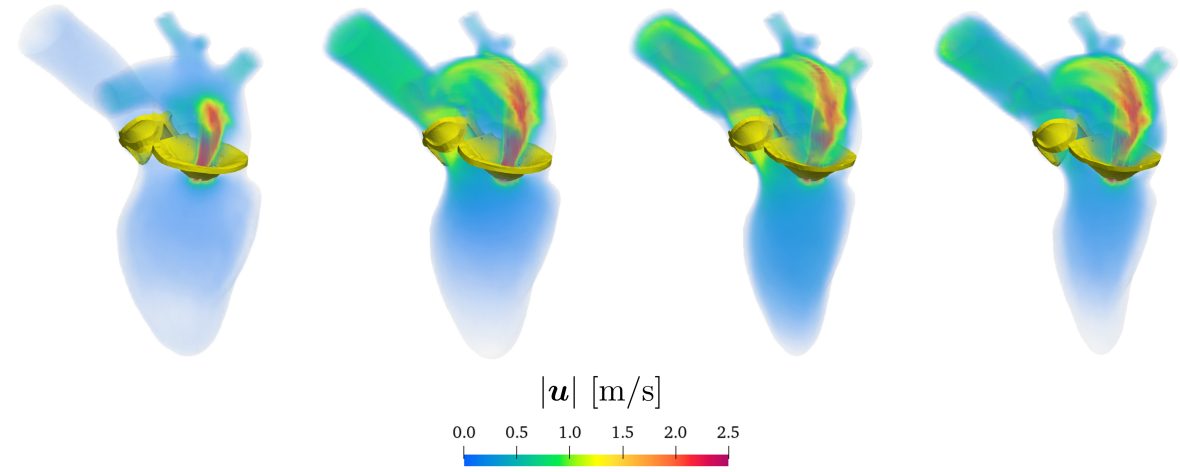

(a) velocity

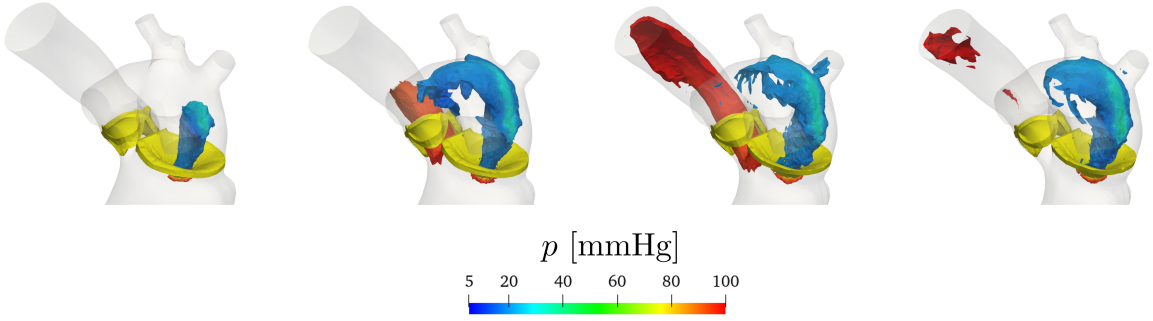

(b) pressure

Figure 25: Flow field for the regurgitant mitral valve during systole: (a) volume rendering of velocity magnitude; (b) contour surface of velocity magnitude ($|\boldsymbol{u}| = 0.5$ m/s) colored according to pressure.

simulation, we get RVol = 47.07 ml/s and RF = 55.74 %, values which would indicate a severe mitral valve regurgitation [91].

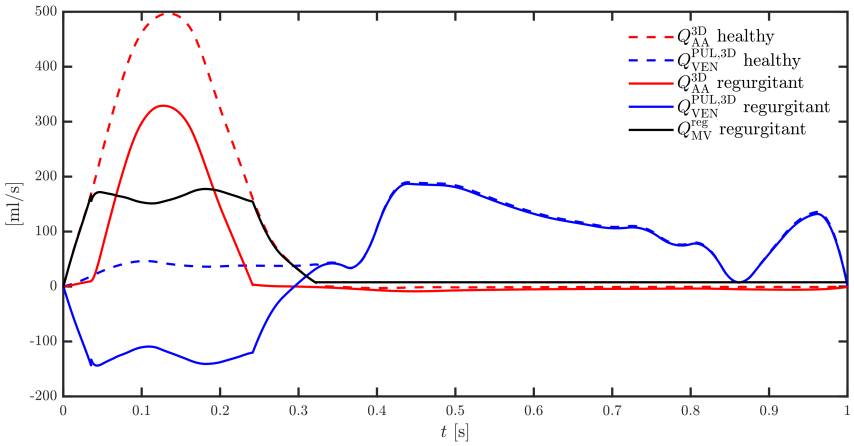

Figure 26: Flowrates at inlet and outlet sections: comparison between healthy and MV regurgitation case.

7 Conclusions and future developments

We propose a computational model for the detailed analysis of the left heart hemodynamics, accounting for the displacement of the domain boundary, the motion of the aortic and mitral valve, the dynamics of the circulatory system, and transition to turbulence effects. We carry out an electromechanical simulation of the left ventricle and, for the description of the motion over the whole domain boundary, we introduce an extension procedure and a volume-based displacement definition on the atrium. The 3D CFD model of the left heart consists of the Navier-Stokes equations in an Arbitrary Lagrangian Eulerian framework, with valves accounted for by means of the Resistive Immersed Implicit Surface method. We couple the 3D CFD model to a closed-loop 0D circulation model of the whole cardiovascular system.

We simulate the blood flow in the left heart in physiological conditions by means of the proposed methodology. The results are analyzed in terms of flow and pressure distribution, velocity profiles through the valves, and turbulent coherent structures. Biomarkers such as the pressure-volume loop, the stroke volume, the ejection fraction, the EA ratio and the pressure peaks are compared with the literature and accurately reproduced; a comparison with Doppler echocardiography data and 4D flow magnetic resonance imaging allows to validate the computational model. As a proof of concept, we apply the geometric multiscale model to the case of a mitral valve regurgitation, estimating several clinical indicators and comparing the wall shear stress distribution with the healthy case.

Different further directions of investigation will be considered. Introducing an electromechanical model of the complete left heart would complete the description of the cardiac contractility and hence allow to relax some of the hypotheses we made on the atrium motion. In addition, in the present work we prescribe the electromechanics-based displacement on the boundary of the fluid dynamics system, hence enforcing a kinematic coupling condition among the two physics. Since we are neglecting the dynamic balance, the pressure would not be uniquely defined when both valves are closed. Thus, we discard the isovolumetric phases of the heart cycle. As done in [50], one could circumvent this issue by introducing an additional penalty term in the Navier-Stokes equations to control the intraventricular pressure during the isovolumetric phases. Moreover, patient-specific studies could be undertaken, with a reconstruction of the geometry and displacement of the domain from diagnostic imaging data. From a numerical point of view, we found that the stability of the numerical scheme requires a small time step during systole, the phase of the heartbeat characterized by larger velocity values. We envision that the computational cost of a cardiac fluid dynamics simulation might be reduced by employing an adaptive time-advancing numerical scheme. As a matter of fact, adaptivity would allow to use a larger time step size in diastole while satisfying the small time step requirements of systole.

The novelty of the paper is threefold. First, we introduce an original preprocessing procedure that combines i) an extension of a given left ventricular displacement on the whole left heart by means of Laplace-Beltrami equations with physiological kinematic constraints; ii) a reduced model for the motion of the atrium

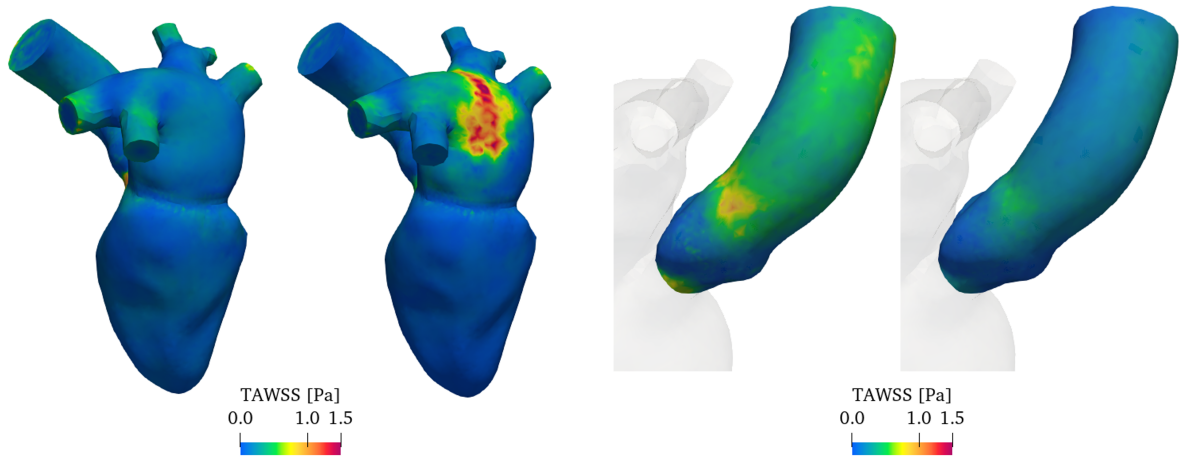

(a) Front view (b) Focus on the AA

Figure 27: Comparison of TAWSS in physiologic and mitral valve regurgitation case: (a) front view of the LH (b) focus on the AA. In each subfigure: on the left the healthy case, on the right the mitral valve regurgitation.

based on the volume variation dictated by a lumped-parameter circulation model. This yields an integrated system in which fluid dynamics is one-way coupled to electromechanics in the left ventricle. The extension procedure can also be employed to merge displacement fields coming from different sources, such as a reconstruction from diagnostic images, and may, thus, be applied also to patient-specific studies. As the imaging data routinely acquired in diagnostic exams is often focused on the ventricle, the extension procedure that we propose can be used to complete the missing data.

Second, we devise a coupled 3D-0D model made of the 3D CFD model of the left heart and a 0D circulation model of the whole cardiovascular system. We solve the coupled model with a segregated scheme and we develop computational strategies to solve the integrated system made of fluid dynamics, displacement, valves and circulation.

Third, we found that our numerical simulations yielded a qualitative and quantitative good agreement with clinical data from different sources, making the whole integrated multiscale model significant and realiable from an hemodynamics view point. Furthermore, the flexibility of the model also allowed to simulate pathological scenarios.

To conclude, the present work can be viewed as a significant step forward to simulate the hemodynamics of the whole human heart coupled to the external pulmonary and systemic circulation: a challenging task that might be reached with intermediate stages.

Acknowledgments

This work has been supported by the ERC Advanced Grant iHEART, "An Integrated Heart Model for the simulation of the cardiac function", 2017–2022, P.I. A. Quarteroni (ERC–2016– ADG, project ID: 740132). We gratefully acknowledge the CINECA award under the ISCRA B initiative, for the availability of high performance computing resources and support under the project HP10BD303V, P.I. A. Quarteroni, 2020-2021.

References

[1]M. T. Ngo, C. I. Kim, J. Jung, G. H. Chung, D. H. Lee, and H. S. Kwak, "Four-dimensional flow magnetic resonance imaging for assessment of velocity magnitudes and flow patterns in the human carotid artery bifurcation: comparison with computational fluid dynamics", Diagnostics **9**, 223 (2019).

[2]A. Quarteroni, L. Dede', A. Manzoni, and C. Vergara, *Mathematical modelling of the human cardiovascular system: data, numerical approximation, clinical applications*, Vol. 33 (Cambridge University Press, 2019).

[3]C. Chnafa, S. Mendez, and F. Nicoud, "Image-based large-eddy simulation in a realistic left heart", Computers & Fluids **94**, 173–187 (2014).

[4]S. Zhao, P. Papathanasopoulou, Q. Long, I. Marshall, and X. Xu, "Comparative study of magnetic resonance imaging and image-based computational fluid dynamics for quantification of pulsatile flow in a carotid bifurcation phantom", Annals of Biomedical Engineering **31**, 962–971 (2003).

[5]D. I. Hollnagel, P. E. Summers, D. Poulikakos, and S. S. Kollias, "Comparative velocity investigations in cerebral arteries and aneurysms: 3d phase-contrast MR angiography, laser doppler velocimetry and computational fluid dynamics", NMR in Biomedicine: An International Journal Devoted to the Development and Application of Magnetic Resonance In vivo **22**, 795–808 (2009).

[6]D. Bluestein and S. Einav, "Transition to turbulence in pulsatile flow through heart valves—a modified stability approach", Journal of biomechanical engineering **116**, 477–487 (1994).

[7]A. Verkaik, A. Bogaerds, F. Storti, and F. Van De Vosse, "A coupled overlapping domain method for the computation of transitional flow through artificial heart valves", in ASME 2012 summer bioengineering conference (SBC 2012) (American Society of Mechanical Engineers, 2012), pp. 217–218.

[8]A. Zingaro, L. Dede', F. Menghini, and A. Quarteroni, "Hemodynamics of the heart's left atrium based on a variational multiscale-les numerical method", European Journal of Mechanics-B/Fluids **89**, 380–400 (2021).

[9]I. E. Vignon-Clementel, C. Figueroa, K. Jansen, and C. Taylor, "Outflow boundary conditions for 3D simulations of non-periodic blood flow and pressure fields in deformable arteries", Computer methods in biomechanics and biomedical engineering **13**, 625–640 (2010).

[10]F. Viola, V. Spandan, V. Meschini, J. Romero, M. Fatica, M. D. de Tullio, and R. Verzicco, "FSEI-GPU: GPU accelerated simulations of the fluid-structure-electrophysiology interaction in the left heart", arXiv preprint arXiv:2103.15187 (2021).

[11]F. Viola, V. Meschini, and R. Verzicco, "Fluid–Structure-Electrophysiology interaction (FSEI) in the left-heart: a multi-way coupled computational model", European Journal of Mechanics-B/Fluids **79**, 212–232 (2020).

[12]E. Karabelas, M. A. Gsell, C. M. Augustin, L. Marx, A. Neic, A. J. Prassl, L. Goubergrits, T. Kuehne, and G. Plank, "Towards a computational framework for modeling the impact of aortic coarctations upon left ventricular load", Frontiers in physiology **9**, 538 (2018).

[13]F. Viola, V. Meschini, and R. Verzicco, "Effects of stenotic aortic valve on the left heart hemodynamics: a fluid-structure-electrophysiology approach", arXiv preprint arXiv:2103.14680 (2021).

[14]Y. J. Choi, J. Constantino, V. Vedula, N. Trayanova, and R. Mittal, "A new MRI-based model of heart function with coupled hemodynamics and application to normal and diseased canine left ventricles", Frontiers in bioengineering and biotechnology **3**, 140 (2015).

[15]A. Gerbi, "Numerical approximation of cardiac electro-fluid-mechanical models: coupling strategies for large-scale simulation", PhD thesis (Ecole Polytechnique Fédérale de Lausanne, 2018).

[16]A. Tagliabue, L. Dede', and A. Quarteroni, "Fluid dynamics of an idealized left ventricle: the extended Nitsche's method for the treatment of heart valves as mixed time varying boundary conditions", International Journal for Numerical Methods in Fluids **85**, 135–164 (2017).

[17]L. Dede', F. Menghini, and A. Quarteroni, "Computational fluid dynamics of blood flow in an idealized left human heart", International Journal for Numerical Methods in Biomedical Engineering, `10.1002/cnm.3287` (2019).

[18]A. Tagliabue, L. Dede', and A. Quarteroni, "Complex blood flow patterns in an idealized left ventricle: a numerical study", Chaos: An Interdisciplinary Journal of Nonlinear Science **27**, 093939 (2017).

[19]F. Domenichini, G. Pedrizzetti, and B. Baccani, "Three-dimensional filling flow into a model left ventricle", Journal of Fluid Mechanics **539**, 179 (2005).

[20]B. Baccani, F. Domenichini, and G. Pedrizzetti, "Vortex dynamics in a model left ventricle during filling", European Journal of Mechanics-B/Fluids **21**, 527–543 (2002).

[21]X. Zheng, J. Seo, V. Vedula, T. Abraham, and R. Mittal, "Computational modeling and analysis of intracardiac flows in simple models of the left ventricle", European Journal of Mechanics-B/Fluids **35**, 31–39 (2012).

[22]J. H. Seo and R. Mittal, "Effect of diastolic flow patterns on the function of the left ventricle", Physics of Fluids **25**, 110801 (2013).

[23]I. Fumagalli, M. Fedele, C. Vergara, L. Dede', S. Ippolito, F. Nicolò, C. Antona, R. Scrofani, and A. Quarteroni, "An image-based computational hemodynamics study of the systolic anterior motion of the mitral valve", Computers in Biology and Medicine **123**, 103922 (2020).

[24]A. This, H. G. Morales, O. Bonnefous, M. A. Fernández, and J.-F. Gerbeau, "A pipeline for image based intracardiac CFD modeling and application to the evaluation of the PISA method", Computer Methods in Applied Mechanics and Engineering **358**, 112627 (2020).

[25]A. Masci, L. Barone, L. Dede', M. Fedele, C. Tomasi, A. Quarteroni, and C. Corsi, "The impact of left atrium appendage morphology on stroke risk assessment in atrial fibrillation: a computational fluid dynamics study", Frontiers in Physiology **9**, `10.3389/fphys.2018.01938` (2019).

[26]A. Masci, M. Alessandrini, D. Forti, F. Menghini, L. Dedé, C. Tomasi, A. Quarteroni, and C. Corsi, "A patient-specific computational fluid dynamics model of the left atrium in atrial fibrillation: development and initial evaluation", in International conference on functional imaging and modeling of the heart (Springer, 2017), pp. 392–400.

[27]A. Masci, M. Alessandrini, D. Forti, F. Menghini, L. Dedé, C. Tomasi, A. Quarteroni, and C. Corsi, "A proof of concept for computational fluid dynamic analysis of the left atrium in atrial fibrillation on a patient-specific basis", Journal of Biomechanical Engineering **142** (2020).

[28]A. Quarteroni, A. Veneziani, and C. Vergara, "Geometric multiscale modeling of the cardiovascular system, between theory and practice", Computer Methods in Applied Mechanics and Engineering **302**, 193–252 (2016).

[29]P. J. Blanco and R. A. Feijoo, "A 3D-1D-0D computational model for the entire cardiovascular system", Mecanica Computacional **24**, 5887–5911 (2010).

[30]Y. Shi and T. Korakianitis, "Numerical simulation of cardiovascular dynamics with left heart failure and in-series pulsatile ventricular assist device", Artificial organs **30**, 929–948 (2006).

[31]V. Milišić and A. Quarteroni, "Analysis of lumped parameter models for blood flow simulations and their relation with 1D models", ESAIM: Mathematical modelling and numerical analysis **38**, 613–632 (2004).

[32]H. J. Kim, I. E. Vignon-Clementel, C. A. Figueroa, J. F. LaDisa, K. E. Jansen, J. A. Feinstein, and C. A. Taylor, "On coupling a lumped parameter heart model and a three-dimensional finite element aorta model", Annals of biomedical engineering **37**, 2153–2169 (2009).

[33]F. N. Van de Vosse and N. Stergiopulos, "Pulse wave propagation in the arterial tree", Annual Review of Fluid Mechanics **43**, 467–499 (2011).

[34]L. Formaggia, D. Lamponi, and A. Quarteroni, "One-dimensional models for blood flow in arteries", Journal of engineering mathematics **47**, 251–276 (2003).

[35]L. Formaggia, J.-F. Gerbeau, F. Nobile, and A. Quarteroni, "On the coupling of 3D and 1D Navier–Stokes equations for flow problems in compliant vessels", Computer methods in applied mechanics and engineering **191**, 561–582 (2001).

[36]Y. Shi, P. Lawford, and R. Hose, "Review of zero-D and 1-D models of blood flow in the cardiovascular system", Biomedical engineering online **10**, 1–38 (2011).

[37]M. Fedele, E. Faggiano, L. Dede', and A. Quarteroni, "A patient-specific aortic valve model based on moving resistive immersed implicit surfaces", Biomechanics and Modeling in Mechanobiology **16**, 1779–1803 (2017).

[38]Y. Bazilevs, V. Calo, J. Cottrell, T. Hughes, A. Reali, and G. Scovazzi, "Variational multiscale residual-based turbulence modeling for large eddy simulation of incompressible flows", Computer Methods in Applied Mechanics and Engineering **197**, 173–201 (2007).

[39]D. Forti and L. Dede', "Semi-implicit BDF time discretization of the Navier–Stokes equations with VMS-LES modeling in a high performance computing framework", Computers & Fluids **117**, 168–182 (2015).

[40]F. Regazzoni, M. Salvador, P. C. Africa, M. Fedele, L. Dede, and A. Quarteroni, "A cardiac electromechanics model coupled with a lumped parameters model for closed-loop blood circulation. Part I: model derivation", arXiv preprint arXiv:2011.15040 (2020).

[41]F. Regazzoni, M. Salvador, P. C. Africa, M. Fedele, L. Dede, and A. Quarteroni, "A cardiac electromechanics model coupled with a lumped parameters model for closed-loop blood circulation. Part II: numerical approximation", arXiv preprint arXiv:2011.15051 (2020).

[42]M. Hirschvogel, M. Bassilious, L. Jagschies, S. M. Wildhirt, and M. W. Gee, "A monolithic 3D-0D coupled closed-loop model of the heart and the vascular system: experiment-based parameter estimation for patient-specific cardiac mechanics", International Journal for Numerical Methods in Biomedical Engineering **33**, e2842 (2017).

[43]L. Formaggia and F. Nobile, "A stability analysis for the arbitrary Lagrangian Eulerian formulation with finite elements", East-West Journal of Numerical Mathematics **7**, 105–131 (1999).

[44]K. Perktold, E. Thurner, and T. Kenner, "Flow and stress characteristics in rigid walled and compliant carotid artery bifurcation models", Medical & biological engineering & computing **32**, 19–26 (1994).

[45]C. A. Taylor, T. J. Hughes, and C. K. Zarins, "Finite element analysis of pulsatile flow in the abdominal aorta under resting and exercise conditions", ASME-PUBLICATIONS-BED **33**, 81–82 (1996).

[46]C. A. Taylor, T. J. Hughes, and C. K. Zarins, "Finite element modeling of blood flow in arteries", Computer methods in applied mechanics and engineering **158**, 155–196 (1998).

[47]F. Duarte, R. Gormaz, and S. Natesan, "Arbitrary Lagrangian–Eulerian method for Navier–Stokes equations with moving boundaries", Computer Methods in Applied Mechanics and Engineering **193**, 4819–4836 (2004).

[48]M. A. Fernández, J.-F. Gerbeau, and V. Martin, "Numerical simulation of blood flows through a porous interface", ESAIM: Mathematical Modelling and Numerical Analysis **42**, 961–990 (2008).

[49]M. Astorino, J. Hamers, S. C. Shadden, and J.-F. Gerbeau, "A robust and efficient valve model based on resistive immersed surfaces", International Journal for Numerical Methods in Biomedical Engineering **28**, 937–959 (2012).

[50]A. This, L. Boilevin-Kayl, M. A. Fernández, and J.-F. Gerbeau, "Augmented resistive immersed surfaces valve model for the simulation of cardiac hemodynamics with isovolumetric phases", International Journal for Numerical Methods in Biomedical Engineering **36**, `10.1002/cnm.3223` (2019).

[51]Z. M. G. Inc., "Zygote solid 3d heart generation ii developement report. tech. rep.", (2014).

[52]A. Veneziani and C. Vergara, "Flow rate defective boundary conditions in haemodynamics simulations", International Journal for Numerical Methods in Fluids **47**, 803–816 (2005).

[53]E. Helps and D. McDonald, "Observations on laminar flow in veins", The Journal of physiology **124**, 631 (1954).

[54]K. E. Schober, V. L. Fuentes, J. D. Mcewan, and A. T. French, "Pulmonary venous flow characteristics as assessed by transthoracic pulsed doppler echocardiography in normal dogs", Veterinary Radiology & Ultrasound **39**, 33–41 (1998).

[55]P. C. Franzone, L. F. Pavarino, and S. Scacchi, *Mathematical cardiac electrophysiology*, Vol. 13 (Springer, 2014).

[56]K. H. Ten Tusscher and A. V. Panfilov, "Alternans and spiral breakup in a human ventricular tissue model", American Journal of Physiology-Heart and Circulatory Physiology **291**, H1088–H1100 (2006).

[57]F. Regazzoni, L. Dede', and A. Quarteroni, "Biophysically detailed mathematical models of multiscale cardiac active mechanics", PLoS computational biology **16**, e1008294 (2020).

[58]J. M. Guccione and A. D. McCulloch, "Finite element modeling of ventricular mechanics", in *Theory of heart* (Springer, 1991), pp. 121–144.

[59]F. Regazzoni, L. Dede', and A. Quarteroni, "Machine learning of multiscale active force generation models for the efficient simulation of cardiac electromechanics", Computer Methods in Applied Mechanics and Engineering **370**, 113268 (2020).

[60]J. D. Bayer, R. C. Blake, G. Plank, and N. A. Trayanova, "A novel rule-based algorithm for assigning myocardial fiber orientation to computational heart models", Annals of biomedical engineering **40**, 2243–2254 (2012).

[61]R. Piersanti, P. C. Africa, M. Fedele, C. Vergara, L. Dede', A. F. Corno, and A. Quarteroni, "Modeling cardiac muscle fibers in ventricular and atrial electrophysiology simulations", Computer Methods in Applied Mechanics and Engineering **373**, 113468 (2021).

[62]M. Salvador, L. Dede', and A. Quarteroni, "An intergrid transfer operator using radial basis functions with application to cardiac electromechanics", Computational Mechanics **66**, 491–511 (2020).

[63]A. Quarteroni, *Numerical models for differential problems*, Vol. 2 (Springer, 2009).

[64]P. K. Kundu, I. M. Cohen, and D. R. Dowling, *Fluid Mechanics*, 5th ed. (Academic Press, 2014).

[65]`https://www.paraview.org/Wiki/PvPython_and_PvBatch`.

[66]`https://lifex.gitlab.io/`.

[67]L. Antiga, M. Piccinelli, L. Botti, B. Ene-Iordache, A. Remuzzi, and D. A. Steinman, "An image-based modeling framework for patient-specific computational hemodynamics", Medical & Biological Engineering & Computing **46**, 1097–1112 (2008).

[68]`www.vmtk.org`.

[69]M. Fedele and A. Quarteroni, "Polygonal surface processing and mesh generation tools for the numerical simulation of the cardiac function", International Journal for Numerical Methods in Biomedical Engineering **37**, `10.1002/cnm.3435` (2021).

[70]A. Quarteroni, R. Sacco, and F. Saleri, *Numerical mathematics*, Vol. 37 (Springer Science & Business Media, 2010).

[71]`https://github.com/martemyev/tethex`.

[72]D. Arndt, W. Bangerth, B. Blais, M. Fehling, R. Gassmöller, T. Heister, L. Heltai, U. Köcher, M. Kronbichler, M. Maier, P. Munch, J.-P. Pelteret, S. Proell, K. Simon, B. Turcksin, D. Wells, and J. Zhang, "The `deal.II` library, version 9.3", Journal of Numerical Mathematics (2021, accepted for publication).

[73]S. Deparis, G. Grandperrin, and A. Quarteroni, "Parallel preconditioners for the unsteady Navier–Stokes equations and applications to hemodynamics simulations", Computers & Fluids **92**, 253–273 (2014).

[74]`https://trilinos.github.io`.

[75]G. S. Gulsin, A. Singh, and G. P. McCann, "Cardiovascular magnetic resonance in the evaluation of heart valve disease", BMC Medical Imaging **17**, `10.1186/s12880-017-0238-0` (2017).

[76]R. M. Carey and P. K. Whelton, "Prevention, detection, evaluation, and management of high blood pressure in adults: synopsis of the 2017 American College of Cardiology/American Heart Association Hypertension Guideline", Annals of internal medicine **168**, 351–358 (2018).

[77]T. Sugimoto, R. Dulgheru, A. Bernard, F. Ilardi, L. Contu, K. Addetia, L. Caballero, N. Akhaladze, G. Athanassopoulos, D. Barone, M. Baroni, N. Cardim, A. Hagendorff, K. Hristova, T. Lopez, G. de la Morena, B. Popescu, M. Moonen, M. Penicka, T. Ozyigit, J. Rodrigo Carbonero, N. van de Veire, R. von Bardeleben, D. Vinereanu, J. Zamorano, Y. Go, M. Rosca, A. Calin, J. Magne, B. Cosyns, S. Marchetta, E. Donal, G. Habib, M. Galderisi, L. Badano, R. Lang, and P. Lancellotti, "Echocardiographic reference ranges for normal left ventricular 2D strain: results from the EACVI NORRE study", European Heart Journal-Cardiovascular Imaging **18**, 833–840 (2017).

[78]A. Maceira, S. Prasad, M. Khan, and D. Pennell, "Normalized left ventricular systolic and diastolic function by steady state free precession cardiovascular magnetic resonance", Journal of Cardiovascular Magnetic Resonance **8**, 417–426 (2006).

[79]P. Tripathi, "Pathophysiological mechanism behind diabetic cardiovascular disorders", International Journal of Current Research **6**, 4426–4436 (2014).

[80]C. P. Appleton, "Evaluation of diastolic function by two-dimensional and doppler assessment of left ventricular filling including pulmonary venous flow", in *Diastology* (Elsevier, 2008), pp. 115–143.

[81]`https://criticalecho.com/tutorial-6-assessment-of-lv-diastolic-function-and-filling-pressures`.

[82]J. Hunt, A. Wray, and P. Moin, "Eddies, stream, and convergence zones in turbulent flows", Center for Turbulence Research Report **CTR-S88**, 193–208 (1988).

[83]P. Dyverfeldt, M. Bissell, A. J. Barker, A. F. Bolger, C.-J. Carlhäll, T. Ebbers, C. J. Francios, A. Frydrychowicz, J. Geiger, D. Giese, M. D. Hope, P. J. Kilner, S. Kozerke, S. Myerson, S. Neubauer, O. Wieben, and M. Markl, "4D flow cardiovascular magnetic resonance consensus statement", Journal of Cardiovascular Magnetic Resonance **17**, `10.1186/s12968-015-0174-5` (2015).

[84]R. J. van der Geest and P. Garg, "Advanced analysis techniques for intra-cardiac flow evaluation from 4D flow MRI", Current Radiology Reports **4**, `10.1007/s40134-016-0167-7` (2016).

[85]P. M. Arvidsson, S. J. Kovács, J. Töger, R. Borgquist, E. Heiberg, M. Carlsson, and H. Arheden, "Vortex ring behavior provides the epigenetic blueprint for the human heart", Scientific Reports **6**, `10.1038/srep22021` (2016).

[86]W. Y. Kim, P. G. Walker, E. M. Pedersen, J. K. Poulsen, S. Oyre, K. Houlind, and A. P. Yoganathan, "Left ventricular blood flow patterns in normal subjects: a quantitative analysis by three-dimensional magnetic resonance velocity mapping", Journal of the American College of Cardiology **26**, 224–238 (1995).

[87]R. Mittal, J. H. Seo, V. Vedula, Y. J. Choi, H. Liu, H. H. Huang, S. Jain, L. Younes, T. Abraham, and R. T. George, "Computational modeling of cardiac hemodynamics: current status and future outlook", Journal of Computational Physics **305**, 1065–1082 (2016).

[88]M. Enriquez-Sarano, K. S. Dujardin, C. M. Tribouilloy, J. B. Seward, A. P. Yoganathan, K. R. Bailey, and A. J. Tajik, "Determinants of pulmonary venous flow reversal in mitral regurgitation and its usefulness in determining the severity of regurgitation", The American journal of cardiology **83**, 535–541 (1999).

[89]R. Koizumi, K. Funamoto, T. Hayase, Y. Kanke, M. Shibata, Y. Shiraishi, and T. Yambe, "Numerical analysis of hemodynamic changes in the left atrium due to atrial fibrillation", Journal of biomechanics **48**, 472–478 (2015).

[90]A. This, "Image/model fusion for the quantification of mitral regurgitation severity", PhD thesis (Sorbonne université, 2019).

[91]G. W. Fischer and P. Trigo, "15 - Mitral Valvular Disease", in *Perioperative transesophageal echocardiography*, edited by D. L. Reich and G. W. Fischer (W.B. Saunders, Philadelphia, 2014), pp. 144–155.

MOX Technical Reports, last issues

Dipartimento di Matematica
Politecnico di Milano, Via Bonardi 9 - 20133 Milano (Italy)

50/2021 Ciaramella, G.; Vanzan, T.
On the asymptotic optimality of spectral coarse spaces

51/2021 Ciaramella, G.; Kwok, F.; Mueller, G.
Nonlinear optimized Schwarz preconditioner for elliptic optimal control problems

52/2021 Ciaramella, G.; Mechelli, L.
An overlapping waveform-relaxation preconditioner for economic optimal control problems with state constraints

53/2021 Ciaramella, G.; Mechelli, L.
On the effect of boundary conditions on the scalability of Schwarz methods

54/2021 Ciaramella, G.; Gander, M.J.; Mamooler, P.
HOW TO BEST CHOOSE THE OUTER COARSE MESH IN THE DOMAIN DECOMPOSITION METHOD OF BANK AND JIMACK

55/2021 Buchwald, S.; Ciaramella, G.; Salomon, J.
ANALYSIS OF A GREEDY RECONSTRUCTION ALGORITHM

50/2021 Rea, F.; Savaré, L; Franchi, M.; Corrao, G; Mancia, G
Adherence to Treatment by Initial Antihypertensive Mono and Combination Therapies

49/2021 Rea, F.; Savaré, L; Franchi, M.; Corrao, G; Mancia, G
Adherence to Treatment by Initial Antihypertensive Mono and Combination Therapies

47/2021 Orlando, G; Della Rocca, A; Barbante, P. F.; Bonaventura, L.; Parolini, N.
An efficient and accurate implicit DG solver for the incompressible Navier-Stokes equations

48/2021 Riccobelli, D.
Active elasticity drives the formation of periodic beading in damaged axons